PFC/RR-91-19

Studies of Runaway Electron Transport in TEXT

Wang, P.W.

December 1991

Plasma Fusion Center
Massachusetts Institute of Technology
Cambridge, Massachusetts 02139 USA

Studies of Runaway Electron Transport in TEXT

by

Pei-Wen Wang

S.M., Stevens Institute of Technology (1983)

Submitted to the Department of Nuclear Engineering
in partial fulfillment of the requirements for the degree of

Doctor of Philosophy

at the

MASSACHUSETTS INSTITUTE OF TECHNOLOGY

September 1991

Signature of Author .....
Department of Nuclear Engineering
August 1991

Certified by .....
Dieter J. Sigmar
Senior Research Scientist, Plasma Fusion Center
Prof. of Theoretical Physics, Technical University of Vienna
Thesis Supervisor

Certified by .....
Ted F. Yang
Research Scientist, Plasma Fusion Center
Thesis Reader

Certified by .....
Stanley Luckhardt
Principal Research Scientist, Plasma Fusion Center
Thesis Reader

Accepted by .....
Allan F. Henry
Chairman, Departmental Graduate Committee

Studies of Runaway Electron Transport in TEXT

by

Pei-Wen Wang

Submitted to the Department of Nuclear Engineering
on August 1991, in partial fulfillment of the
requirements for the degree of
Doctor of Philosophy

ABSTRACT

The transport of runaway electrons is studied by a plasma position shift experiment and by imposing an externally applied perturbing magnetic field on the edge. The perturbing magnetic field can produce either magnetic islands or, with overlapping islands, a stochastic field. Hard X-ray signals are then measured and compared with analytic and numerical model results. Diffusion coefficients in the edge, $\sim 10^4$ cm^2/sec, and inside the plasma, $\sim 10^2 - 10^3$ cm^2/sec, are estimated. The averaged drift effects are small and the intrinsic magnetic fluctuations are estimated to be $< (b_r/B_0)^2 > \sim 10^{-10}$ at the edge and decreasing inward. Runaway electrons are a good diagnostic of the magnetic fluctuations. It is concluded that the magnetic fluctuations have a negligible effect on electron thermal diffusion in the edge plasma.

Thesis Supervisor: Dieter J. Sigmar
Title: Senior Research Scientist, Plasma Fusion Center
Prof. of Theoretical Physics, Technical University of Vienna

Thesis Reader: Ted F. Yang
Title: Research Scientist, Plasma Fusion Center

Thesis Reader: Stanley Luckhardt
Title: Principal Research Scientist, Plasma Fusion Center

Contents

Acknowledgements

It has been a great privilege to work in the field of controlled thermonuclear fusion. I wish to take this opportunity to express my gratitude to a number of people who have provided guidance and assistance during the course of my graduate studies.

I would like to thank Professor Dieter Sigmar, my thesis advisor, for his patient support and the stimulating discussions. Next I wish to thank Dr. Ted Yang for the financial support without which I could never survive these years. I also appreciate the help of Dr. Stan Luckhardt for being my thesis reader and Professor Jeff Freidberg and Professor Ian Hutchinson for serving on my thesis committee.

Many people have assisted me during the time I stayed in Texas. They made the Texas experience so pleasant and memorable. Among all the people, I wish to thank Professor Roger Bengtson first. He guided me not only in how to do the research but also in the way of making things go smoothly. I hope I can still learn more from him. Dr. Alan Wootton was the person who initiated the idea of the runaway electron study. He gave me many new ideas and was always willing to discuss questions in spite of his busy schedule.

I would like to acknowledge the contributions of the TEXT group to this work. Of all those scientists, I would like to thank Dr. Steve McCool for the friendly support and Dr. David Sing, Dr. Burton Richards, Dr. Ron Bravenec, Dr. Gary Hallock, and Dr. Ken Gentle for running TEXT. I also wish to thank TEXT technical staffs, Tom Herman, Wayne Henry, and Daniel Mendoza. Without them, life would be much more difficult.

I also wish to thank Dr. Cris Barnes for sending me the code REDDOG and many helpful suggestions. At Lodestar, I wish to thank Dr. Peter Catto and Dr. Jim Myra for the very ingenious comments.

I would like to thank my fellow students, Alan Wan, Warren Krueger, Scott Peng at MIT and Mark Foster, Jose Boedo, John Heards at University of Texas for their academic and philosophical help.

Finally, I want to thank my parents, my brothers and sisters for their encouragements. Of course, special thanks to my wife Sunnie who has always supported me through all these years and to my son Raymond and my daughter May for growing stronger day by day. They are the best things that have happened to me during my graduate study.

Chapter 1

Introduction

In tokamaks, the goal is to confine dense, high temperature plasmas long enough so that a considerable amount of fusion reactions can occur. Good energy confinement of the plasma is needed to maintain the high temperature at which the fusion reaction cross section is maximized. Because the plasma is composed of ionized particles, toroidal, poloidal and vertical magnetic fields are used for the containment of the plasma. The toroidal and vertical fields are generated by the current flowing in the external magnetic coils and the poloidal field is generated by the induced plasma current. Nested flux surfaces are created in the plasma. The study of the transport processes in this system has always been a very important topic in the plasma physics. It has been found that the electron thermal diffusivity is much higher than that predicted by neoclassical theory and the transport is therefore described as anomalous[1, 2, 3]. The anomalous transport has been attributed to electrostatic[4, 5, 6] or electromagnetic[7, 8, 9, 10, 11, 12] microscopic turbulence. Magnetic perturbations can destroy the magnetic flux surfaces[13] and generate magnetic islands. When two neighboring magnetic islands overlap, magnetic field lines wander stochastically, and allow the electrons to move along the perturbed field lines and transport energy due to random-walk processes. It is important to know the magnetic microturbulence and the effects of its interaction with electrons in the plasma.

Runaway electrons are electrons with high enough energy that the acceleration force by the induced electric field is greater than the frictional drag on them due to collisions. As they continue to accelerate, the collisions, which decrease as the velocity increases, become less and less, and the runaway electrons decouple from collisional interaction with the plasma. They are natural test particles for studying the collisionless transport due to magnetic turbulence in the plasma. One hopes to elucidate the intrinsic magnetic turbulence inside the plasma and the thermal electron transport by understanding the runaway electron diffusion processes.

Runaway electrons will become more important in larger, reactor-grade tokamaks which have higher temperatures and current, longer discharge lengths and better confinement of high energy particles. These runaway electrons can cause a considerable amount of damage to the vacuum vessel. In this thesis the transport of runaway electrons is studied in the Texas EXperimental Tokamak (TEXT). The TEXT machine and basic diagnostics are introducd.

The basic properties, production rate, acceleration and drift motion of the runaway electrons are discussed and previous work on runaway electron transport are briefly reviewed in Chapter 2. The critical velocity at which the electric force is equal to the drag force caused by collisions is defined. The history of developing the kinetic theory of runaway electron production rate is reviewed and the formula is presented. Because of the collisionless characteristics of runaway electrons, the drift orbit theory is important in understanding the basic confinement of the runaway electron in tokamaks. The displacement of runaway electron drift orbit from the flux surface is derived. A numerical code calculating the increase in drift orbit due to the energy increase in the dc electric field has been written and the results show that the drift orbit transport cannot be responsible for the runaway electron transport. Therefore, an anomalous diffusion coefficient is needed for the runaway electrons.

Chapter 3 shows the diagnostic techniques used for this study of runaway

electron transport. The thick-target bremsstrahlung radiation, generated when runaway electrons hit the limiter, is detected by a sodium iodide scintillator (NaI(Tl)). The NaI(Tl) detector with a photomultiplier tube (PMT), its interactions with X-ray photons, and the counting system are described. A numerical code DOG (Determination Of Gamma emission)[14] which calculates the thick-target bremsstrahlung intensity, the transmission of the photons through different materials, and the detector response, is used for the data analysis.

Chapter 4 describes the two experiments performed to study the runaway electron transport : (i) displacing the plasma column inward by increasing the vertical magnetic field, and (ii) applying an externally generated magnetic field perturbation. The responses of the runaway electrons to the perturbations are used to deduce the diffusion coefficient D. In the first experiment, an extra distance is created by suddenly shifting the plasma column inward for the runaway electrons to diffuse out to the limiter. Because it takes them longer time to reach the limiter due to the shift, an initial dip in the hard X-ray signal is expected and observed experimentally.

The second experiment uses a set of magnetic coils, Ergodic Magnetic Limiter (EML), to generate magnetic fields to perturb the plasma edge. The magnetic field is resonant with the equilibrium magnetic surfaces in the edge layer. Magnetic islands or, with overlapped islands, a layer of ergodic surfaces in the edge are produced. The field lines are traced by using a numerical mapping code. The structure of the magnetic configurations with different levels of perturbations is investigated extensively. The responses of the runaway electrons associated with the magnetic perturbations are observed.

In another experiment EML and position shift perturbations are both applied to the plasma at the same time. The responses of the hard X-ray signal show interesting implications and help to better understand the runaway electron transport.

Chapter 5 shows the analytic and numerical models for the experiments. The

diffusion equation with an anomalous diffusion coefficient, which is assumed to be a constant, is solved analytically by using a moving boundary condition to simulate the experiments. The analytic solutions with some approximations can be obtained. Also, more exact numerical solutions are obtained. The solutions are compared to the experimental results to get the diffusion coefficient from the best fit of the two. The diffusion coefficient deduced from the position shift experiment can be interpreted as the edge value and the one from the magnetic field perturbation experiment as the value further in. It is then found that the runaway electron diffusion coefficient is $\sim 10^2$–10^3 cm^2/sec in the core of the plasma and about 10^4 cm^2/sec at the edge. The results are then discussed. A radially varying profile can also be determined.

The drift surfaces of the high energy electrons with EML are plotted using a numerical code. The averaging drift effects on the runaway electron drift surfaces are found to be small. The intrinsic magnetic fluctuations can be estimated to be $< (b_r/B_0)^2 > \geq 3 \times 10^{-10}$ at the edge and decreasing inward if they are the responsible mechanism for the runaway electron anomalous transport. These magnetic fluctuation level may be too small to be responsible for the thermal diffusivity of the background electrons in the edge.

The last chapter, Chapter 6, summarizes the results of this thesis. Runaway electrons are a good diagnostic of measuring the magnetic fluctuations. By understanding their diffusion in the plasma, runaway electrons can offer information more deeply into the plasma core than that of the external B-dot probes.

Chapter 2

Runaway electron theories, experiments and the TEXT tokamak

This chapter reviews the basic properties of the runaway electrons. The reason why the electrons can run away is discussed and the critical velocity is defined. The development of the kinetic theory of runaway electron production rate and the drift orbit theory are presented. Also the TEXT tokamak is briefly described.

2.1 Review of the runaway electron theories

The existence of the induced electric field E would accelerate electrons in the plasma due to the electric force $F_E = eE$. The friction force on an electron moving in a Maxwellian distribution of field particles can be written in the simple form

$$F_f(v) = m_e v \nu_e \tag{2.1}$$

where

$$\nu_e = \frac{4\pi e^4 n_e \ln \Lambda}{m_e^2 v^3} \tag{2.2}$$

is the collision frequency, n_e is the electron density, m_e is the electron mass, v is the electron velocity, and $\ln\Lambda$ is the Coulomb logarithm. This friction force decreases as the electron velocity increases. The critical velocity can be defined by balancing the electric force against the frictional drag of the Coulomb collisions

$$F_E = F_f(v = v_c) \tag{2.3}$$

and the critical velocity is

$$v_c = \left(\frac{4\pi e^3 n_e \ln\Lambda_c}{m_e E}\right)^{1/2} \tag{2.4}$$

where $\Lambda_c \equiv \Lambda(v = v_c)$. Electrons with velocities $v < v_c$ will remain in the thermal distribution. However, electrons with velocities higher than v_c will be gradually accelerated by the electric field to higher energies. The critical electric field[15] can also be defined to be the one that would accelerate the thermal electrons as

$$F_E(E = E_c) = F_f(v = v_{th}) \tag{2.5}$$

and

$$E_c = \frac{4\pi e^3 n_e \ln\Lambda}{m_e v_{th}^2} \tag{2.6}$$

Thus, for electric fields $E \gtrsim E_c$, the bulk of the electrons will run away, while for electric fields $E \ll E_c$, only a small fraction will run away.

2.1.1 Kinetic theory of runaway electron production

The kinetic theory of runaway production in a plasma has been studied extensively by numerous authors. For the most part, the assumptions of weak electric field $E \ll E_c$ in an infinite, homogeneous, fully ionized, quasi-steady-state, and near Maxwellian plasma have been used. The theory of runaway production will be reviewed briefly in this section. More detailed review can be found in a review article by Knoepfel and Spong[16] and a lecture by Sesnic[17].

The earliest work was done by Dreicer[15]. He divided velocity space into collisional and runaway regions by the velocity below or above the critical velocity.

The runaway production rate was the diffusion rate across the $v = v_c$ surface. The electron distribution function was expanded as $f = f_0(\vec{v},t) + \mu f_1(\vec{v},t)$, where μ is the cosine of the angle between the velocity $\vec{v}$ and the electric field $\vec{E}$; f_0 was assumed to vanish for velocities greater than the critical velocity and to vary with time as exp(-λt). The initial-value problem was then solved for the eigenvalue λ which represented the rate of diffusion of electrons into the runaway region.

Gurevich[18] realized that the distribution function is expected to be peaked about $\mu = 1$ near the runaway critical velocity. He expanded $\ln(f)$ in powers of $1 - \mu$ and the solution was valid for velocities $v_{th} \ll v < v_c$ and had a singularity at v_c. Lebedev[19] improved the technique by using two different expansions for $\ln(f)$ in powers of $1 - \mu$ for the range $v \leq v_c$ and for $v \ll v_c$.

Kruskal and Bernstein[20] and Gurevich and Zhivlyuk[21] presented the most consistent and mathematically rigorous analysis of the problem. They divided velocity space into five separate regions and expanded f in powers of the electric field strength. In each region the solution was solved and matched at the adjacent boundaries.

Kulsrud, et al.[22] solved the Fokker-Planck equation numerically to determine the electron runaway rates for a range of electric field values and effective ionic charges Z_{eff}. The comparisons with their result showed close agreement of the Kruskal-Bernstein's and Lebedev's analytical results. However, Gurevich's expression agrees less well and Dreicer's result is larger by over an order of magnitude, as shown in Fig 2-1.

Connor and Hastie[23] used an approach similar to that of Kruskal and Bernstein and included the relativistic and impurity effects. They found that no runaway electrons are produced for the electric fields $E < E_c \times kT_e/m_ec^2$ and determined the runaway production rate, λ, as

$$\lambda = 0.35 n_e \nu_e \left(\frac{E_c}{E}\right)^{h(\alpha,Z)} \exp\{-[\frac{s(\alpha)}{4}\frac{E_c}{E} + \left(\frac{2E_c}{E}\right)^{1/2}\gamma(\alpha,Z)]\} \qquad (2.7)$$

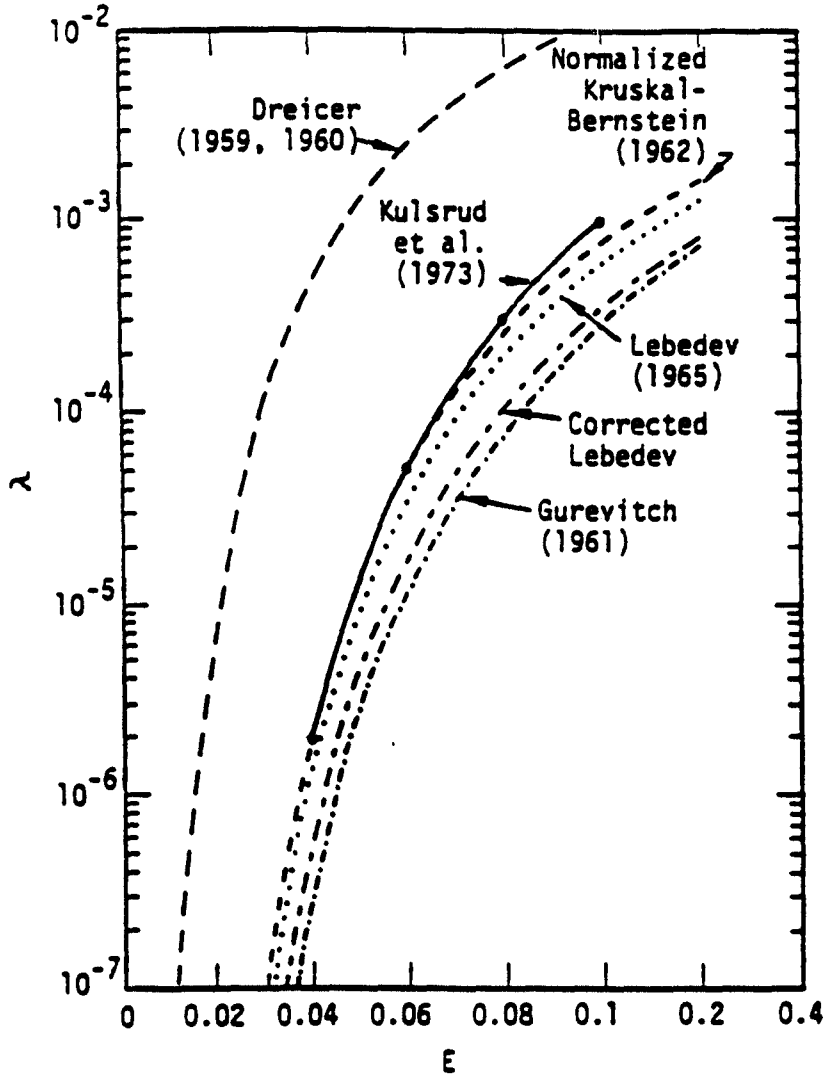

Figure 2-1: Comparison of analytically and numerically determined runaway production rates(λ) for Z = 1. The Kruskal-Bernstein expression is normalized to the numerical value of Kulsrud et al., the solid curve, at E = 0.04[16,22].

where

$$s(\alpha) = 8\alpha[\alpha - \frac{1}{2} - \sqrt{\alpha(\alpha-1)}] \quad (2.8)$$

$$\gamma(\alpha, Z) = \sqrt{\frac{(1+Z)\alpha^2}{8(\alpha-1)}}\cos^{-1}(1-\frac{2}{\alpha}) \quad (2.9)$$

$$h(\alpha, Z) = \frac{1}{16(\alpha-1)}[\alpha(Z+1) - Z + 7 + 2\sqrt{\frac{\alpha}{\alpha-1}}(1+Z)(\alpha-2)] \quad (2.10)$$

and

$$\alpha = \frac{E}{E_c}\frac{m_e c^2}{T_e}$$

as $\alpha \rightarrow \infty$.

Cohen[24] considered the effect of impurities and found that the presence of impurity ions reduces the runaway electron production rate. Gurevich and Dimant[25] included the toroidal geometry effect and the result differs little from the previous ones.

2.1.2 Runaway electron drift orbit theory

Once a runaway electron is created, it will continue to accelerate in the electric field and gain energy. As its energy becomes higher, the runaway electron can be considered collisionless with respect to other particles. Ignoring the perpendicular velocity component which does not increase and thus remains relatively small, the energy gained by the electron in an electric field is

$$\frac{d(\gamma m_e v)}{dt} = eE \quad (2.11)$$

or

$$\frac{d(\gamma\beta)}{dt} = \frac{d(\gamma^2-1)^{1/2}}{dt} = \frac{eE}{m_e c} \quad (2.12)$$

where $\gamma \equiv 1/\sqrt{1-\frac{v^2}{c^2}}$ and $\beta \equiv v/c$ and the solution is

$$(\gamma^2-1)^{1/2} = (\frac{eE}{m_e c})t + (\gamma_0^2-1)^{1/2} \quad (2.13)$$

where $\gamma = \gamma_0$ at $t = t_0$.

Thus in the absence of collisions and other energy loss mechanisms the electron experiences the free-fall acceleration and gains momentum linearly in time. In TEXT the electron can gain 70 MeV of energy in one second for a typical discharge.

Since these electrons are considered collisionless because of their high energies, the single particle trajectories become useful in understanding their confinement in tokamaks. The trajectories of runaway electrons in the magnetic fields consist of a fast Larmor gyration around a guiding center. The length and time scales of the gyromotion are small compared to those of variations in the field itself. The guiding center motion is appropriate and sufficient to describe the electron motion. The components of the guiding center velocity[16], neglecting the $\vec{E} \times \vec{B}$ drift term for high energy electrons, are

$$\vec{v_g} \cong v_\theta \hat{e}_\theta + v_\parallel \hat{e}_\phi + (v_d + v_v)\hat{e}_z \tag{2.14}$$

where

$$v_\theta = \frac{r v_\parallel}{qR} = v_\parallel \frac{B_p}{B_T} \tag{2.15}$$

$$v_v = -v_\parallel \frac{B_v}{B_T} \tag{2.16}$$

$$v_d = \frac{1}{R\Omega_T}(v_\parallel^2 + \frac{1}{2}v_\perp^2) \tag{2.17}$$

B_θ, B_ϕ, B_v are the poloidal, toroidal, and vertical magnetic fields. The directions of velocities and magnetic fields are shown schematically in Fig. 2-2.

The conservation of canonical angular moment P_ϕ allows the formulation of the drift orbit displacement as a function of the poloidal flux ψ(r)

$$P_\phi = \gamma m_e R v_\phi - \frac{e}{c}\psi(r) \tag{2.18}$$

$$\psi(r) = \frac{2IR}{c}\int_0^r \frac{dr''}{r''}\int_0^{r''} r' j(r') dr' \tag{2.19}$$

For a flat current profile this function becomes

$$\psi(r) = \int_0^r B_p R dr' = \frac{R_0 I r^2}{c r_L^2}$$

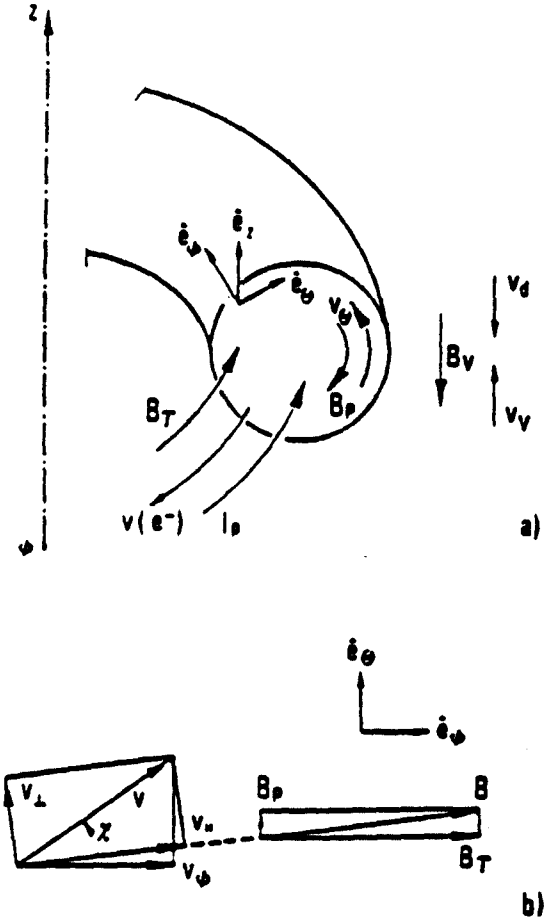

Figure 2-2: (a) Drift velocities for electrons and magnetic fields in a tokamak configuration. (b) Definition of velocity and magnetic field components.

for $r \leq r_L$, where r_L is the radius of the flat current profile, R_0 is the major radius, I is the total current, and $B_p = 2IrR_0/cr_L^2R$ is the poloidal magnetic field.

The radial outward shift d_γ of the runaway orbit is

$$d_\gamma = \rho_p \frac{r_L}{R_0} = \frac{r_L^2}{2R_0}\frac{I_A}{I} \tag{2.20}$$

where ρ_p is the poloidal Larmor radius and

$$I_A = \frac{\beta\gamma m_e c^3}{e}$$

is the Alfvén current.

The geometrical condition for confining the orbit can be written as

$$r_0 + d_\gamma + d_p \leq r_L$$

where r_0 is the radius of the runaway drift orbit and d_p is the shift of the center of the current distribution with respect to the geometrical center. This sets a limit on the runaway electron energy which is[16]

$$\gamma^2 - 1 < \left[2R(1 - \frac{r_c}{r_L})\frac{I}{17000 r_L}\right]^2 \tag{2.21}$$

where r_c is the initial drift radius. For $r_c \ll r_L$, this gives

$$\gamma < 91 \tag{2.22}$$

for the TEXT parameters, $I = 200$ kA, $r_L = 26$ cm, and $R = 100$ cm. This energy limit is much larger than the runaway electron energy in TEXT.

For a more realistic current profile, the shift orbit is no longer circular and the shift distance is reduced because more flux is enclosed in the orbit with a peaked profile.

2.1.3 Drift orbit transport

Knowing the runaway electron drift motion in a tokamak, the question is "Can the runaway electron transport be explained simply by the single particle drift

orbit ?". That is, can the increase in major radius of the runaway electron orbit due to the energy increase in an axisymmetric magnetic field be responsible for its transport ?

The following simplified set of guiding-center equations is used to calculate orbits in a standard cylindrical geometry (r, θ, z), with $x = r\cos\theta$, $y = r\sin\theta$.

$$\begin{aligned} \frac{dx}{dt} &= v(\frac{B_x}{B_z}) \\ \frac{dy}{dt} &= v(\frac{B_y}{B_z}) \\ \frac{d(\gamma^2-1)^{1/2}}{dt} &= \frac{eE}{m_e c} \end{aligned} \tag{2.23}$$

where

$$\begin{aligned} v_d &= -\frac{\gamma}{\Omega_0 R_0} v^2 \\ B_z &= \frac{B_0 R_0}{R} \\ R &= R_0 + r\cos\theta \\ v &\approx v_z \\ \Omega_0 &= \frac{eB_0}{m_e c} \\ E &= \frac{V_l}{2\pi R_0}, \text{ where } V_l \text{ is the loop voltage} \end{aligned}$$

The perpendicular velocity is negligibly small compared with the parallel velocity and is neglected, $v \approx v_z$, so is the cross-field ∇B drift velocity term in v_d. The z coordinate is irrelevant here.

The poloidal field $B_p = (B_x^2 + B_y^2)^{1/2}$ is calculated from the current density profile, which is assumed to have the form $\propto [1-(r/a)^2]$, and can be written as

$$B_p = \frac{\mu_0 I}{\pi a^2} r(1 - \frac{r^2}{2a^2}) \tag{2.24}$$

The assumed current profile is sufficient to estimate the distance of the drift displacement from the flux surface on TEXT.

To make it easier for numerical calculations, Eq. 2.23 can be written as

$$\frac{dx}{d(\gamma^2-1)^{1/2}} = v(\frac{B_x}{B_z})(\frac{m_e c}{eE}) \quad (2.25)$$

$$\frac{dy}{d(\gamma^2-1)^{1/2}} = [v(\frac{B_y}{B_z})+v_d](\frac{m_e c}{eE}) \quad (2.26)$$

A standard simultaneous ordinary differential equations solver[26] is used to solve the equations. It integrates a system of first-order differential equations over a range with initial conditions given below, using a Runge-Kutta-Merson method, and returns the solution at points specified. The accuracy of the integration is controlled by input parameters. The values of $V_l = 1.5$ V, $I = 200$ kA, and $B_0 = 2$ T are used and three initial electron positions, $x = 0$ cm, $y = 5, 10, 20$ cm, are followed from $\gamma = 1$ to $\gamma = 20$ which is chosen because the runaway electron maximum energy is below this value as observed experimentally on TEXT and will be discussed in Chapter 4. Fig. 2-3 shows the orbits on x-y plane and the increase in d_γ as a function of γ.

The runaway electrons are expected to be created mostly in the center of the plasma as they follow the field lines of small minor radius orbits with drift orbit displacements d_γ. The accelerating runaway electron orbits are closely related to the time-independent orbits. This is likely to be explained by the statement that the cross-sectional area of a closed runaway orbit is an adiabatic invariant with respect to particle energy variations[27]. The orbit radius will increase only very little as the electron gains energy and the orbit shifts outward[28], as can be seen in Fig. 2-3. Only when the electron has accelerated to extremely high energies, about 50 MeV for TEXT, can it reach the outside of the limiter.

The energies of the runaway electrons observed experimentally are much lower than could be accounted for from the drift orbit displacement transport. Some other mechanisms must be acting upon the runaway electrons to drive them out. This anomalous transport is studied in this thesis.

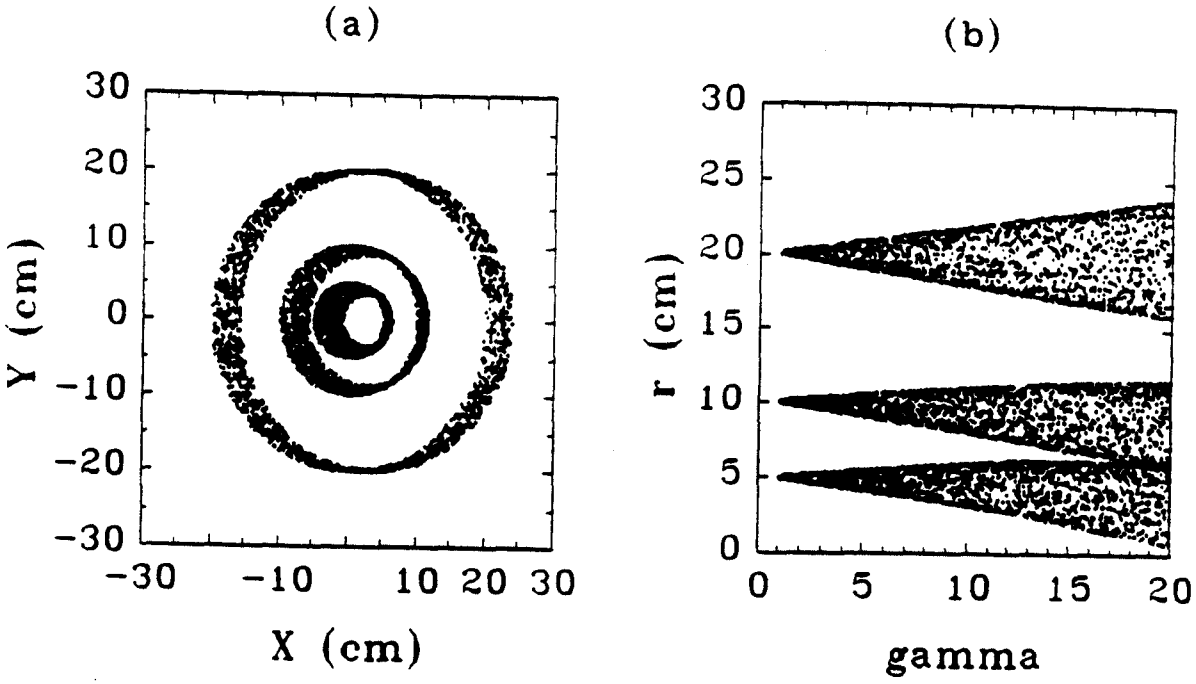

Figure 2-3: Three electrons at the initial positions $x = 0$ cm, $y = 5, 10, 20$ cm with $V_l = 1.5$ V, $I = 200$ kA, and $B_0 = 2$ T are followed from $\gamma = 1$ to $\gamma = 20$. (a) The drift orbits on x-y plane. (b) The increase in d_γ, radial outward shift of the runaway drift orbit, as a function of γ

2.2 Review of previous works on runaway electron transport

This section reviews the previous studies of the runaway electron transport briefly. More detailed reviews have been done by Knoepfel and Spong[16] and Barnes[14]. The measurement of bremsstrahlung photon spectra, which can be characterized by a spectral energy E_{s0} with the exponential distribution $N(E) \propto e^{-(E/E_{s0})}$, is crucial for the runaway electron confinement.

Some of the earliest experiments on runaway electrons were done on tokamak LT-1 and LT-3. By observing the thick-target bremsstrahlung X-rays from a movable Molybdenum wire probe using a NaI scintillator in the photon energy range up to 100 keV, they measured a decreasing electron energy spectrum during MHD instability cycles[29]. Using a fixed probe and a movable quencher probe inserted into the plasma to obtain radial information from the thick-target bremsstrahlung emitted in LT-3, they determined that runaway electrons (< 100 keV) drift surfaces lie close to the magnetic surfaces. They found that runaway electrons were created on magnetic surfaces inside the radius of the probe and diffuse outward, possibly because of stochastic wandering of magnetic field lines[30]. The large diffusion coefficient for runaway electrons could be due to a parallel velocity dependence of the transport. Runaway electrons with energies < 600 keV were formed within the central 4 cm of the plasma and diffused outward with rms step sizes of approximately 1 mm near the center and 1 cm at the edge of the plasma[31]. With a thin tungsten wire inserted into the plasma, the rms step length of 0.3 to 1.0 mm, with the step size increasing with increasing energy of X-rays in the range > 10 to > 100 keV, was obtained[32]. Other early experiments included the runaway dominated discharges in the T-6 tokamak[33], low density, high q plasmas in TM-3 [34, 35], the low density discharges in Alcator[36], and the normal discharges in ST[37, 38].

The studies of runaway dominated discharges in tokamaks were carried out

on the ORMAK tokamak[39]. Two types of discharges were classified by the observations of limiter hard X-ray emission. In type A discharges, the runaway electrons were generated in the outer plasma layers (19 – 20 cm) and lost to the wall or limiter in the first 10 msec. In type B discharges, no X-rays were observed until about 40 msec and the X-ray intensity increased as the current began to drop. In both cases, it was concluded that the multi-MeV electrons were generated in layers by the skin effect at the beginning of the discharge and the drift orbit model was used to explain the loss of the runaway electrons. This is contrary to the measurements that the runaway electrons are created in the central region and that the loss mechanism is caused by the anomalous transport.

The radial transport of the runaway electrons was investigated by shifting the plasma column inward[40]. The experimental results showed that the drift orbit theory could not explain the drop in the hard X-ray intensity. An anomalous diffusion coefficient near the edge was needed to account for the lack of a well defined gap.

By changing the vertical magnetic field the plasma was moved rapidly outward in Tuman-2[41]. The limiter X-ray signal was observed to first increase rapidly then reach a peak and then decrease to zero. This behavior was found for sufficiently large velocity, $v > 4 \times 10^4$ cm/sec. They concluded from this observation that most of the runaway electrons were in a layer about 1 cm thick near the limiter. The correlation of the X-ray and magnetic fluctuations was also observed. Also by rapidly increasing the toroidal field a compression of the plasma was induced. That the X-ray signal did not vanish completely during the compression implied a runaway electron transport process.

An X-ray peak at about 3 msec into the current build up phase and the termination of the plasma current were observed in Pulsator[42]. They estimated an overall confinement time of about 10 msec. They also confirmed that the orbit shift model can explain the preference of the limiter outside with respect to runaway bombardment, but fails to explain how to get from the center to

the outer region. An anomalous transport seemed to be needed. A strong m = 2 magnetic island located in the outer region of the plasma could produce the hard X-ray oscillation at the same frequency and phase[43]. A three-dimensional, time-independent code was used to calculate high energy runaway electron orbits in the presence of ergodic magnetic fields and it was found that for high energies E = 5 MeV and large gyroradii $v_\perp/v_\parallel = 0.1$ the runaway electron orbits are better confined than the radial magnetic diffusion might suggest. The correlation between fluctuations in the microwave radiation at the plasma frequency and fluctuations in the hard X-ray flux from the limiter was reported in PRETEXT[44].

The instabilities driven by the runaway electron tail[45, 46, 47] formed by a dc electric field have been studied by many theoreticians [48, 49, 50, 51, 52, 53]. The instability is triggered by the anomalous Doppler resonance or Čerenkov resonance instability, depending on the values of the dc electric field and the ratio of the electron gyrofrequency to plasma frequency. Once the instability is triggered, the runaway tail relaxes into an isotropic distribution.

Runaway electron transport deduced from photonuclear activation was performed on the PLT limiter. The inferred runaway electron population was found to decrease exponentially with energy as $e^{-E/3.2MeV}$[54]. The oscillating steady state displacement of the plasma column driven by harmonics of a 60 Hz ripple in the PLT power supplies and feedback system for the vertical magnetic field was used to estimate the diffusion coefficient[55]. The time of increased hard X-rays following internal disruptions was interpreted to be the time for a perturbation to the runaway electron population to travel from the q = 1 region to the plasma boundary[56]. From all these results it was concluded that the runaway electrons anomalously diffuse out of the plasma due to electromagnetic turbulence. Their confinement increased with density and toroidal magnetic field, and increased at higher energy presumably due to drift orbit averaging of the turbulence[57, 58, 59, 55].

2.3 TEXT machine

The Texas EXperimental Tokamak is a medium-size tokamak of major radius R = 100 cm and minor radius a = 26 cm, defined by a TiC coated graphite poloidal limiter, with nominal magnetic field of 2.8 Tesla, nominal plasma current of 400 kA. The tokamak is a pulsed device with typical pulse duration of 0.5 seconds and 2-3 minutes between each discharge[60]. There are 16 toroidal magnetic coils. The toroidal field is driven by a motor-generator capable of sustaining a 0.5 sec flat-top with rise and fall of 1 sec. The toroidal current is induced in the working gas to form a plasma which has a density on the order of 3×10^{13} cm^{-3}. The average ripple produced by the 16 coils is less than 1% and a maximum of 3% at the outer edge.

The ohmic heating system has an iron-core transformer with two return legs and 1.6 V-sec without saturation. The typical temperature is 1 keV for electrons and 650 eV for ions. The plasma has circular cross section. Hydrogen, deuterium and helium plasma discharges with line averaged electron densities ranging from 1.0×10^{13} cm^{-3} to 7.0×10^{13} cm^{-3} are obtained routinely.

A discharge typically has three phases—a start-up phase in which the plasma current is ramped up to an operational value, a flat-top phase in which the current is held constant, and a final phase in which the plasma is lost due to disruption or ramping down of the current. Most experiments are performed in the flat-top phase in which the plasma reaches near steady-state conditions.

The basic TEXT diagnostics are the simplest and most fundamental machine diagnostics. Plasma current, $I_p(t)$, is measured by Rogowski coils around the vacuum vessel. Loop voltage is measured at a loop outside the vacuum vessel. The vertical and horizontal position of the plasma is calculated from sine and cosine loops, using simple equilibrium theory. The coordinates of the center of the outermost complete (presumed circular) flux surface are available from the calculations. The line integral of plasma density on a vertical chord through the geometric axis

is measured by 2 mm microwave interferometry. Other basic diagnostics includes ionization monitor, impurity monitor and residual gas analyzer. In addition to the basic diagnostics, a number of other more complex diagnostics are operating. Fig 2-4 shows the TEXT tokamak and the positions of the diagnostics on TEXT.

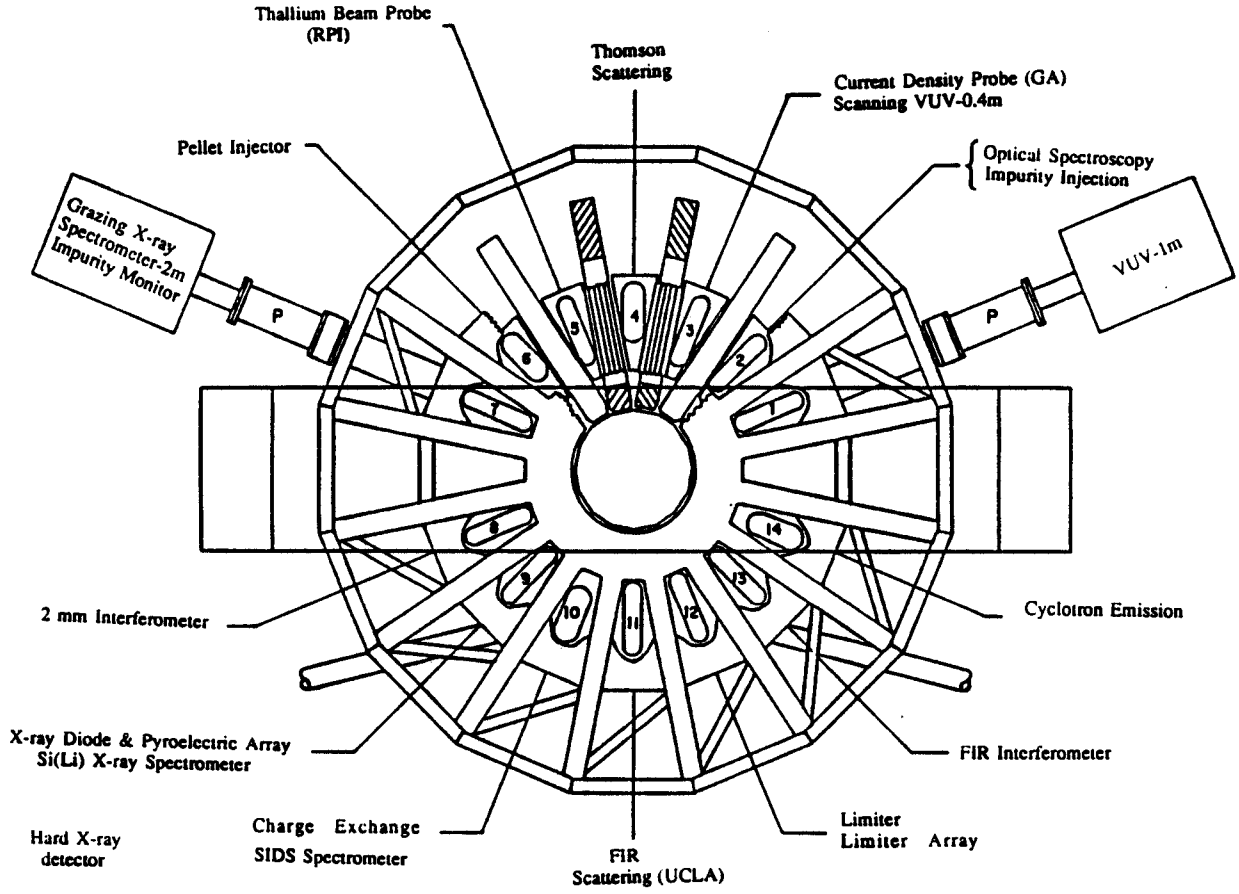

Figure 2-4: Plan view of the TEXT machine with 16 toroidal magnetic coils and the positions of the diagnostics and hard X-ray detector.

Chapter 3

Detection of runaway electrons and data analysis

To study the runaway electron transport we need the diagnostics to detect them in the plasma. Ideally one would like to measure the runaway electron distribution at all times. Practically there are several ways of detecting the runaway electrons. Each has its advantages and disadvantages.

The plasma bremsstrahlung caused by the collisions of the runaway electrons with the plasma particles could be measured and the runaway electron energy inferred[61, 62]. Because the plasma is optically thin to these bremsstrahlung X-rays, this radiation is known as thin-target bremsstrahlung. The radiation emitted from thermal electrons is useful as an electron temperature diagnostic. For high energy runaway electrons, the problem with this technique is the low count rate due to the small bremsstrahlung cross section. Many shots may be required to accumulate useful data and great care must be exercised to isolate the signal from noises coming from the wall and limiter.

The most common diagnostic technique is to measure the thick-target bremsstrahlung at the limiter when runaway electrons leave the plasma and hit the limiter. This technique is relatively simple to implement and the radiation is much more intense than that from other sources. However, this technique can not measure the

runaway electron distribution directly. It only measures those runaway electrons that are no longer confined. Also it is difficult to relate the measured signal to the runaway electrons themselves.

In this chapter the detection technique, which measures the limiter bremsstrahlung radiation, is described in the first section. The sodium iodide scintillator is used to detect the X-rays and is described in some detail. A numerical code DOG (Determination Of Gamma emission)[14], which simulates the steps from the creation of the X-rays to the detector response, is used to relate the measured X-ray signal to the runaway electron flux to the limiter.

3.1 The detection of runaway electrons

The runaway electrons confined inside the plasma have drift surfaces shifted a few centimeters from the magnetic axis toward the major radius direction as shown in Fig. 2-3. When a runaway electron leaves the plasma, it intersects the material limiter at the outer side on the equatorial plane of the torus. The slowing down of the electron inside the limiter, as it loses its energy because of the high density of the limiter material, causes a considerable amount of bremsstrahlung. The thick-target bremsstrahlung emission intensity increases with incident electron energy and the bremsstrahlung cross section is dependent on the limiter material. Different limiter material has different thick-target bremsstrahlung cross section. On TEXT only carbon limiter material is used.

The bremsstrahlung photons may interact with the material nuclei and cause photo-nuclear processes to occur. The photon must have enough energy to overcome the binding energy of the emitted particles, so there is a threshold energy for such reactions. The threshold energy for the incident electron is about 21 MeV[63] for the photoneutron reaction to happen with the carbon limiter. This photoneutron reaction is not important on TEXT because the detected maximum X-ray energy($\sim$ 10 MeV) is far below the threshold energy.

After the emitted photons leave the limiter, they can pass through the vacuum vessel and other machine components in the path to the detector. Photons with lower energy are absorbed by these materials and those with higher energy can travel through considerable amount of material. A large amount of lead is used for the detector to collimate the X-ray emission generated at the limiter. The X-ray detector used in these experiments consists of a sodium iodide scintillator (NaI(Tl)) and a photomultiplier tube (PMT) housed in a lead cylinder. The lead shield cylinder has 2" thickness on side and 9" on the end facing the limiter. The detector is placed about 6 meters from the limiter and collimated to aim at the outside of the limiter. The sodium-iodide crystal is efficient at stopping the energetic photons and has been widely used for gamma ray spectroscopy in nuclear physics. The scintillator converts all or part of the X-ray photon energy into the kinetic energy of one or more electrons, and then converts the electron kinetic energy into light energy radiated from the scintillator. The PMT turns the light into an output pulse of current.

3.1.1 Sodium Iodide scintillation detector

A 3 inch diameter by 3 inch long sodium iodide crystal with a small amount of Tl added in order to activate the crystal, NaI(Tl), has good efficiency for gamma ray detection[64]. In the crystal a forbidden band in which no electrons are found separates the valence and conduction bands. The addition of activator fills in the forbidden band with the single atom energy levels of the activator. When an incident high energy photon enters, the electrons which gain energy from the interactions with the photon are boosted from the valence band into the conduction band leaving behind an equal number of holes. The positive holes will quickly drift to the activator sites and ionize them. The electrons in the conduction band are free to migrate through the crystal until they recombine with the ionized activators. The resulting neutral impurity atoms are in excited state. Deexcitation will occur very rapidly and emit visible photons. Typical half

lives for these excited states are on the order of 10^{-7} sec with the migration times being much shorter[65].

A PMT consists of a photocathode, a string of dynodes held at increasingly higher voltage by a voltage divider circuit, and an anode. Fig. 3-1 shows the structure and the circuit of the PMT. The photocathode is a photoelectric material that when struck by a photon with energy greater than the work function has a probability for the emission of a single photoelectron. This probability limits the resolution of NaI(Tl) X-ray spectrometer. A dynode is a material that emits a few eV electrons when struck by an energetic electron. The number of emitted electrons is proportional to the energy of the original electron. The potential difference between each anode will accelerate the emitted electrons and a larger number of electrons will be emitted on the next anode. The total electron charge is then converted into a voltage output pulse by integration over an RC circuit which is made up of the load resistor and coupling capacitor. The output pulse is then received by a preamplifier.

In order to understand the detector for X-ray detection, it is necessary to know the ways in which X-rays can interact with the detector material. The next subsection reviews such interactions.

3.1.2 Interactions of X-rays with NaI

To detect the X-rays the detector must be able to absorb most of the incident energetic photons. It is necessary to understand the interactions of X-rays with the detector. There are three processes by which the incident photon can interact with the scintillator, photoelectric absorption, Compton scattering and pair production. These processes are strongly dependent upon the energy of the photon and the atomic number Z of the material.

The photoelectric absorption happens at low photon energies, less than about 300 keV, and the photon is likely to be absorbed, depositing all its energy. The incident photon is absorbed and a photoelectron is emitted from one of the atomic

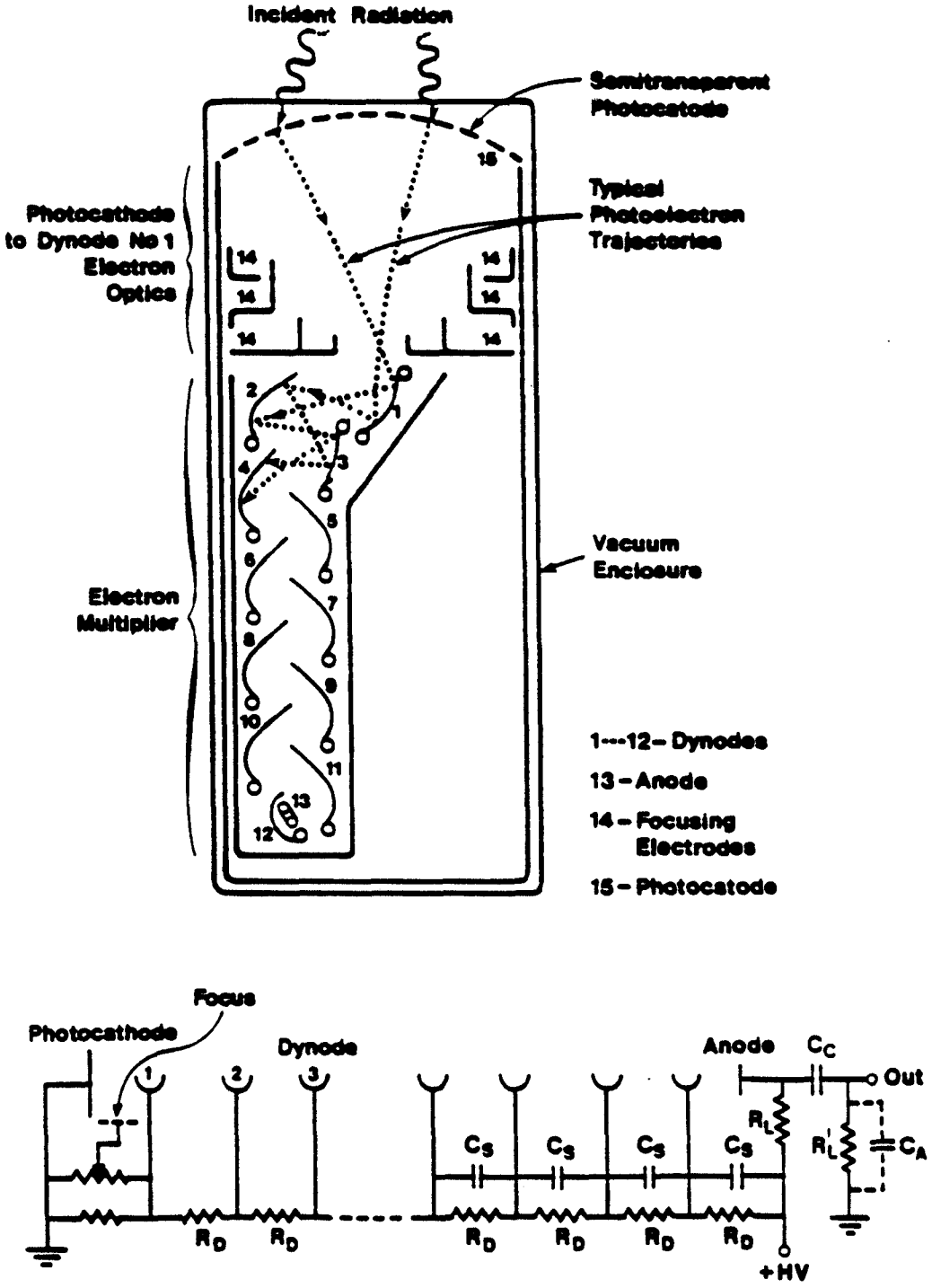

Figure 3-1: Schematic diagram of the structure and the circuit of PMT.

shells of the absorber atom. The electron energy is given by $E_e = E_\gamma - E_b$, where E_γ is the incident photon energy and E_b is the binding energy. The photoelectric probability increases strongly with Z of the material, scaling as Z^4 to Z^5[66]. The probability also is less important at higher energies. Unless the photoelectric absorption occurs near the detector surface, the energy of the incident photon is completely converted into detector electron energy and measured directly.

At higher energies the photon is likely to experience the Compton scattering process in which the incident photon collides with an electron, losing energy to the electron and scattering to a different direction. The energy of electron and the scattered photon are given by

$$E_\gamma = \frac{E_\gamma^i}{[1 + \frac{E_\gamma^i}{m_e c^2}(1 - \cos\theta)]} \tag{3.1}$$

$$E_e = E_\gamma^i - E_\gamma = E_\gamma^i \left[\frac{\frac{E_\gamma^i}{m_e c^2}(1 - \cos\theta)}{1 + \frac{E_\gamma^i}{m_e c^2}(1 - \cos\theta)} \right] \tag{3.2}$$

where E_γ^i is the incident photon energy, E_γ is the scattered photon energy, E_e is the electron energy, and θ is the angle between incident and scattered gamma ray. The maximum energy loss by the photon is for a head-on collision ($\theta = 180^0$) and is equal to

$$E_\gamma^i - E_\gamma = \frac{E_\gamma^i}{1 + \frac{m_e c^2}{2E_\gamma^i}} \tag{3.3}$$

Since all scattering angles can occur, a continuum of energies will be transferred to the electrons even for monoenergetic photons. A detector should be large enough to reabsorb all the Compton scattered photons.

Finally, at energies above about 3 MeV the pair-production becomes relevant. Pair production is the process in which a positron-electron pair is created in the field of a nucleus. The creation of the anti-matter positron is viewed as ejecting an electron from a negative energy state into a positive energy state, leaving a hole in the region of normally filled negative energy states. This hole is the positron. There is a gap of $2m_ec^2$ between two energy regions, so at least 1.022 MeV of energy is required to create an electron-positron pair. The photons resulting from

the annihilation of the positron may escape or be reabsorbed in the crystal. Thus all or some of the incident photon energy may be deposited in the scintillator. Even for a monoenergetic X-ray the pulse-height spectrum produced by the PMT pulses can be quite complex, depending on the energy deposited by the incident photons.

The probability of interacting with matter in one of these three processes can be expressed as a cross section or as an absorption coefficient. The attenuation coefficient μ for a beam of gamma rays is related to the number of gamma rays removed from the beam, either by absorption or scattering. In Compton scattering, the absorption cross section is determined by the energy absorbed by the electron, which is the total collision energy minus the average scattered photon energy. For all three processes, the total attenuation coefficient is the sum of the three partial attenuation coefficients. The μ/ρ, where ρ is the density, is plotted as a function of gamma ray energy in Fig. 3-2 for NaI[67].

3.1.3 The counting system

The rise of the pulse voltage from the PMT is related to the collection time of the charge, which has to be long enough to insure complete charge collection, while the decay time is the RC time constant characteristic of the preamplifier. Thus the preamplifier output pulse has a rise time ranging from a few nanoseconds up to a few microseconds and a long decay time of about 50 microseconds. The preamplifier should be placed close to the detector to reduce capacitance of the leads, which can degrade the rise time as well as lowering the effective signal size.

A spectroscopy amplifier shapes the pulse and further amplifies it. The preamplifier pulse having long decay time may not return to zero before another pulse occurs, so it is important to shorten it and only preserve the information in the pulse rise time. Several differentiation-integration circuits in series are used to first differentiate the pulse to remove the slowly varying decay time, and then integrate to reduce the noise. The result is a near-Gaussian shorter pulse whose

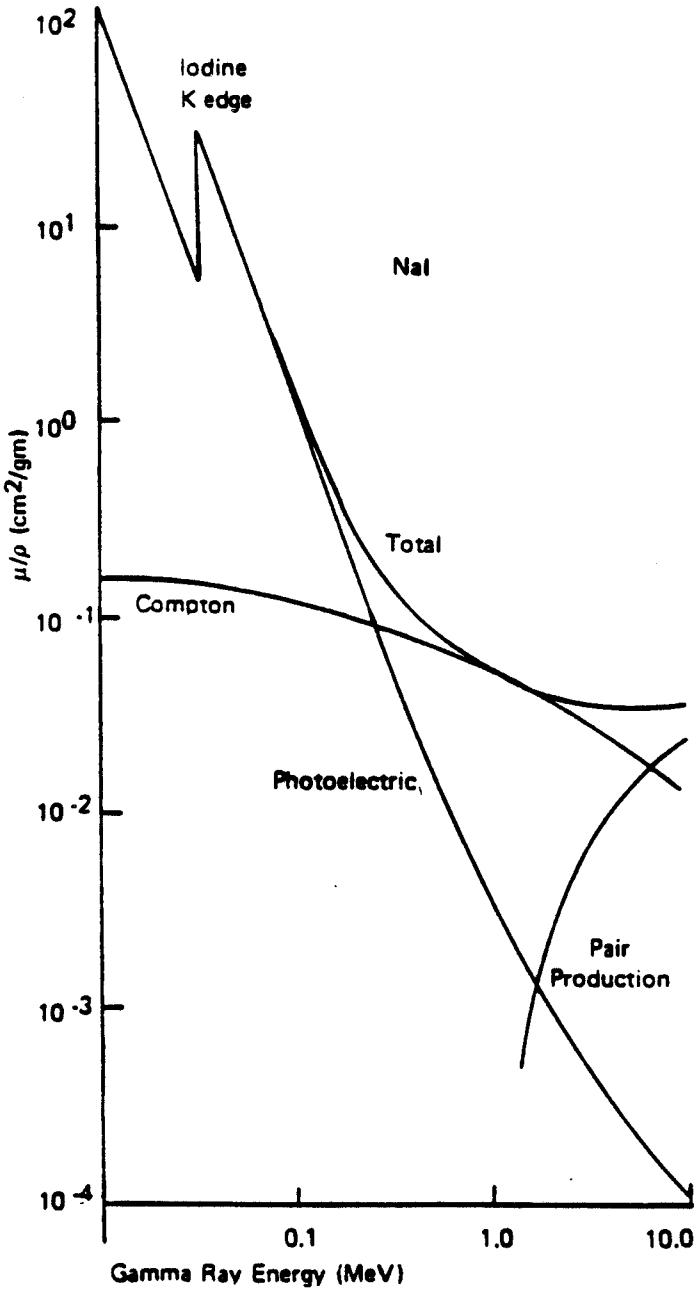

Figure 3-2: Absorption coefficients for NaI

amplitude is linearly proportional to the original incident X-ray energy. The output voltage ranges from 0 to 10 volts and the pulse width is about 1 microsecond for the system used here.

A pulse height analysis (PHA) technique counts the number of pulses having an amplitude that falls in a series of channels of constant-width dV at V. The number of counts in each channel would give a discrete approximation to the X-ray energy distribution being measured.

The pulses in a time interval determined by the experiment are separated by the multichannel analyzer (MCA) to provide an entire spectrum at once. An input pulse is checked to see if it is within the selected range by a single channel analyzer (SCA) and then passed to the analog-to-digital converter (ADC). The ADC converts the pulse into a digital number which is the address of a memory location, and one count is added to that location. while the ADC is converting a input pulse, a logic signal keeps a gate closed until the conversion is complete and the ADC is ready for another pulse. After collecting data for some period of time, the memory contents vs memory locations is equivalent to the X-ray spectrum. There are 512 channels in the system and 10 msec time interval is chosen for the data collection.

The total X-ray flux count rate as a function of time is measured for the experiments. The pulses from the spectroscopy amplifier are added over a specified time interval, 0.2 msec, and the resulting voltage is recorded. For the 500 msec period of discharge, 2,500 data points are collected and will be referred as hard X-ray signal(HXR) in this thesis. Fig. 3-3 shows the diagram of the X-ray detection system.

The major disadvantage of NaI(Tl) is the relatively long decay time of the output pulse width, a few microseconds. The count rate has to be kept below about 10^5 Hz or else the pile-up of multiple X-rays may distort the signal. A standard pulse pile-up rejection system is used to avoid the problem. Two pulses are produced for each scintillation, a slow one for linear pulse height analysis and

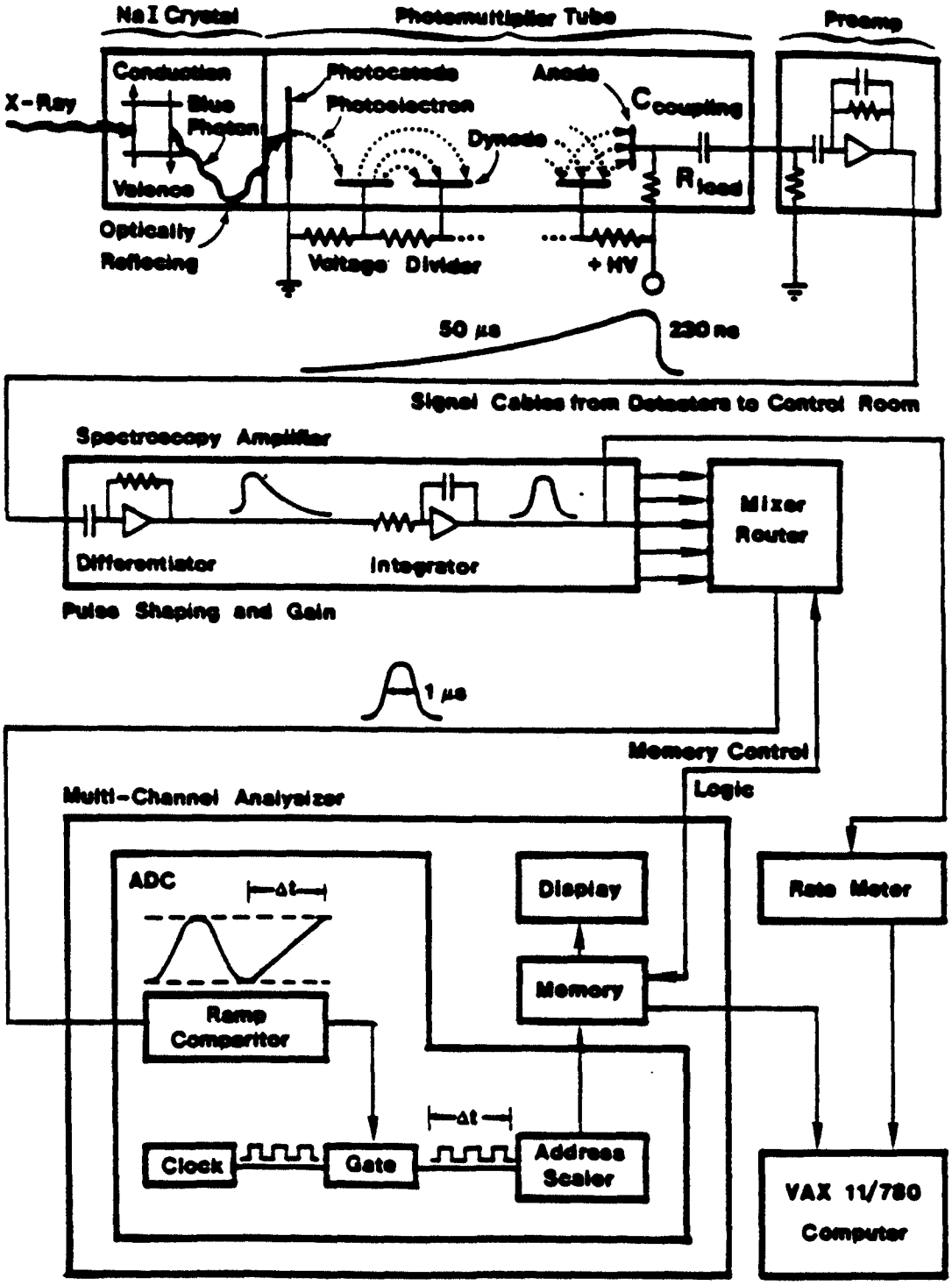

Figure 3-3: Block diagram of the X-ray detection system.

a fast one for pileup inspection. The pile-up inspection circuit checks to insure that only one pulse height signal goes through the circuit. If other pulses show up, the entire signal is gated out.

The energy resolution of the detector is typically 8% for the ^{137}Cs line at 662 keV and is roughly proportional to $\sqrt{E}/E$ where E is the incident X-ray energy. The spectrum is calibrated by using a Co-60 Gamma-ray source at 1.173 MeV and 1.332 MeV energies as in Fig 3-4. Two-point energy calibration is to determine both the offset and slope in the equation

$$E = A \times (Ch\#) + B \tag{3.4}$$

so that energy vs channel number can be directly read out.

3.2 Data analysis

The problem now is how to interpret the measured signal in terms of the original runaway electron distribution that generated the X-rays. The peeling-off method is the usual procedure applied, in which the highest energy is fitted first and then its contribution to the remaining part of the spectrum is subtracted, and so on. This method is tedious and inaccurate for lower energy parts. Here a numerical code DOG[14] is used for the data analysis.

In the preceding section the processes of the generation and detection of the X-rays are explained. In this section the numerical code used to simulate the processes is described and the relationship relating the experimental data to the runaway electron flux is discussed.

The generation of the X-rays is from the thick-target bremsstrahlung reaction. Barnes[14] created a data set for the thick-target bremsstrahlung differential energy cross section by assuming that the electrons would be normally incident on the material of impact and that all observations would be made in the forward cone of emission, specifically at 0°. The bremsstrahlung intensity for thick-targets

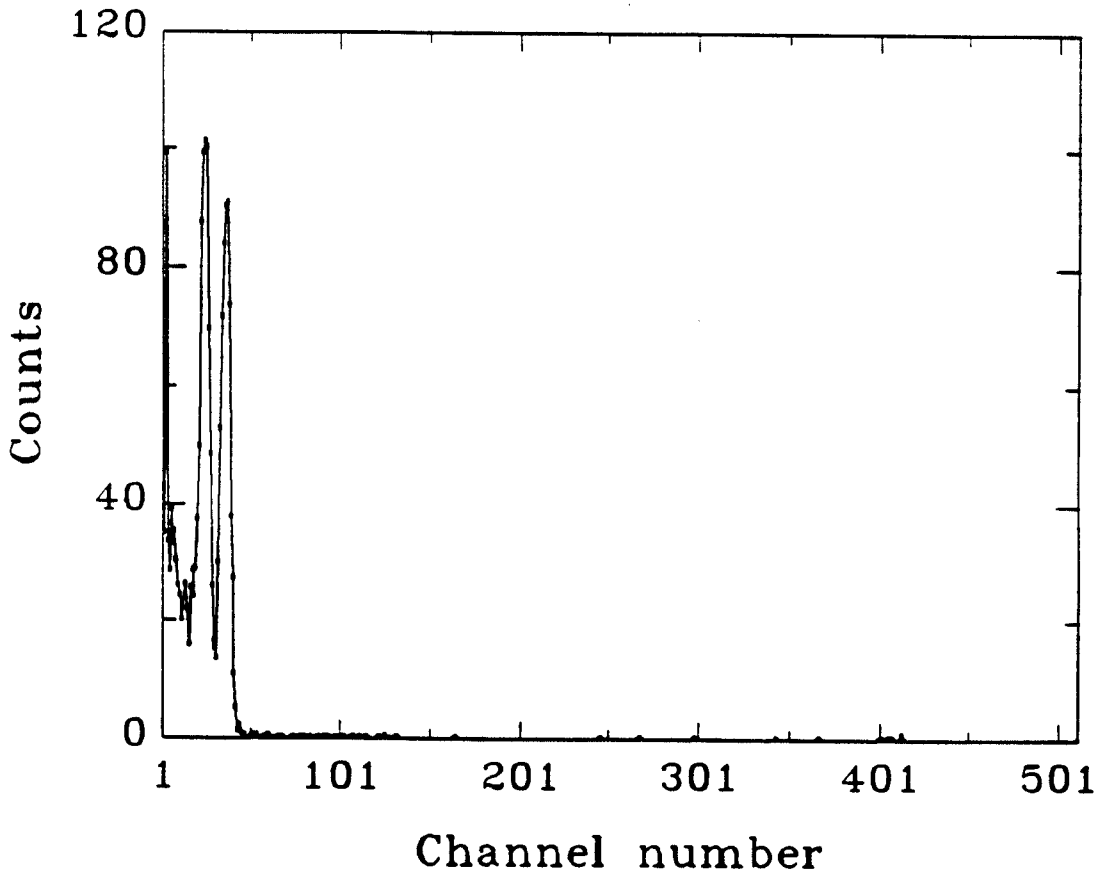

Figure 3-4: Energy calibration of the detector with a Co-60 Gamma-ray source at 1.173 MeV and 1.332 Mev energies.

is usually written as

$$k\frac{d\sigma}{dkd\Omega}(\text{MeV/MeV-ster-elec}) \tag{3.5}$$

Actually also differential in electron energy and hence having unit (MeV/MeV^2-ster-elec), it is the output energy in photons of energy k emitted by an incident electron of energy E. The emitted photons then go through various materials until they reach the detector and are detected. The probability of a photon of energy k being detected is

$$P(k) = e^{-\sum_i \mu_i(k)\rho_i h_i}(1 - e^{-\mu(k)\rho h_{det}}) \tag{3.6}$$

where μ is the absorption coefficient and ρh is the density-thickness product for the different absorbers i and the detector. The probability is the product of the probability of transmission through different materials, such as vacuum vessel, etc., and the probability of absorption by the detector material, NaI. The thickness of 5 cm steel is estimated to be the material shielding the detector and the result is shown in Fig 3-5.

The detector response is the contribution to the detector signal by a photon of energy k, and depends on the photon-to-pulse height response function R(p,k) as

$$D(k) = P(k)\int_{p_{lo}}^{p_{hi}} dpp^{\alpha}R(p,k) \tag{3.7}$$

where $\alpha = 0$ and p_{lo} and p_{hi} are the lower and upper bounds on the pulse heights for the counting rate in a single channel analyzer, and $\alpha = 1$, $p_{lo} = 0$ and $p_{hi} = \infty$ for a signal depending on the total energy deposited. Integrating this with the bremsstrahlung intensity over all photon energies gives the contribution to the detector signal by an electron of a given energy E

$$F(E) = \int_0^{\infty} dk\frac{kd\sigma}{dkd\Omega dE}D(k) \tag{3.8}$$

Multiplying this function by the electron energy flux distribution at a given time $\Gamma(E,t)$ gives the relative contribution to the signal by all electrons

$$S(E,t) = \Gamma(E,t)F(E) \tag{3.9}$$

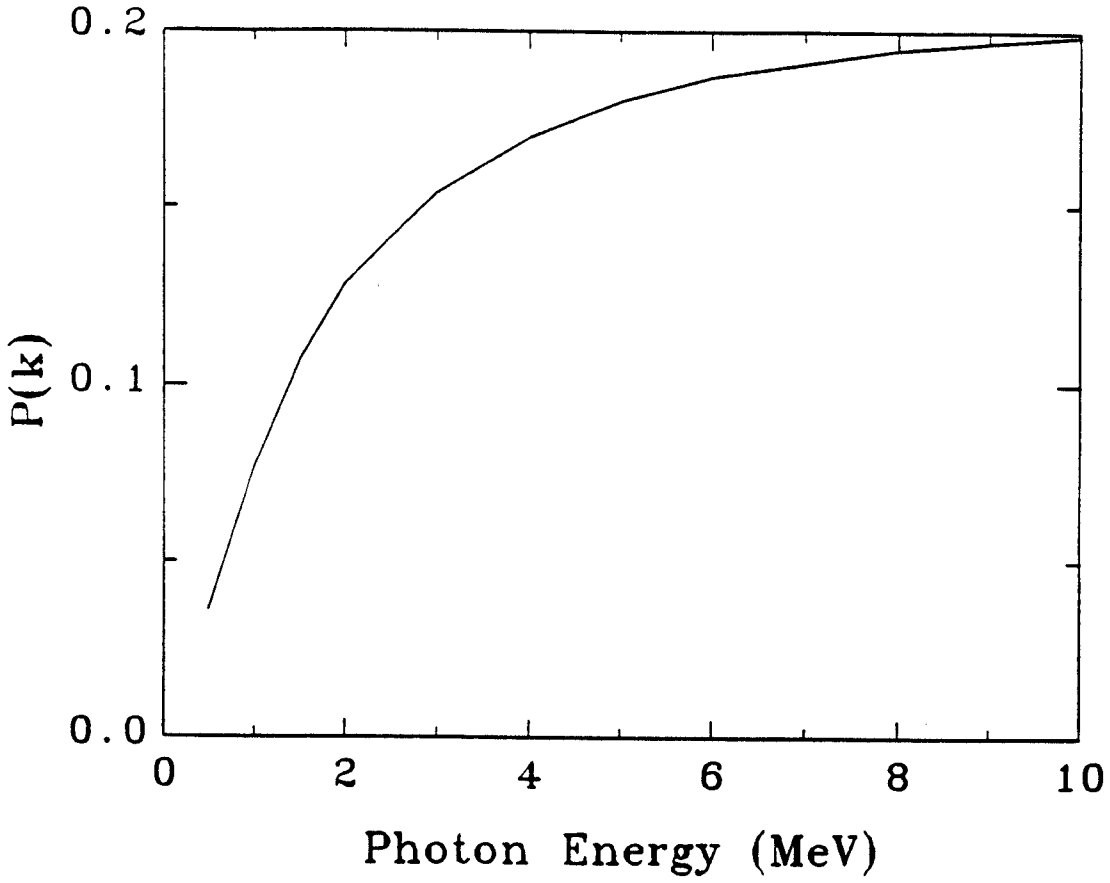

Figure 3-5: The probability of a photon of energy being detected by a 3 inch NaI detector, $P(k) = e^{-\sum_i \mu_i(k)\rho_i h_i}(1 - e^{-\mu(k)\rho h_{det}})$, vs. k. The thickness of 5 cm steel is estimated to be the shielding material.

The time dependence of the detector response can thus be calculated by integrating the relative contribution in electron energy

$$R(t) = \int_0^\infty dE\Gamma(E,t) \int_0^\infty dk \frac{kd\sigma}{dkd\Omega dE}(1 - e^{-\mu\rho h})e^{-\sum_i \mu_i\rho_i h_i} \int_{p_{lo}}^{p_{hi}} dpp^\alpha R(p,k) \tag{3.10}$$

which can be rearranged and rewritten as

$$R(t) = \int_{p_{lo}}^{p_{hi}} dpp^\alpha \int_0^\infty dk R(p,k)(1 - e^{-\mu\rho h})e^{-\sum_i \mu_i\rho_i h_i} \int_0^\infty dE\Gamma(E,t) \frac{kd\sigma}{dkd\Omega dE} \tag{3.11}$$

Eq. 3.11 is coded in DOG. There are two inputs for the code. The materials in between the limiter and the detector which are estimated to be about 5 cm steel is the first one. The other input for the code is the electron flux distribution $\Gamma(E,t)$. This distribution function can be written as $\Gamma(E,t) = \Gamma(t)f(E,t)$ where $\Gamma(t)$ is the particle flux and $f(E,t)$ is the energy distribution function which is assumed to have the exponential form e^{-E/E_0}, where $E_0 = E_0(t)$ is the electron energy index constant. As can be seen from the equation, the change in either the runaway electron particle flux $\Gamma(t)$ or its energy distribution function $f(E,t)$ can change the detector response $R(t)$. The energy spectrum of the detected signal is calculated as

$$SP(p,t) = \Gamma(t) \int_{k_{lo}}^{k_{hi}} R(p,k)(1 - e^{-\mu\rho h})e^{-\mu_s\rho_s h_s} \int_{E_{lo}}^{E_{hi}} dEf(E,t) \frac{kd\sigma}{dkd\Omega dE} \tag{3.12}$$

and the energy integrated signal

$$R(t) = \int_{p_{lo}}^{p_{hi}} dppSP(p,t) \tag{3.13}$$

where the labels lo and hi represent the chosen integration limits and the steel (μ_s, ρ_s, h_s) is the shielding material.The output photon energy spectrum $SP(p,t)$ can be fitted by an exponential form $e^{-E/E_{x0}}$, where E_{x0} is the X-ray energy index constant. Fig. 3-6 shows the electron energy spectrum as input and the corresponding X-ray energy spectrum from DOG. For each E_0, the corresponding E_{x0} and detector response are calculated and the relationships are plotted in Fig. 3-7.

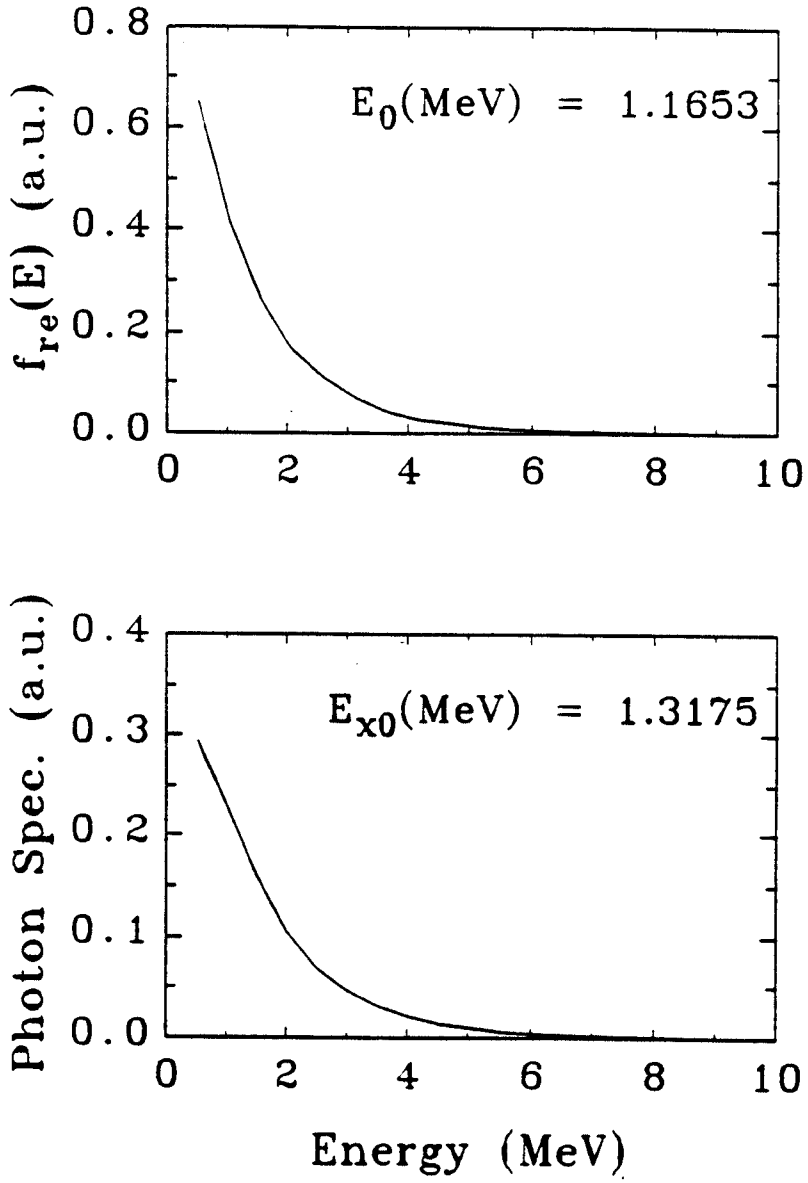

Figure 3-6: The input electron energy spectrum having the form e^{-E/E_0} and the corresponding X-ray energy spectrum, which can be fitted with the form $e^{-E/E_{x0}}$, calculated by the code DOG.

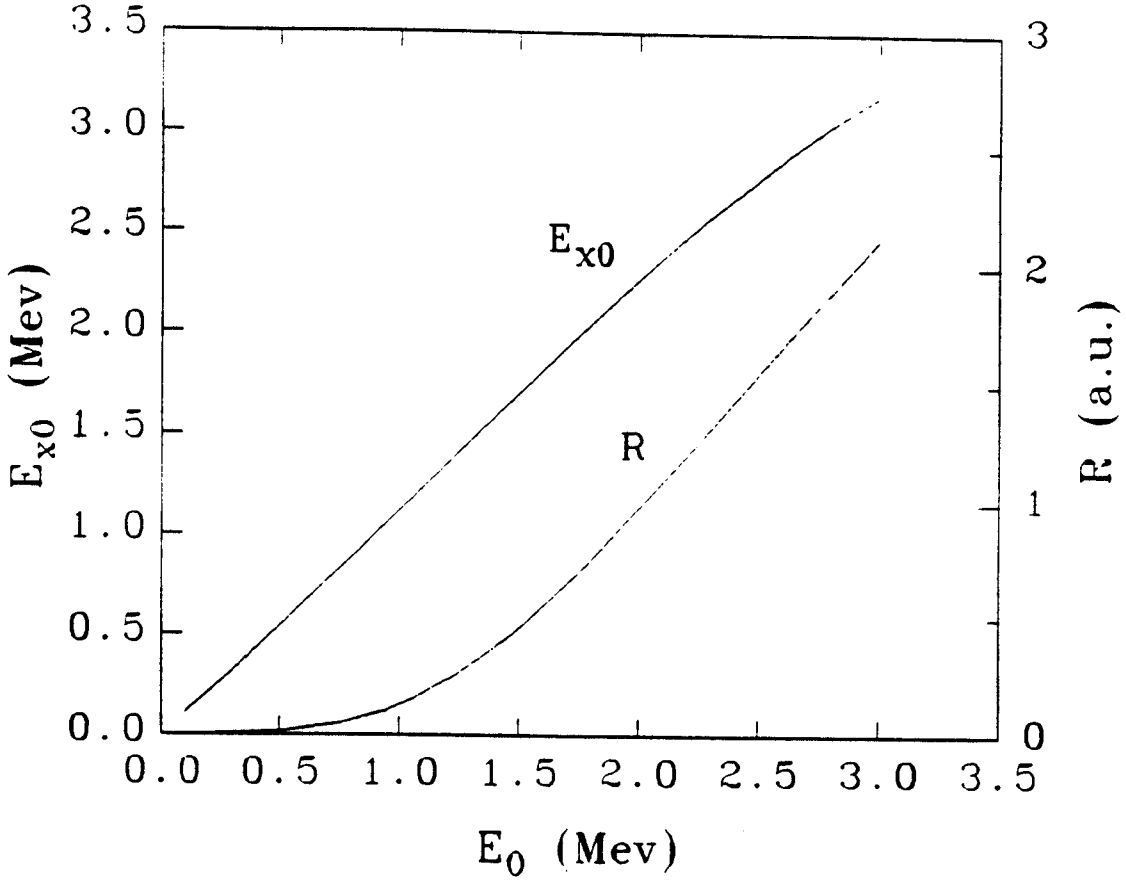

Figure 3-7: The relationship of the runaway electron E_0 and the E_{x0}, $R(t)$ of the X-ray as calculated by DOG.

The hard X-ray energy spectra, E_{x0}^{exp}s and $R^{exp}(t)$ are measured in experiment. Two different experiments are performed using different perturbations on the plasma to study the runaway electron transport. By comparing the measured E_{x0}^{exp}s with and without the perturbations, the change in E_{x0}^{exp} due to the perturbations can be found. If this change is negligible, the observed change in detector response due to the perturbations, $\triangle R^{exp}(t)$, can be assumed to be proportional to the change of the runaway electron particle flux to the limiter, $\triangle\Gamma(t)$,

$$\triangle\Gamma(t) \propto \triangle R^{exp}(t) \tag{3.14}$$

Nevertheless, if there is a change in E_{x0}^{exp}, $\triangle E_{x0}^{exp}$, caused by the perturbations, its contribution to $R(t)$ has to be considered to figure out $\triangle\Gamma(t)$. Fig. 3-7 is used to find the corresponding change in $R(t)$, $\triangle R^{\triangle E_{x0}^{exp}}(t)$. It can be written as

$$\triangle\Gamma(t) \propto \frac{\triangle R^{exp}(t)}{\triangle R^{\triangle E_{x0}}(t)} \tag{3.15}$$

The next chapter will discuss the experimental results. The observed hard X-ray signal will be processed as just described and the runaway electron flux to the limiter change $\triangle\Gamma(t)$ due to different perturbations applied in experiment will be obtained. The runaway electron diffusion coefficient can then be found by comparing $\triangle\Gamma(t)$ to the analytical and numerical solutions.

Chapter 4

Experimental results

Two experiments, using different perturbations on the plasma, have been performed on TEXT to study the runaway electron transport : (i) displacing the plasma column inward, and (ii) externally applying resonant magnetic fields. The discharge parameters for this study are $B_T = 2.0$ T, $I_p = 195$ kA, $\bar{n}_e = 2.0 \times 10^{13}$ cm^{-3} (the line averaged density), and $q_a = 3.5$. In this chapter, the experimental results for the normal discharges with no applied perturbations are discussed first. Both the energy spectra and the time-integrated signal of the hard X-rays are observed. The model that most of the runaway electrons are created in the center of the plasma and in the early stage of the discharge is in agreement with the experimental observations.

Zweben, Swain, and Fleischmann[40] shifted the plasma column inward by an amount Δs to study the radial transport of runaway electrons near the edge on ORMAK. An anomalous diffusion coefficient was needed to explain the gap in the observed hard X-ray signal. This diffusion coefficient was inferred for the edge region. The same technique is used on TEXT. The sudden increase in the vertical magnetic field moves the plasma column inward 2–3 cm such that an extra distance is created for the runaway electrons to diffuse to the limiter. The dip in the hard X-ray signal caused by the shifting of the plasma column is observed and will be explained by the analytical and numerical models, which are not the

same as the one used by Zweben, Swain, and Fleischmann and will be discussed in the next chapter.

The magnetic perturbation experiment uses externally generated resonant magnetic fields to perturb the magnetic surfaces in the edge region of the plasma. The resonant fields, with toroidal mode number n = 2 and dominant poloidal mode number m = 7, produce magnetic islands and stochastic region at the plasma edge ($r/a \geq 0.8$) without affecting the interior. The original ideas of designing this magnetic structure are reviewed. A numerical code is used to calculate the Poincarè plot of the magnetic field. The poloidally and toroidally averaged ratio of radial to toroidal field components is $< |b_r|/B_\phi > \approx 0.1\%$. The response of the hard X-ray signal to this magnetic perturbation is observed and analyzed.

In order to understand the response of the hard X-ray signal due to perturbations, the signal with perturbations needs to be known first. The next section describes the hard X-ray signal behavior for normal ohmically heated discharges without perturbations.

4.1 General results

The number of runaway electrons generated in a discharge depends on the operating conditions early in the discharge. The techniques of generating or eliminating runaway electrons in a discharge include programming the initial gas fill rate, current ramp-up rate, loop voltages, and maintaining clean walls, etc. The number of runaway electrons are usually kept low in a discharge because they might cause damage to the wall. In TFR[68, 69] runaway electron beams which were trapped by toroidal field ripples and forced to move on unconfined orbits pierced the stainless steel vacuum vessel. The high runaway electron contents during the discharges were mainly caused by the low density operation of the device. To study their transport, an adequate level of hard X-rays is generated and, with the same operating conditions, is quite reproducible for the discharges. It is neces-

sary to average over 5-10 shots for the hard X-ray signal in order to have good statistics.

Fig. 4-1 shows the loop voltage, plasma current, line averaged electron density, and Mirnov oscillation for the typical discharge with no perturbations. The hard X-ray signal averaged over several shots with the same plasma conditions is shown in Fig. 4-2. This time behavior is typical of normal ohmically heated discharges on TEXT. The signal starts at zero level, has a small burst caused by the instability during the current ramp-up phase of the discharge as shown by the Mirnov signal in Fig 4-1, rises rapidly in the next $\sim$ 150 msec, and then reaches nearly a plateau till the end of the discharge.

The low hard X-ray signal in the first 50 msec can be explained by assuming that most of the runaway electrons are created at the center of the plasma so that it takes a certain amount of time for them to diffuse out. Once the runaway electrons reach the edge, the signal starts to rise rapidly. The runaway electrons then relax to a slower time evolution mode and the faster time responses decay away, and a nearly plateau state shows up. The perturbations are turned on only after the hard X-ray signal has reached the state of nearly a plateau.

If the plasma column is pushed outward at the beginning of the discharge, most of the runaway electrons are dumped at the limiter as can be seen by the burst in the hard X-ray signal in Fig. 4-3 . The plasma conditions are then the ones as shown in Fig. 4-1. The hard X-ray signal is zero through the end of the discharge. The observation of this discharge and the importance of early discharge conditions in determining the number of runaway electrons generated are in agreement with the early creation model which assumes that most of the runaway electrons are created in the early stage of the discharge. The runaway electrons created during the discharge are negligible because the time left in the discharge after the burst in Fig. 4-3 should be long enough for these runaway electrons to diffuse out and to be detected.

The energy spectra of the hard X-ray are also measured and fitted with a

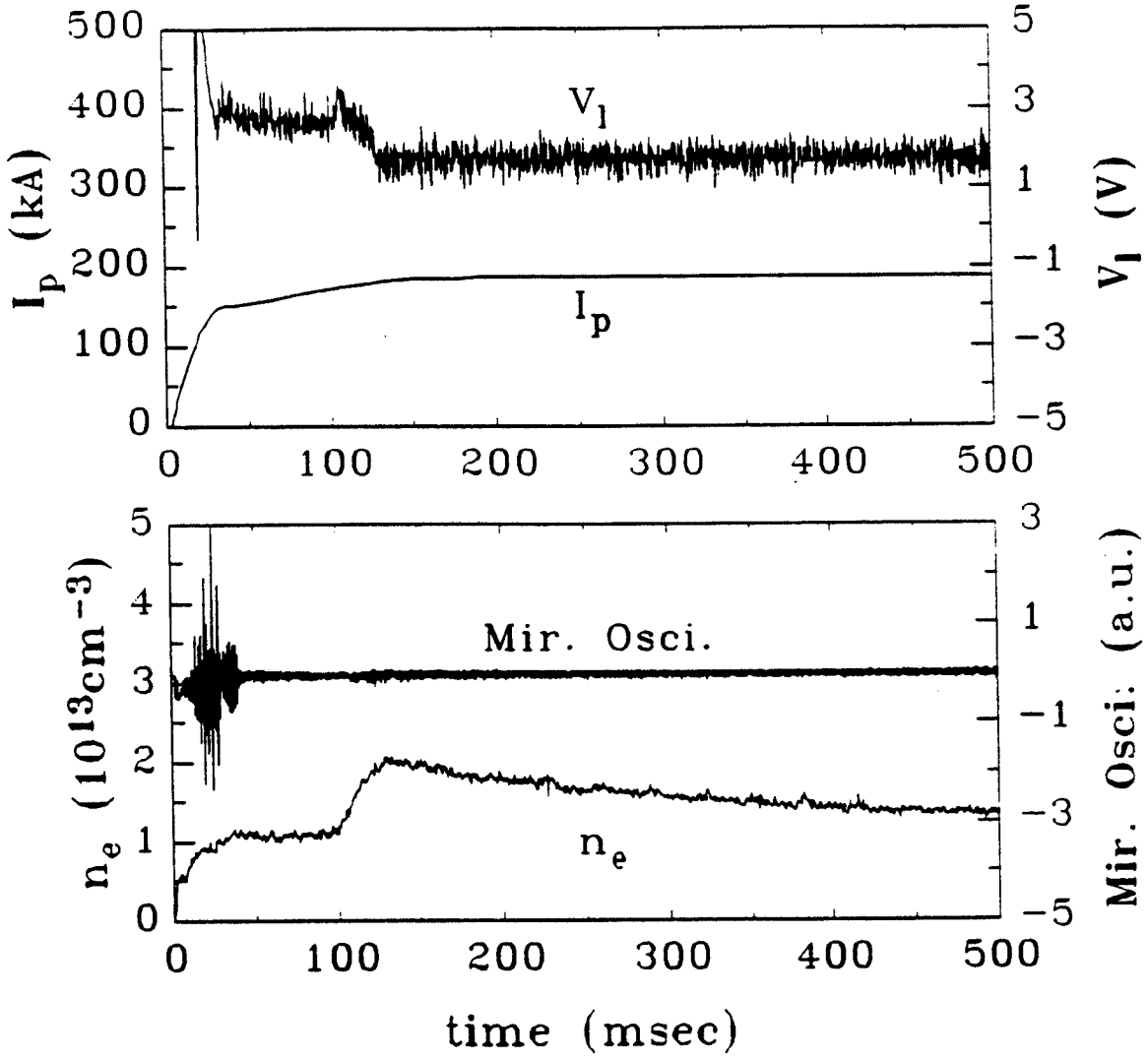

Figure 4-1: Loop voltage (V_l), plasma current (I_p), line averaged electron density (n_e), and Mirnov oscillation for the typical discharge (shot 149248) with no perturbation.

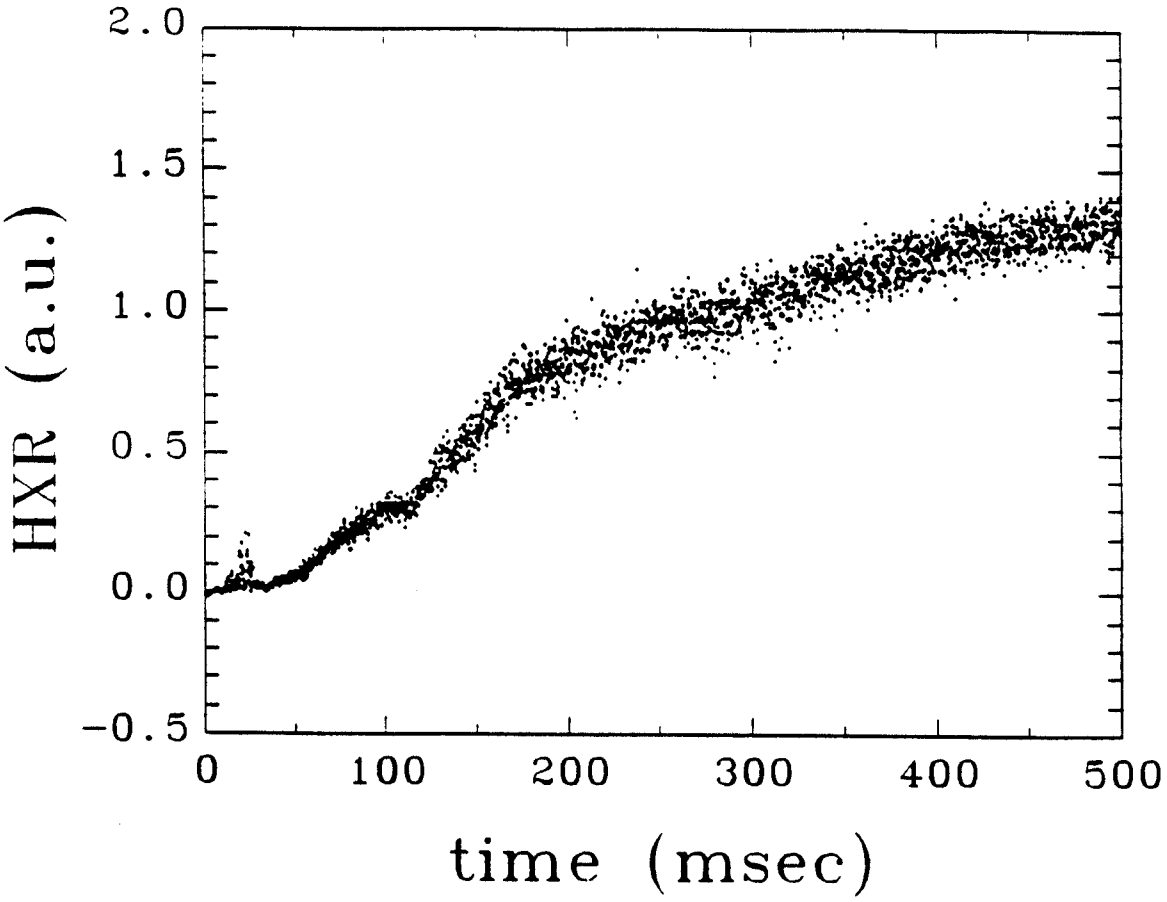

Figure 4-2: Hard X-ray signal (HXR) averaged over 19 shots starting from shot 149248 with no perturbation.

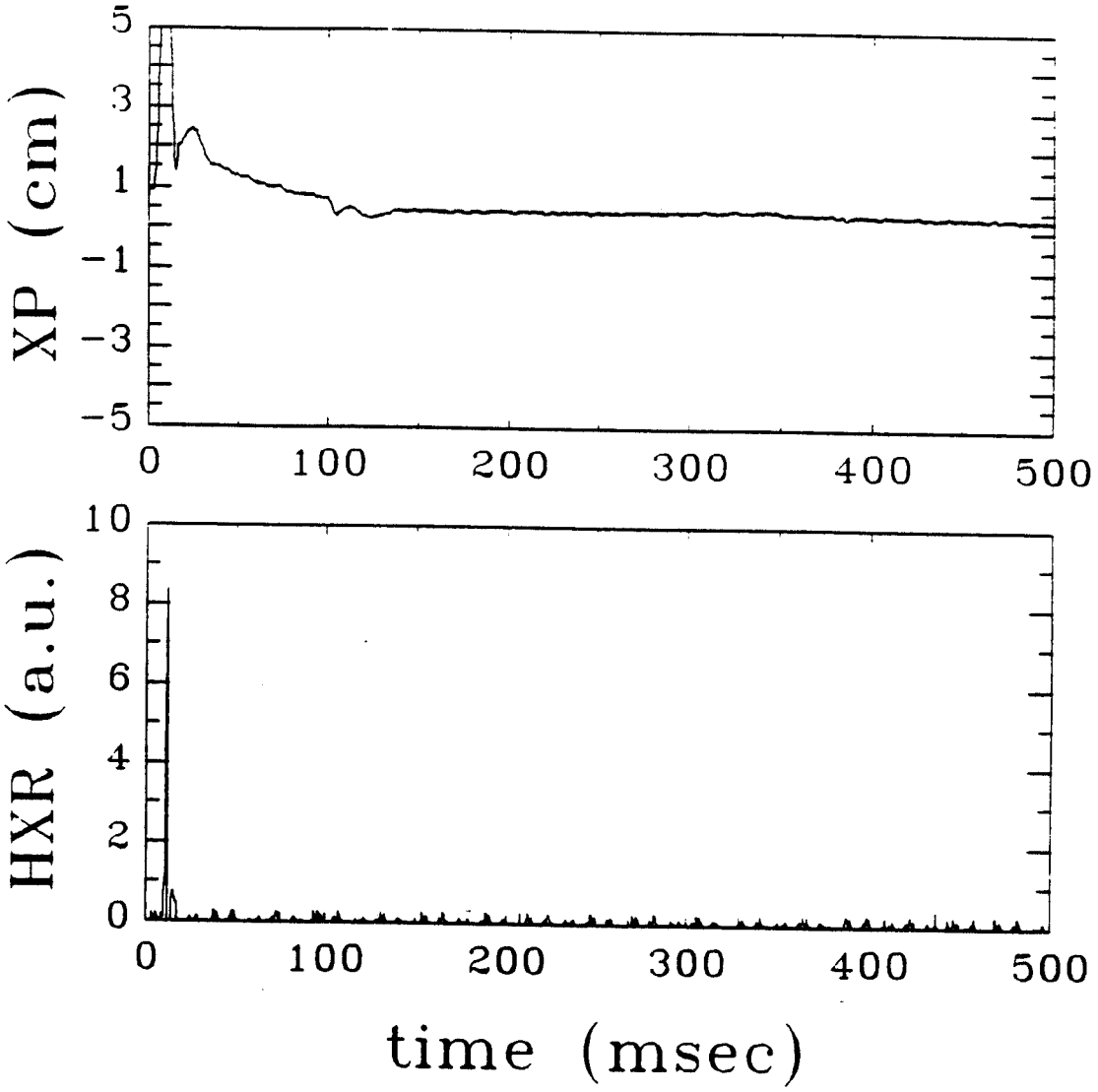

Figure 4-3: Plasma position (XP) and hard X-ray signal (HXR) (shot 149204) show that the plasma is moved outward and most of the runaway electrons are depleted, the burst in HXR, in the beginning of the discharge. After the initial burst, HXR stays low for the rest of the discharge.

functional form $e^{-E/E_{x0}}$, where E_{x0}, the energy index, is a constant. Fig. 4-4 shows the spectra and the fitting function, the solid curves, at four different time intervals. It also shows how photons of gradually higher energy are seen at later and later times. Since photons of a given energy can only be radiated by electrons of greater energy, the time when such photons are first seen is a measure of when electrons first reach that energy. The energy increase in the first $\sim$ 200 msec shows an approximately linear acceleration in this relativistic regime. However, the increase is much less than allowed by acceleration due to the loop voltage. Fig. 4-5 shows the time evolution of E_{x0}.

The slower energy increase rate suggests an energy loss process experienced by the runaway electrons since only little frictional drag on MeV electrons would be expected. For a runaway electron, it can only lose its energy by radiation, which removes energy at a higher rate as the electron energy increases, or by some instability of resonant interaction which increases its perpendicular energy. The synchrotron radiation rate[70] for an electron moving on a curved path of curvature R_{cur} is

$$P_{rad} = \frac{e^2 c}{6\pi\epsilon_0}\frac{\gamma^4}{R_{cur}^2}(\frac{v}{c})^4 \approx 4.613 \times 10^{-20}\frac{\gamma^4}{R_{cur}^2} \tag{4.1}$$

where R_{cur} is the radius of curvature of the electron trajectory which is approximately equal to R_0, the major radius, if the perpendicular component of the runaway electron velocity is negligibly small. For a 10 MeV runaway electron, the power loss by synchrotron radiation is much smaller than the power absorbed from the electric field of the loop voltage V_l, $eV_lc/2\pi R_0$. If the perpendicular component is included, the average radius of curvature for a particle with an average perpendicular velocity fraction can be estimated by

$$R_{cur} = \frac{1}{[\frac{(1-f^2)}{R_0} + \frac{eB_0 f}{m_e c\gamma}]} \tag{4.2}$$

and the limiting value of gamma can be written as

$$\gamma = [\frac{1.66 \times 10^8 R_{cur}^2 V_l\sqrt{1-f^2}}{R_0}]^{1/4} \tag{4.3}$$

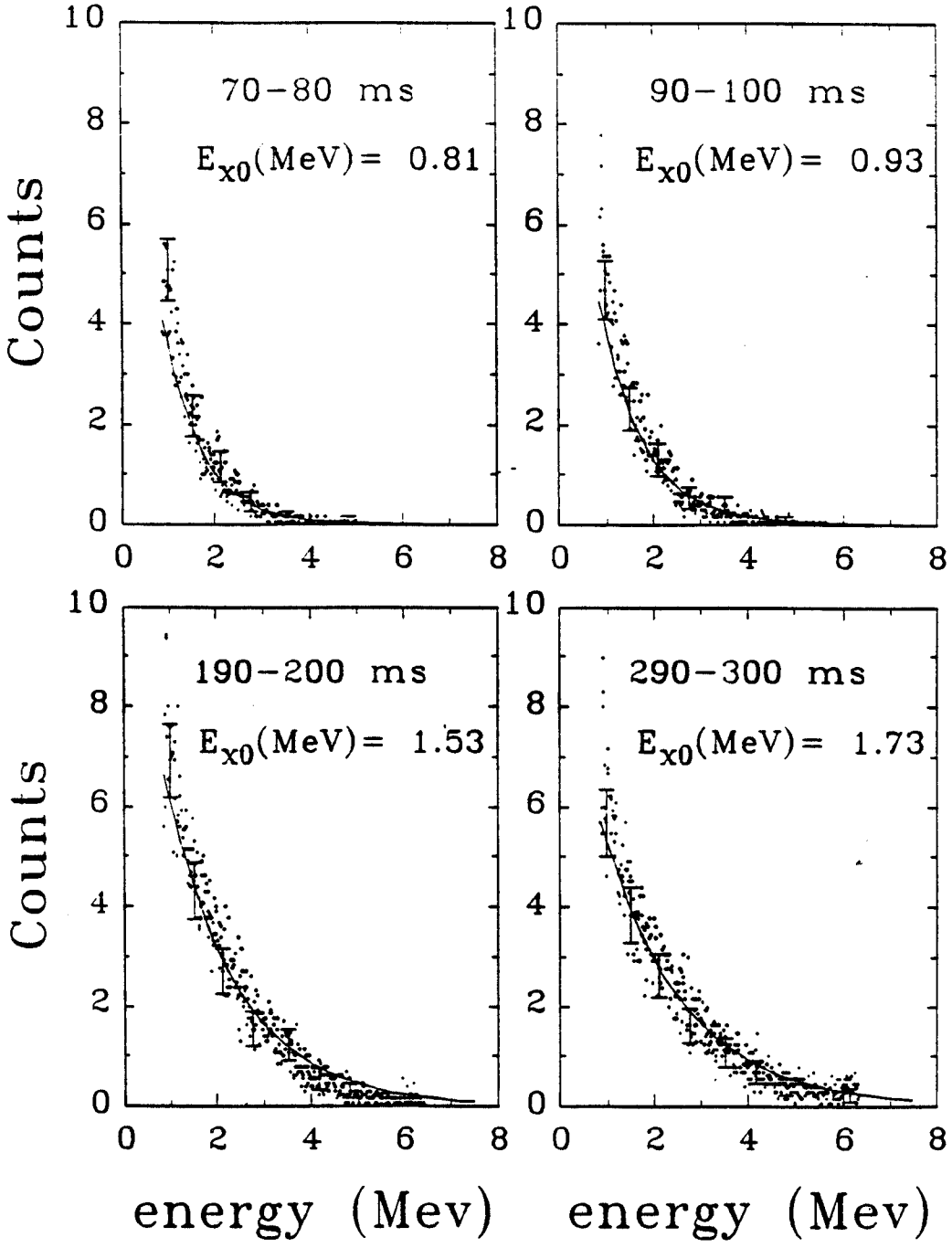

Figure 4-4: Energy spectra of the hard X-ray and the fitting function $e^{-E/E_{x0}}$, the solid curves, at four different time intervals.

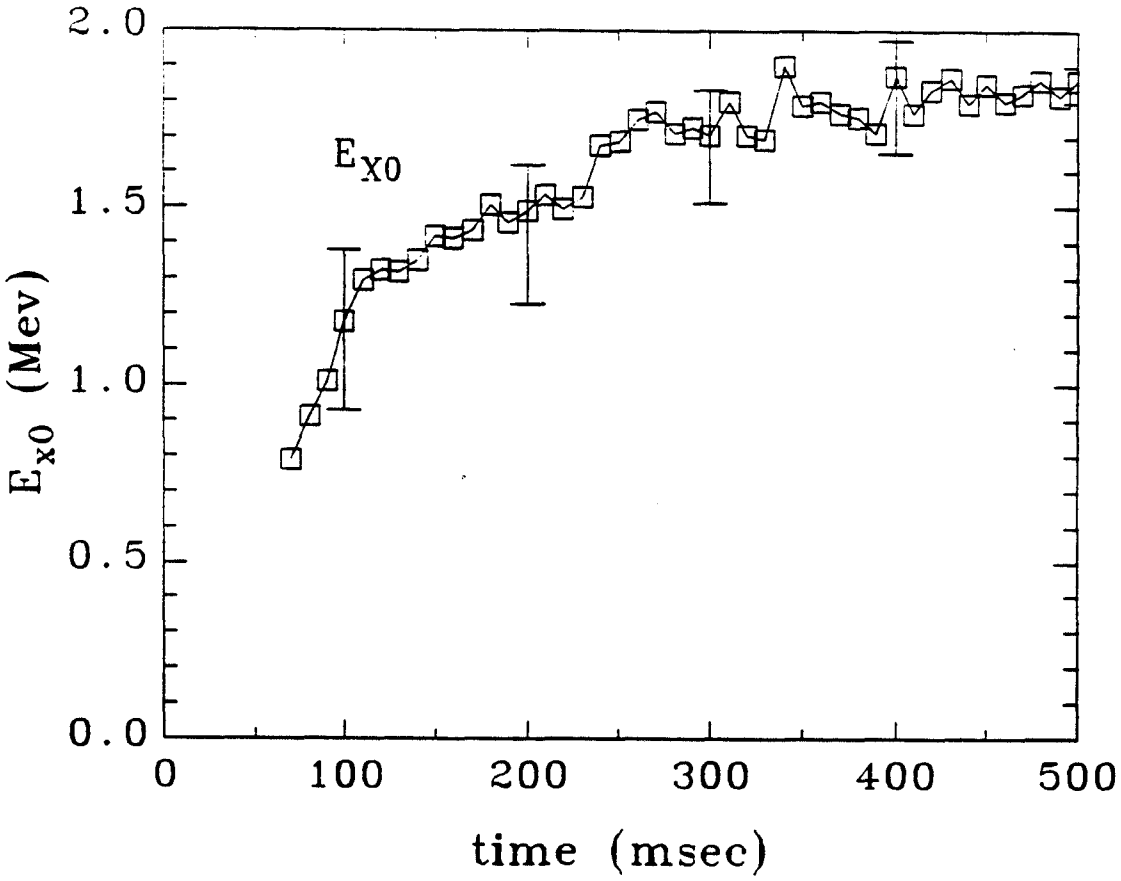

Figure 4-5: The time evolution of the energy index constant E_{x0} averaged over 8 shots starting from shot 168874 for the discharges without perturbation.

If the perpendicular velocity fraction f were to increase, the radiation limiting value would decrease.

The instability due to the anomalous Doppler effect could increase the perpendicular velocity fraction. The instability develops if the electron velocity exceeds the value

$$v \geq 3(\omega_c/\omega_p)^{3/2} v_c \tag{4.4}$$

where $\omega_c = eB/mc$, $\omega_p = \sqrt{4\pi ne^2/m}$, and v_c the critical velocity[46]. The corresponding electron energy on TEXT is $\sim$ 0.5 MeV. The scattering of electrons would occur without energy loss, while the isotropization would enhance the synchrotron radiation. The radiation limit γ decreases from 125.6 to 22.0 as the value of f goes from 0 to 0.5.

The combination of these two effects, the isotropization of electrons due to the anomalous Doppler effect and thus the enhanced synchrotron radiation, could be very well responsible for the experimentally observed slower energy increase rate. Russo[71] also suggested that the interactions with magnetic field ripple may induce an energy loss process for the runaway electron.

4.2 Position shift experiment

The technique of applying a sudden inward shift of the plasma column by programming the vertical magnetic field waveform is used to study the runaway electron transport. As illustrated in Fig. 2-3, the drift surfaces for the high energy electrons in axisymmetric plasma are displaced from the flux surfaces toward the outboard side. As runaway electrons leave the discharge, the intersection with the limiter occurs at the outside of the limiter. The sudden inward shift of the plasma column pulls all the runaway drift surfaces away from the outside of the limiter. An extra distance is then created for the runaway electrons to diffuse with a larger outmost drift surface before they see the limiter as shown in Fig. 4-6. However, the distance of the inward shift must be short enough that the runaway electron drift

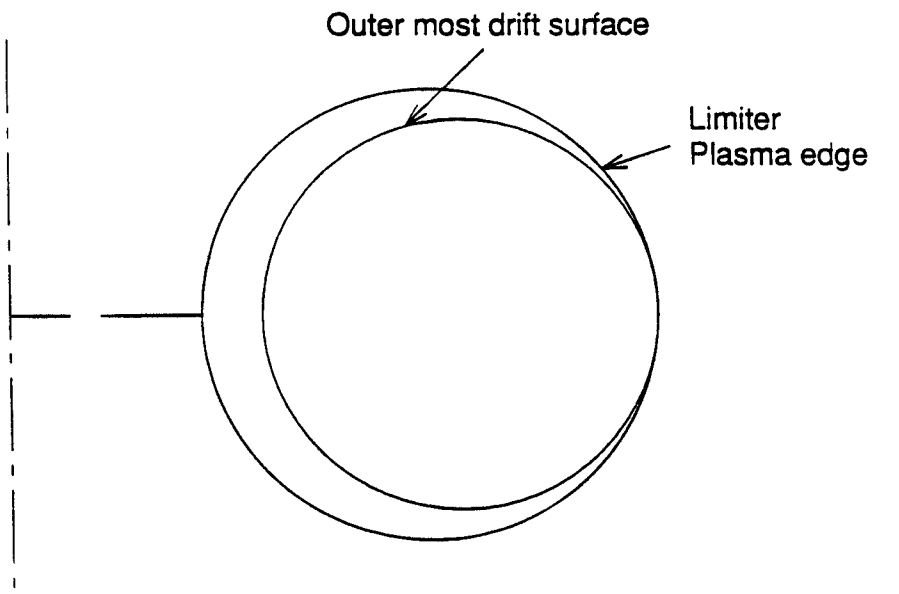

Before the shift

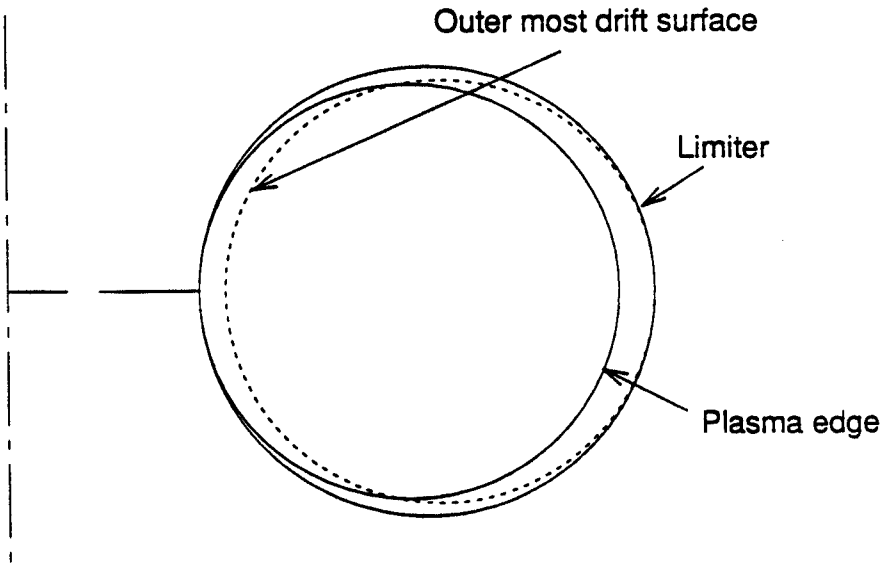

After the shift

Figure 4-6: The plasma position and the outmost drift surface of the runaway electron before and after the shift of the plasma column.

surface does not touch the inner side of the limiter. To insure this, hard X-ray emission at the inner side of the limiter is monitored by a second NaI detector.

The plasma column is shifted after the hard X-ray has reached the a near plateau state. The response of the hard X-ray signal to the shift depends on the speed of inward motion of the plasma column. It is necessary to move the plasma inward fast enough to see a drop in the hard X-ray signal, but sufficiently slow that no instabilities develop in the plasma. Fig. 4-7 shows the position change monitored in the usual way using sine, cosine and saddle coils and the corresponding speed by taking the time derivative. Because it takes longer for the runaway electrons to get out, there is an initial drop in the hard X-ray signal.

The plasma current is unchanged as shown in Fig. 4-8. Also shown is the loop voltage which changes due to the motion of the plasma shift. The loop voltage is the average of four voltages measured with four single-turn pick-up coil wound at inner upper, inner lower, outer upper, and outer lower positions close to the torus. The shift moves the plasma toward the inner coils and away from the outer coils; the flux changes are then picked up by the four coils. The runaway electron energy is proportional to the integration of the loop voltage which changes little as shown in the Fig. 4-8. So the runaway electrons are not affected by the plasma shift. The drop in the hard X-ray signal is simply caused by the longer distance created for the runaway electrons to diffuse. Since the runaway electrons are kept in the plasma longer because of the increased confining dimension, their energies should also increase if there is no energy loss mechanism involved. For a normal discharge without perturbations, the confinement time is

$$\tau_a = \frac{a^2}{4D} \tag{4.5}$$

With the extra distance $\triangle s$ created, the confinement becomes

$$\tau_{a'} = \frac{a'^2}{4D} = \frac{(a+\triangle s)^2}{4D} \tag{4.6}$$

where a is the plasma radius and D is the runaway electron diffusion coefficient.

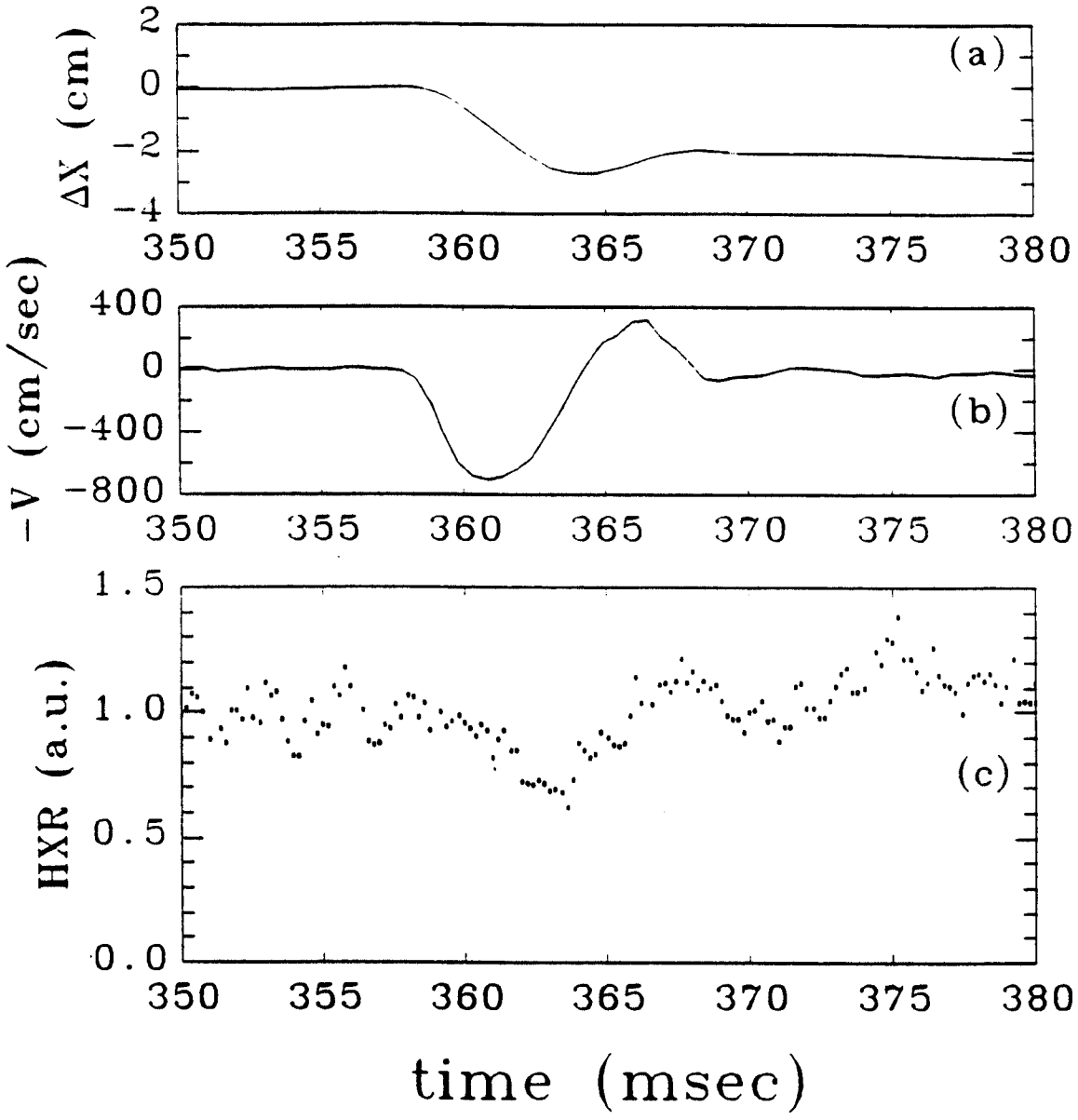

Figure 4-7: Plasma position change (ΔX), the corresponding speed (-V = dΔX/dt), and the hard X-ray signal (HXR) averaged over 14 shots starting from shot 159465 for the position shift experiment.

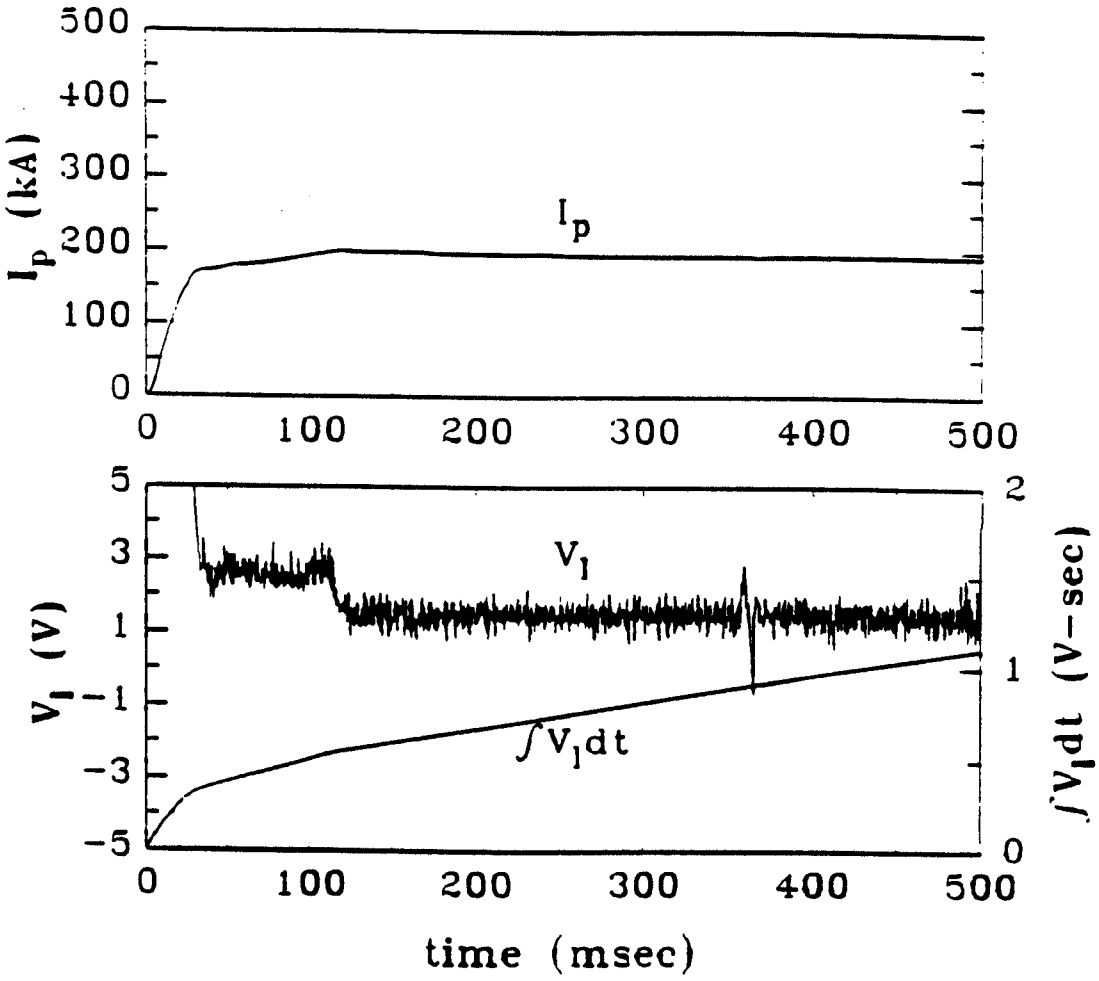

Figure 4-8: Plasma current (I_p), loop voltage (V_l), and the time integration of V_l ($\int V_l dt$) for the position shift experiment.

The ratio of the increased confinement time to τ_a is then

$$\frac{\triangle\tau}{\tau_a} = \frac{\tau_{a'} - \tau_a}{\tau_a} \approx \frac{2\triangle s}{a} \tag{4.7}$$

for $\triangle s \ll a$. The ratio is $\sim 1/6$ with $a = 26$ cm and $\triangle s = 2$ cm. The extra energy gain caused by the shift motion should be approximately equal to 1/6 of the runaway electron energy without the perturbation, which is > 1 MeV, since the energy is approximately linearly proportional to time, Eq. 2.13. However, the measured energy spectra show negligible change due to the shift motion as shown in Fig. 4-9. The discrepancy can be explained by : (i) some energy loss mechanisms impose an upper bound for the energy of the runaway electrons, (ii) the increased time due to the shift motion is much less than that calculated. The first reason has already been seen with the lower energy increase rate for the normal discharge as discussed in the preceding section. The second reason is related to the diffusion coefficient D which is assumed to be a constant in the calculation. If D is a function of the radius, which peaks sharply at the edge as will be discussed in the next chapter, the $\triangle\tau$ could be much less. Both effects would limit the energy gain due to the shift. Nevertheless, the hard X-ray signal change is then considered to be proportional to the change of the runaway electron flux to the limiter because of the small change in the hard X-ray energy spectra.

4.3 Magnetic perturbation experiment

An externally generated magnetic field is used to study the runaway electron transport. Because of their high energies, runaway electrons are considered to be collisionless and their transport due to the magnetic perturbations may contain important information on the anomalous transport of collisionless particles. With the externally generated magnetic fields, the response of the runaway electrons should give valuable informations. The EML (Ergodic Magnetic Limiter) coils are used to generate the perturbing fields.

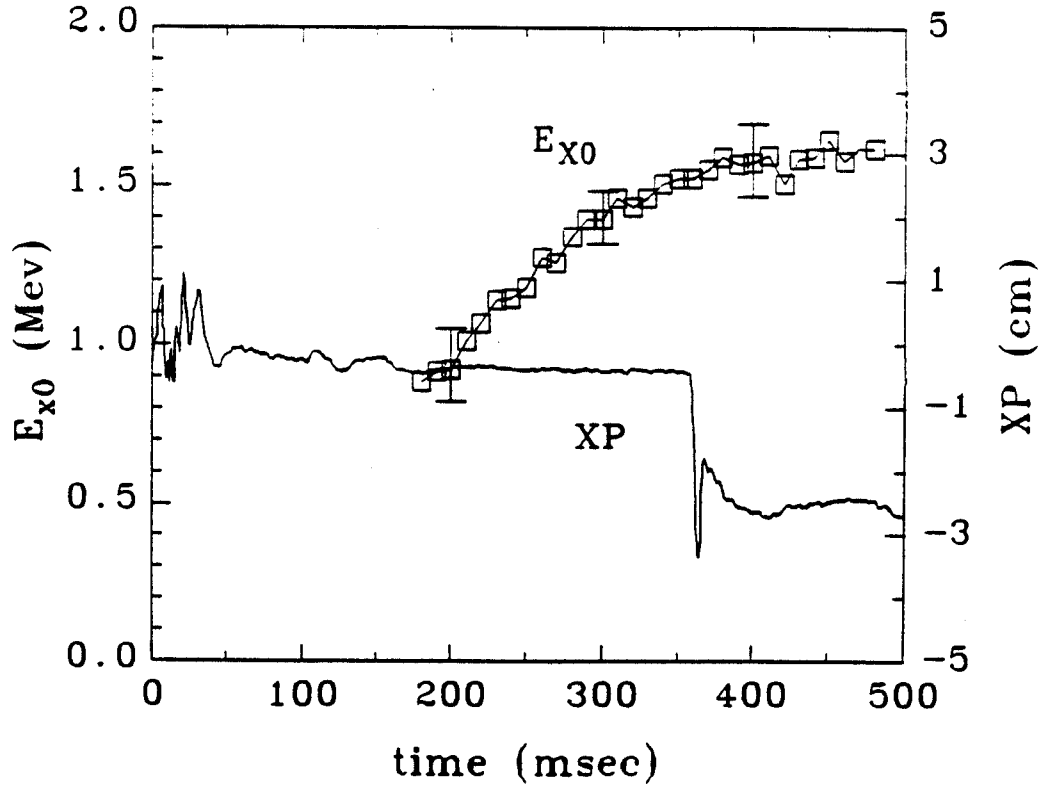

Figure 4-9: The energy index E_{x0} as a function of time for the position shift experiment. The plasma column is shifted inward at 358 msec.

4.3.1 Original ideas of EML experiment

The plasma in tokamaks is confined in the toroidal vacuum chamber by the magnetic fields. The purpose is to make the plasma temperature and density high and the confinement time long enough to generate power from the fusion reactions. The confinement of the particles and the heat is not perfect and plasma-wall-interaction is a very important issue in the fusion devices. This interaction would not only damage the wall but also generate impurities. The accumulation of impurities and the accompanying radiative losses may cause serious obstacles to achieving reactor grade plasmas. The heat load on the limiter is also a concern.

To minimize the problems, one needs to keep the boundary-layer temperature as low as possible to get below the threshold values of critical plasma-wall-interaction processes and to distribute the heat flux emerging from the plasma core over a large area. The application of a helical magnetic field on the edge layer of the plasma was proposed for these purposes [72, 73, 74, 75, 76].

This externally applied magnetic field is resonant with the equilibrium magnetic surfaces in the edge layer. Magnetic islands or stochastic field are produced. A layer of ergodic surfaces surrounding the hot plasma is then used to control the particle and heat fluxes at the edge of the tokamaks. The configuration has been called an ergodic magnetic limiter (EML)[74]. This technique has demonstrated beneficial effects in terms of a reduction in the thermal loading of the pump limiter's plasma facing surface on the TORE-SUPRA tokamak [77, 78].

On TEXT[79, 80, 81, 82, 83, 84, 85], using a m = 7, n = 2 or 3 resonant magnetic fields, braided patterns in H_α light from the limiter are produced. Edge temperature drops at r/a=0.92 by 30%, and reduced central impurity emission and reduced total radiated power are reported. Edge thermal transport[84] is enhanced in the presence of stochastic magnetic fields. However, the plasma particle transport[85] is increased by only 30% in the presence of magnetic islands.

The structure of the magnetic fields in tokamaks is very important for the runaway electron transport studies. Magnetic fluctuations inside a plasma are

often suggested to be responsible for the runaway electron diffusion[59, 58, 86]. Here, the known magnetic perturbations are imposed on the plasma and the response of the runaway electrons is observed and studied.

4.3.2 Magnetic configurations of EML

A set of eight saddle coils placed around the vacuum vessel of TEXT at the radius $r_c = 32.7$ cm creates a stochastic edge layer, coherent magnetic islands, or a mixture of both. The coil bars are closer together on the inside of the torus. This poloidal design will reduce the mode content and cancel out the sideband generation caused by toroidal geometry. A fairly pure poloidal m mode can be obtained. The structure of the EML coil is shown in Fig. 4-10(a). Each coil has fourteen linked current loops with toroidal width 15 cm and is distributed in poloidal direction as

$$\theta_{lj} = \frac{l\pi}{7} + \frac{1}{3}\sin\frac{l\pi}{7} + \theta_{0j}, \quad l = 0, \ldots 13 \tag{4.8}$$

where θ_{0j} is the angle between the feed point of the jth coil and the equatorial plane. The dipole loops, which have opposite current directions for neighboring loops, determine the dominant poloidal mode number m. The toroidal mode number n = 2 or 3, is specified by the relative poloidal rotation of each coil and the electrical polarity of adjacent coils. The m/n = 7/2 mode, which is the one used in this study, has the θ_{0j} as

$$\theta_{0j=1,\ldots 8} = 3^o,\ -9^o,\ 9^o,\ -3^o,\ 3^o,\ -9^o,\ 9^o,\ -3^o \tag{4.9}$$

for the eight coils located at the toroidal positions, Fig. 4-10(b),

$$\phi_{j=1,\ldots 8} = 33.75^o,\ 78.75^o,\ 101.25^o,\ 146.25^o,\ 213.75^o,\ 258.75^o,\ 281.25^o,\ 326.25^o \tag{4.10}$$

and their relative electric polarity (the sign of the coil current)

$$P_{j=1,\ldots 8} = 1,\ 1,\ -1,\ -1,\ 1,\ 1,\ -1,\ -1 \tag{4.11}$$

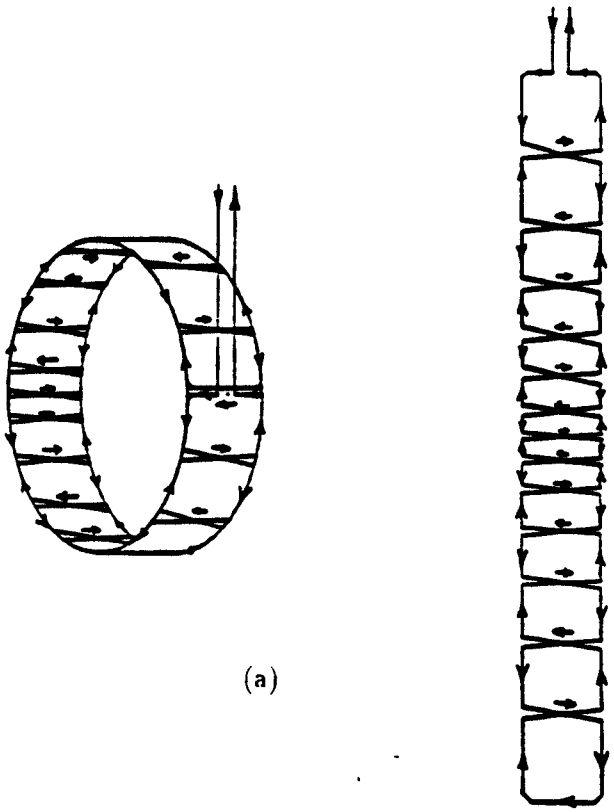

(a)

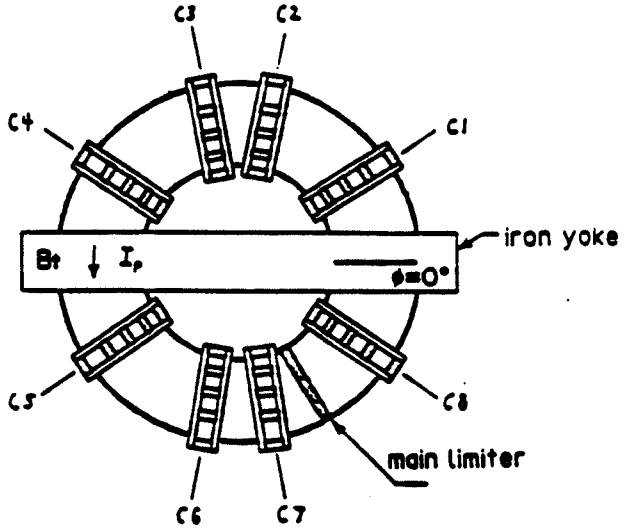

(b)

Figure 4-10: (a) The configuration of the EML coils. (b) Their positions on TEXT.

The magnetic field is calculated using a code with a combination of mapping[87] and field line following[88]. This code separates the toroidal space into two regions, kick and twist. For the kick region, which is under the coil, the perturbation fields (b_r, b_θ) are calculated from the real position and size of each coil current segment. The kick magnitude is obtained from the integration of b_r, b_θ along ϕ-direction. For the twist region, which is between the coils, the field line equations are integrated and the Newton iteration method is used to get the twist magnitude. The tokamak equilibrium fields are approximated by the vacuum poloidal and toroidal components assuming shifted circular cross-sections[89]. The results from running this code, which takes much less computer time, have been confirmed by running a magnetic field line tracing code[90].

The set of helical coils generates the perturbing magnetic field in resonance with the equilibrium magnetic surfaces to produce magnetic islands. When the perturbing field is raised to a certain value, the island chains overlap such that a stochastic layer in the edge is created. Fig. 4-11 shows Poincaré plots of the magnetic field lines in the plane $\phi = 112.5^0$ for four different I_hs (the helical current in EML coils), I_h = 1, 2, 3, and 5 kA. As I_h increases, it shows that the island chains on resonant surfaces begin to form. The island width $\triangle_{mn}$ can be written as[91]

$$\triangle_{mn} = 4\left[\frac{R|\tilde{b}_{mn}(r)|}{mB_t}\left|\frac{q^2}{q'}\right|_{r=r_{mn}}\right]^{1/2} \tag{4.12}$$

where r_{mn} is the radial location of the rational q surface of the mode (m, n). With the neighboring island chains overlapping with each other, the magnetic surfaces become stochastic. A parameter s can be used to define the transition from islands to stochasticity,

$$s = \frac{1}{2}\frac{\triangle_{mn} + \triangle_{m'n'}}{|r_{mn} - r_{m'n'}|} \tag{4.13}$$

where m, n and m', n' represent any two harmonics which have neighboring rational surfaces. If $s \geq 1$, then magnetic surfaces are destroyed in the region between r_{mn} and $r_{m'n'}$, and the field lines become stochastic. The dominant mode,

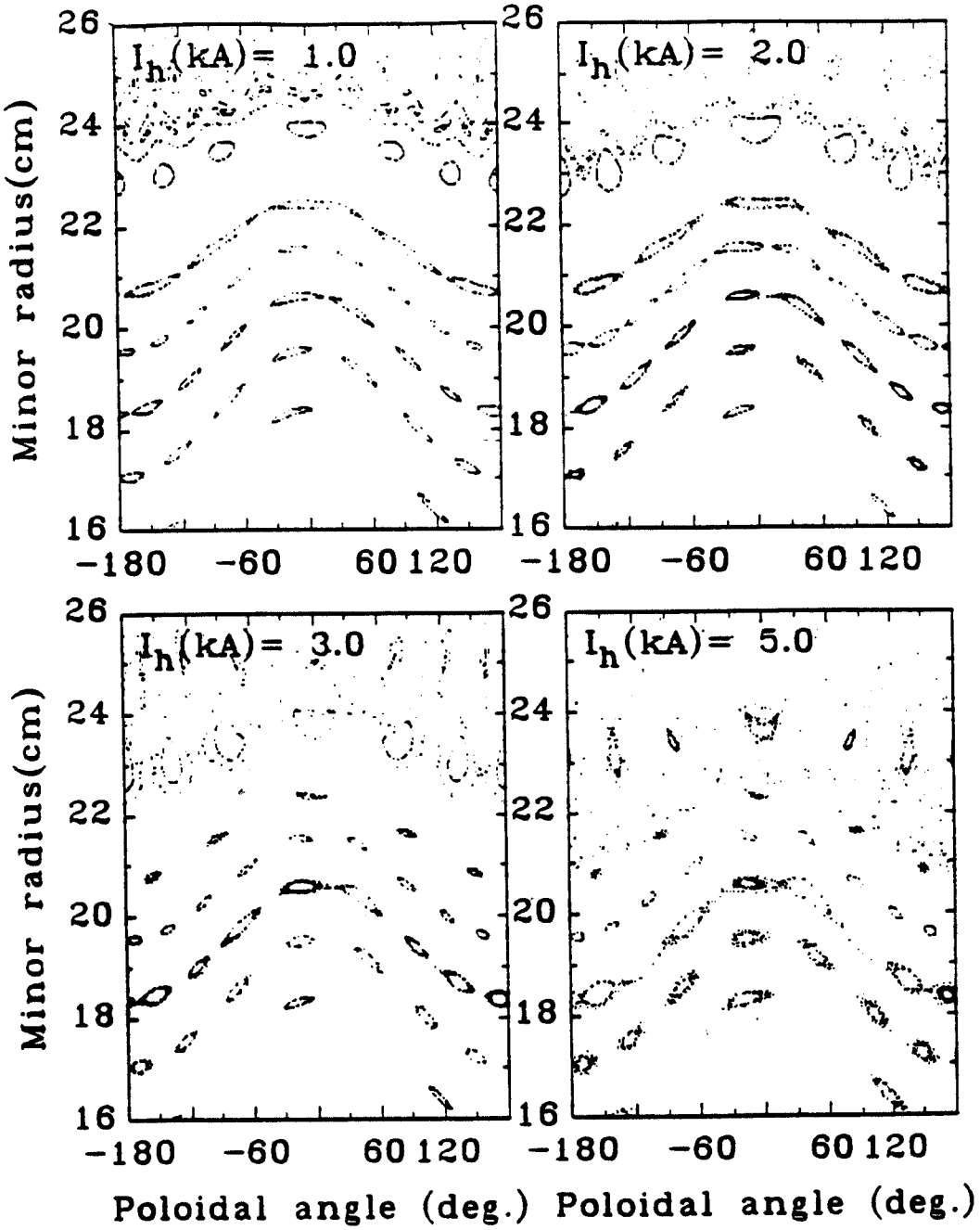

Figure 4-11: Poincaré plot showing the puncture points of magnetic field lines in the plane $\phi = 112.5^0$ for I_h = 1, 2, 3, and 5 kA.

$m/n = 7/2$, of the EML coils is in resonant with the edge surface, $q_a = 3.5$. The edge surfaces become stochastic with increasing I_h. As can be seen in Fig. 4-11, the stochastic layer penetrates deeper into the plasma with higher I_h.

4.3.3 Experimental results

The responses of the hard X-ray signal, normalized to the unperturbed signal (Fig. 4-2), to the magnetic perturbations are shown in Fig. 4-12 for I_h = 1, 2, 3, and 5 kA. The effect of the magnetic perturbation on the hard X-ray signal shows up when I_h is above 2 kA. With higher current, the changes become greater. Typical hard X-ray behavior for I_h = 5 kA is explained here. As I_h is ramping up linearly with time, the generation of magnetic islands or stochasticity is degrading the confinement of runaway electrons in the edge layer. Therefore the runaway electron flux to the limiter increases as is shown by the fast rising signal. The signal peaks at the point when I_h reaches the flat top and decays at a faster rate first, then a slower one during the flat top of I_h. At the end of the pulse, the signal drops and then rises during the longer trailing time of I_h because of the improving confinement as the perturbation field is being removed.

The plasma current in Fig. 4-13 shows little changes caused by the turn on of the I_h. The loop voltage has a little bump at the turn on and a little dip at the turn off of the I_h. The integration of the loop voltage over time, which is proportional to the runaway electron energy, shows a minimum effect on the runaway electrons. However, the plasma potential (ϕ), measured with the HIBP (Heavy Ion Beam Probe), changes with EML current as shown in Fig. 4-14. This change in radial electric field, $E_r = -\partial\phi/\partial r$, would introduce a poloidal drift velocity ($\vec{E} \times \vec{B}$) to the runaway electrons. It is negligibly small compared to the runaway electron poloidal velocity and can be neglected.

Hard X-ray energy spectra with EML are also measured. Fig. 4-15 plots the E_{x0} as a function of time for $t \geq$ 60-70 msec for I_h = 2 and 5 kA. The statistics of data below 60 msec is poor and irrelevant for the study. E_{x0} begins to decrease

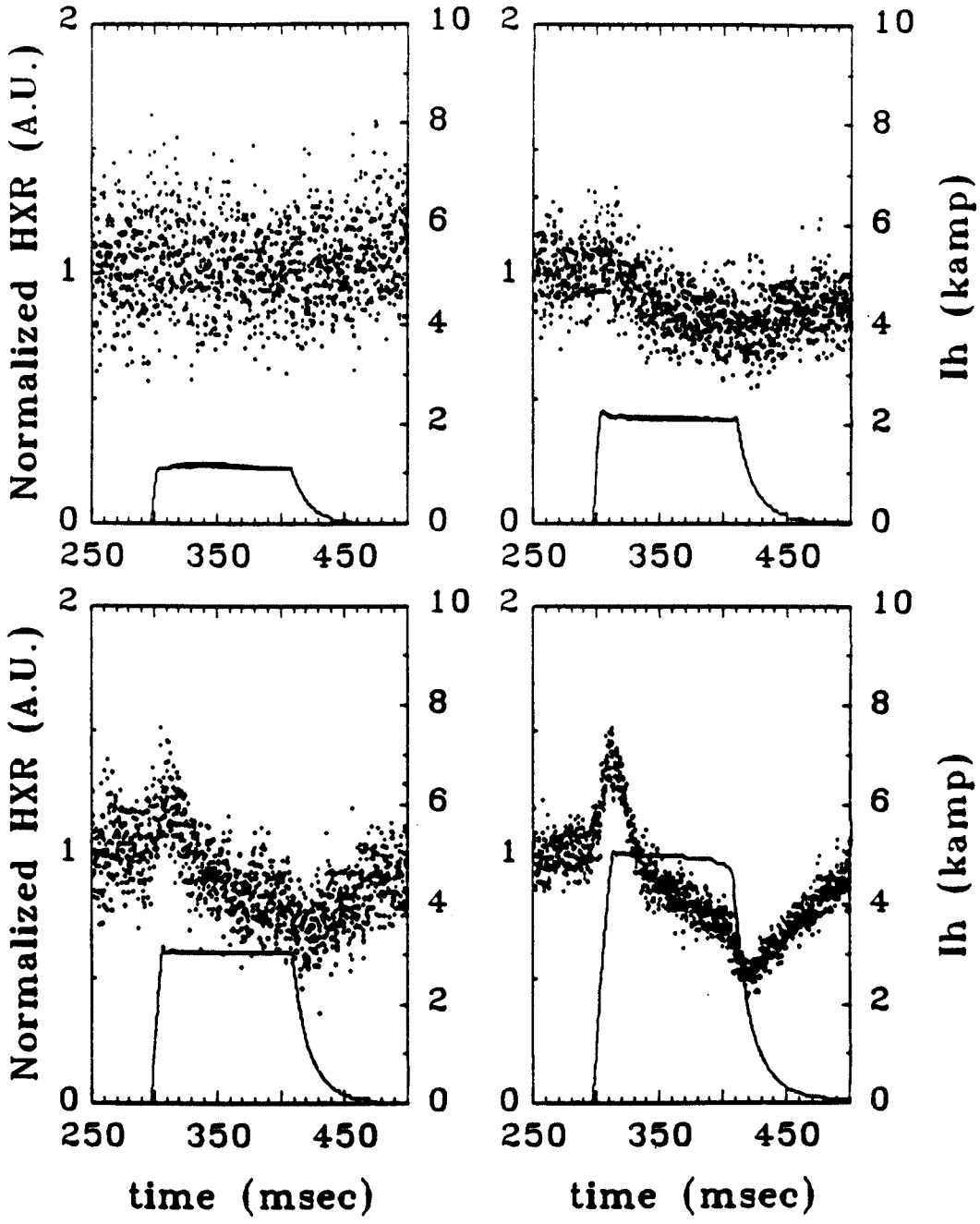

Figure 4-12: Normalized hard X-ray signal and the corresponding helical current I_h as a function of time for I_h = 1, 2, 3, and 5 kA averaged over 5, 6, 6, and 25 shots starting from shot 149237.

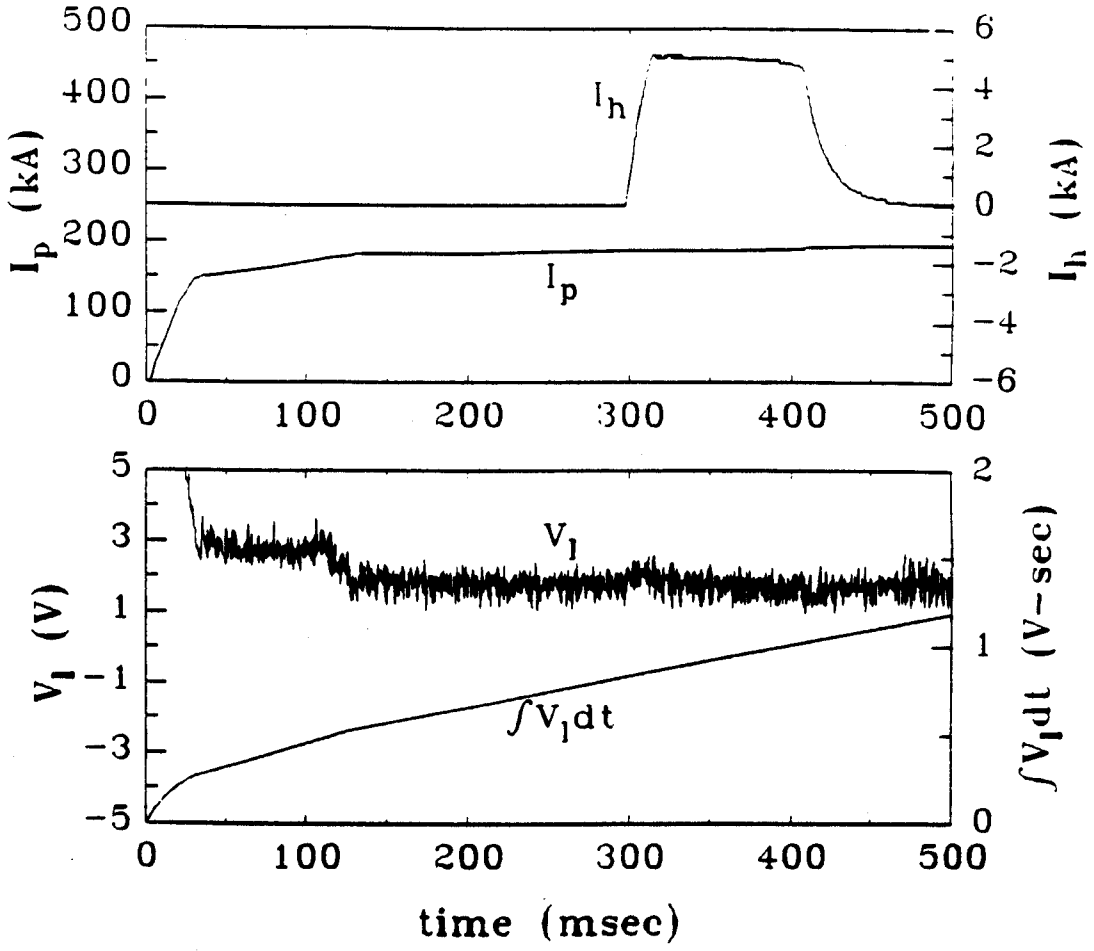

Figure 4-13: Plasma current (I_p), helical current (I_h), loop voltage (V_l), and the integration of V_l for the magnetic perturbation experiment.

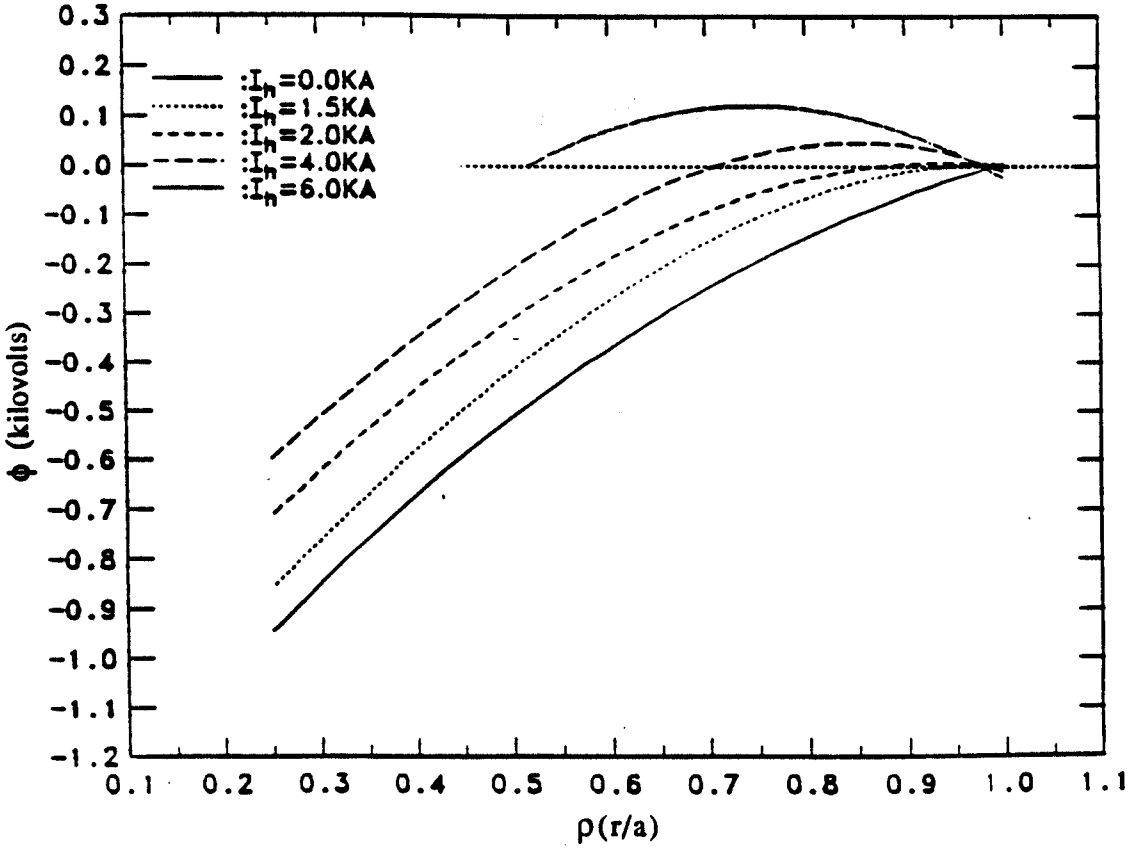

Figure 4-14: The radial dependence of plasma potential, measured with heavy ion beam probe (HIBP), for I_h = 0, 1.5, 2, 4, 6 kA.

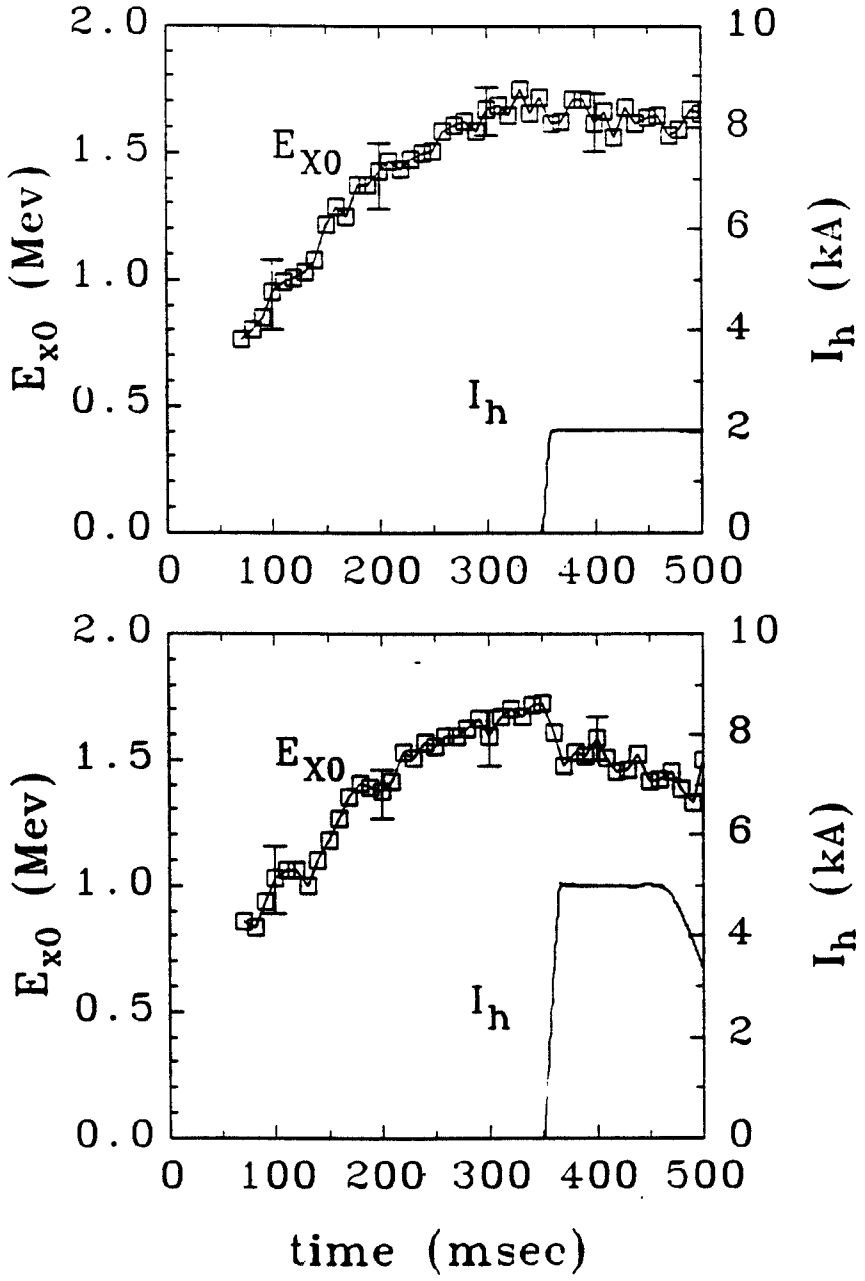

Figure 4-15: The energy index constant E_{x0} as a function of time for I_h = 2 and 5 kA, which is turned on at t = 350 msec.

as the I_h is turned on at t = 350 msec. The amount of decrease is larger for larger current. Chapter 3 describes how to relate the change in E_{x0} to the runaway electron flux to the limiter. An average value of the energy change, $\triangle E_{x0}^{exp}$ is used from Fig. 4-15 and the corresponding change in detector response, $\triangle R^{\triangle E_{x0}^{exp}}$, can be found from Fig 3-7. The change in the runaway electron particle flux to the limiter, $\triangle\Gamma$, is then calculated using Eq. 3.15. Fig. 4-16 shows the results that can be taken to be proportional to the change of the runaway electron particle flux to the limiter for I_h = 5 kA. This result will be used in the next chapter to be compared to the analytical and numerical solutions. Here, only the time period from the turn on till the end of the flat top of I_h is processed. The turn off period is not shown and will not be modelled in the next chapter.

4.4 Magnetic perturbation and position shift experiment

The experiment with both perturbations, magnetic fields and position shift, has also been performed. During the nearly plateau state of the hard X-ray signal, the EML is turned on first and the plasma column is shifted inward when the hard X-ray has relaxed to the slower change rate during the I_h flat top. The hard X-ray signal, I_h, and plasma position are shown in Fig 4-17. Fig. 4-18 shows the drop in the hard X-ray signal caused by the shift of the plasma column with EML in the expanded scale.

The drop is much smaller than that without EML as shown in Fig. 4-7. Because the EML fields affect only the edge layer, they increase the runaway electron edge transport. When the plasma is moved inward, it takes less time for the runaway electrons to reach the limiter with the EML. The response of the hard X-ray signal to the shift is dominated by the diffusion coefficient of the runaway electron at the edge in the short time scale.

Another experiment moves the plasma position first and then turns on the

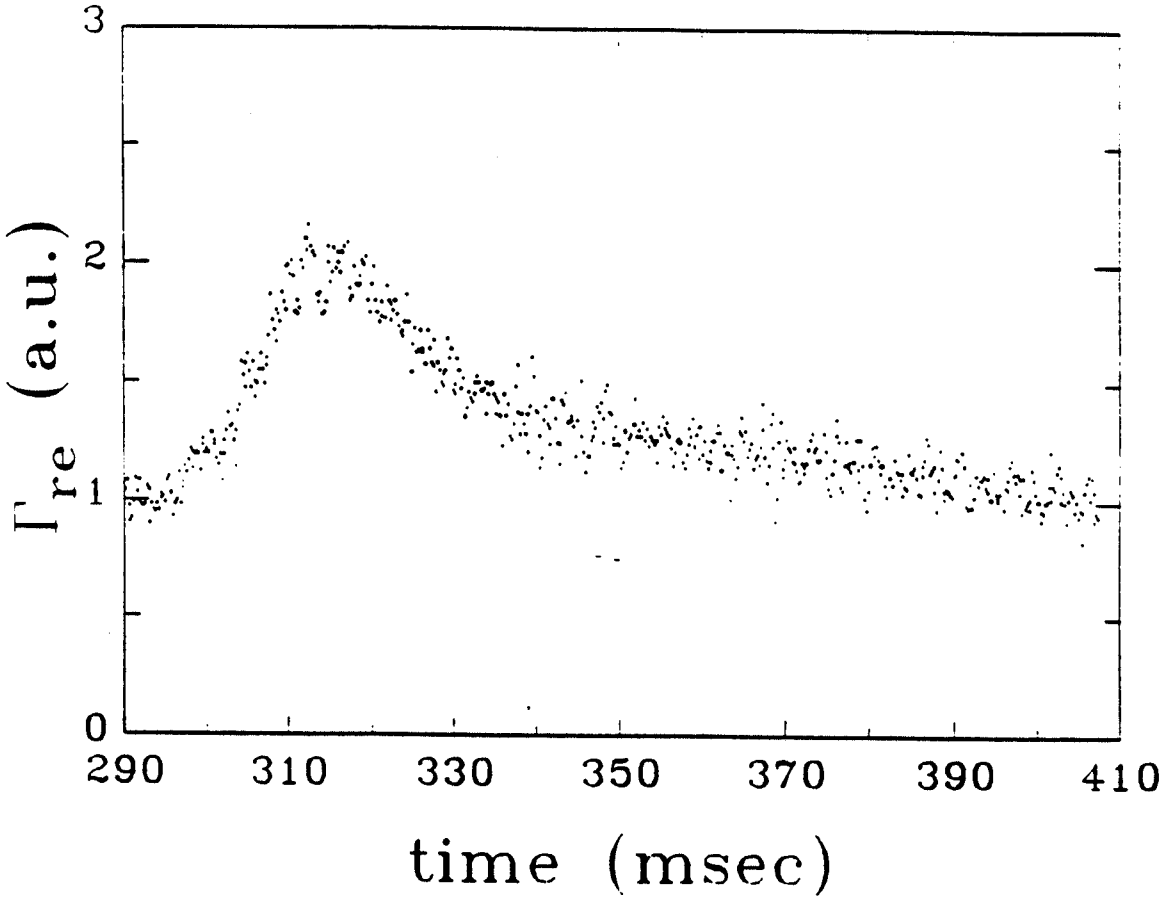

Figure 4-16: The runaway electron particle flux change for I_h = 5 kA for the time period of the turn on and the flat top of the I_h.

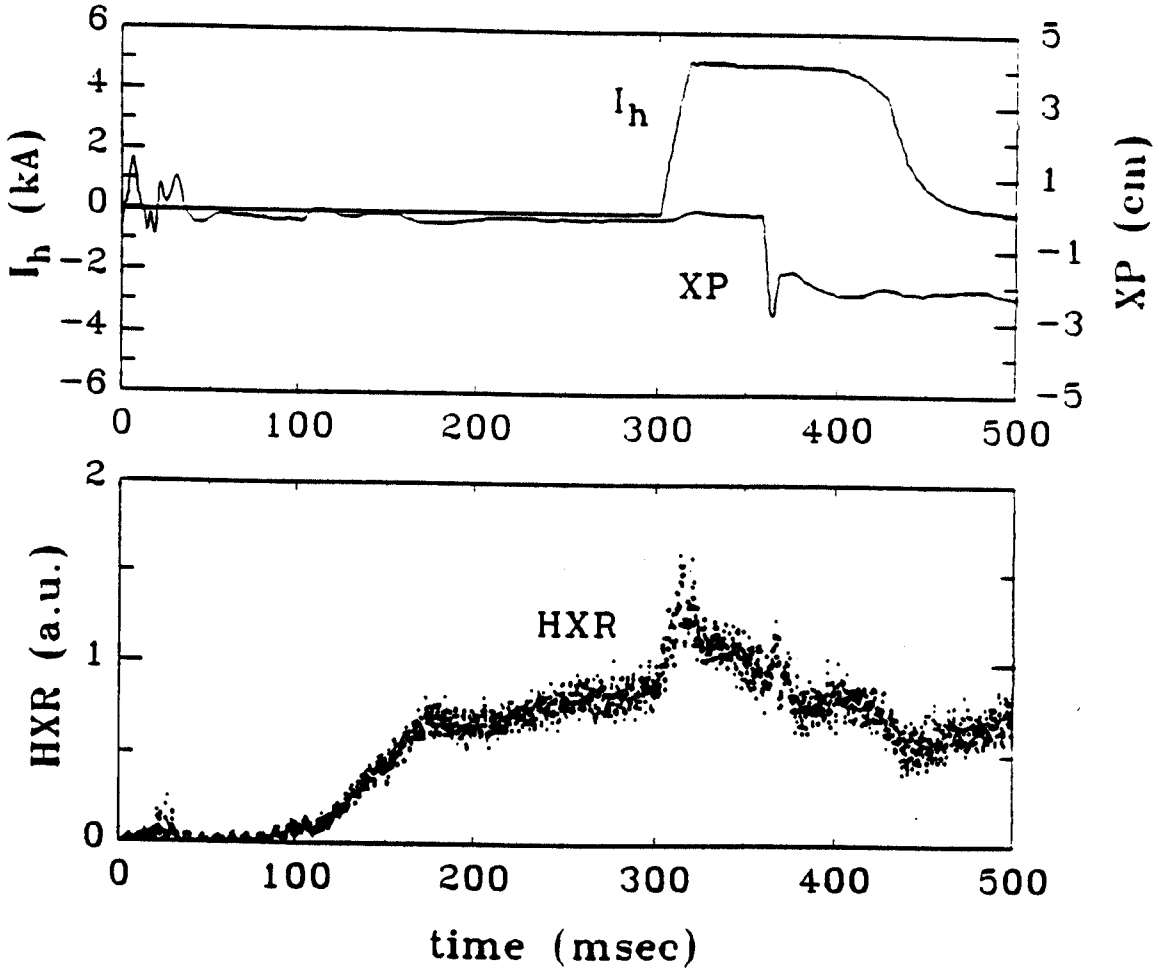

Figure 4-17: Hard X-ray signal (HXR), helical current (I_h), and plasma position (XP) averaged over 22 shots starting from shot 174036 for the experiment with both EML and position shift perturbations.

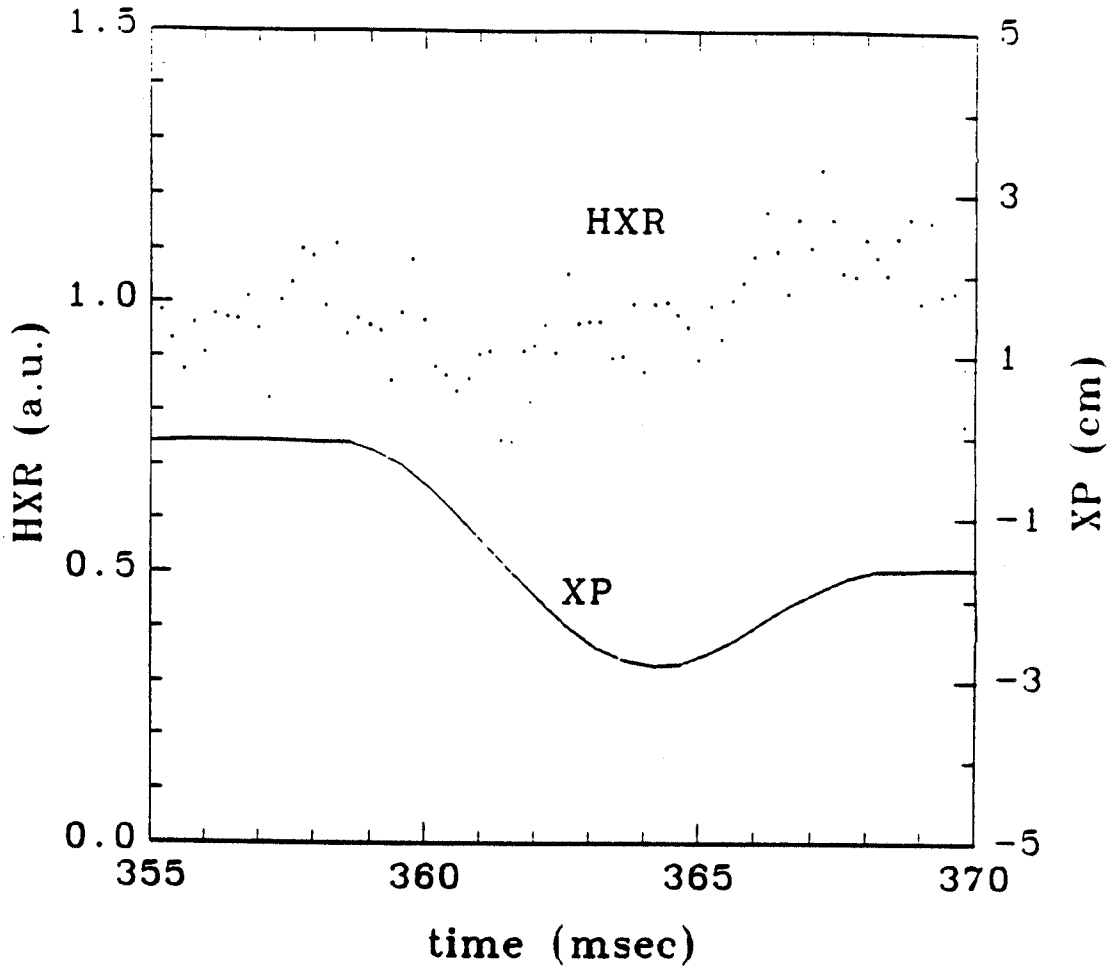

Figure 4-18: The negligible drop in the hard X-ray signal caused by the shift of the plasma column with EML for t = 350 - 370 msec.

EML after the hard X-ray signal has reached the plateau state. Fig. 4-19(Fig. 4-20) shows the plasma position, I_h, and the hard X-ray signal for the 2 cm shift inward(outward) of the plasma column. The interesting observation is that the hard X-ray decay rate during the flat top of I_h is faster for the outward shift than the inward shift. When the plasma is shifted outward(inward), the radius of the confinement is smaller(larger) for the runaway electron drift orbits. With the EML applied, which increases the edge diffusion coefficient, the relaxation rate to the new state with perturbation depends on the size of the confinement. With smaller size, the decay rate is faster. This observation shows that the decay rate of the hard X-ray signal during the flat top of I_h after the faster time modes decay out (the peak) is related to the slower mode decay rate.

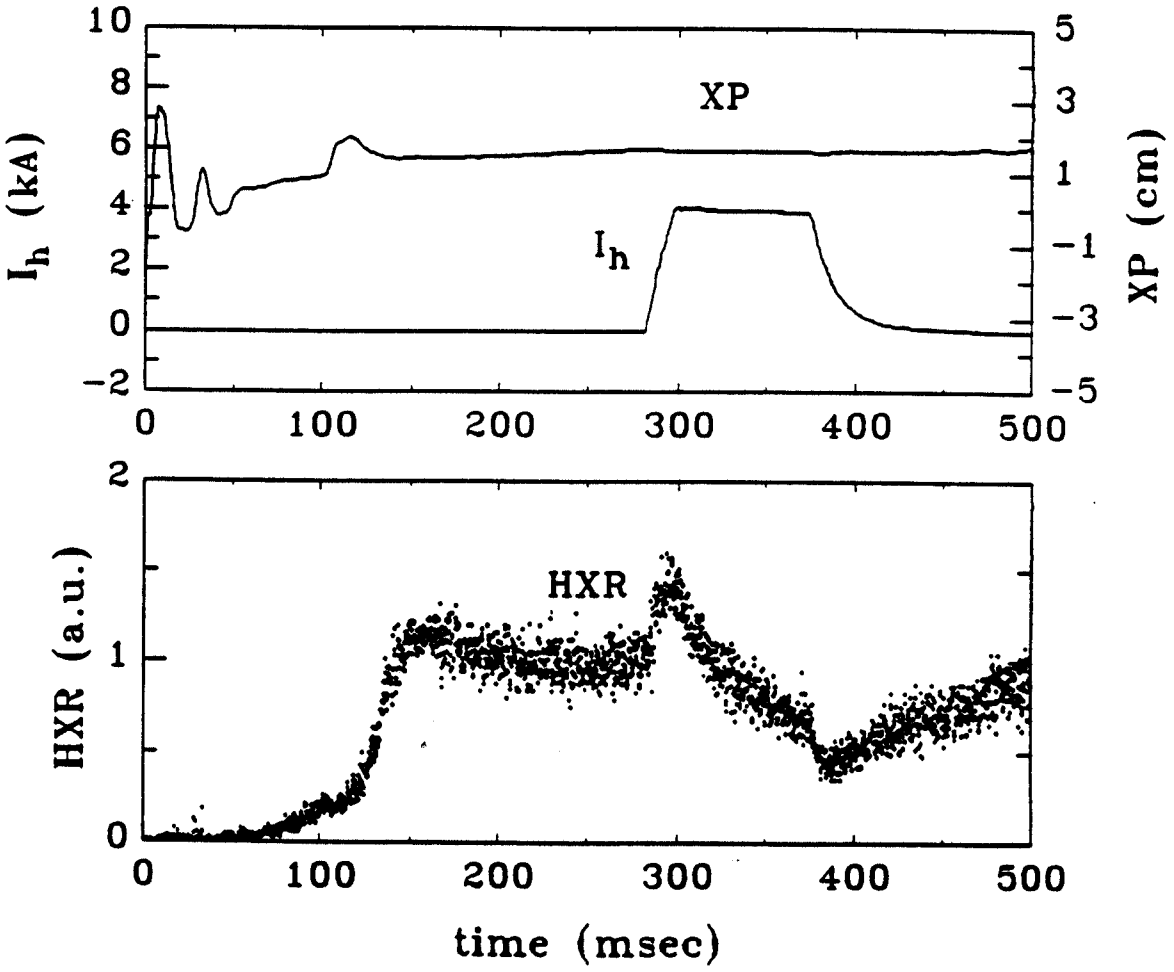

Figure 4-19: The plasma position (XP), I_h, and the hard X-ray signal (HXR) averaged over 11 shots starting from shot 162213.

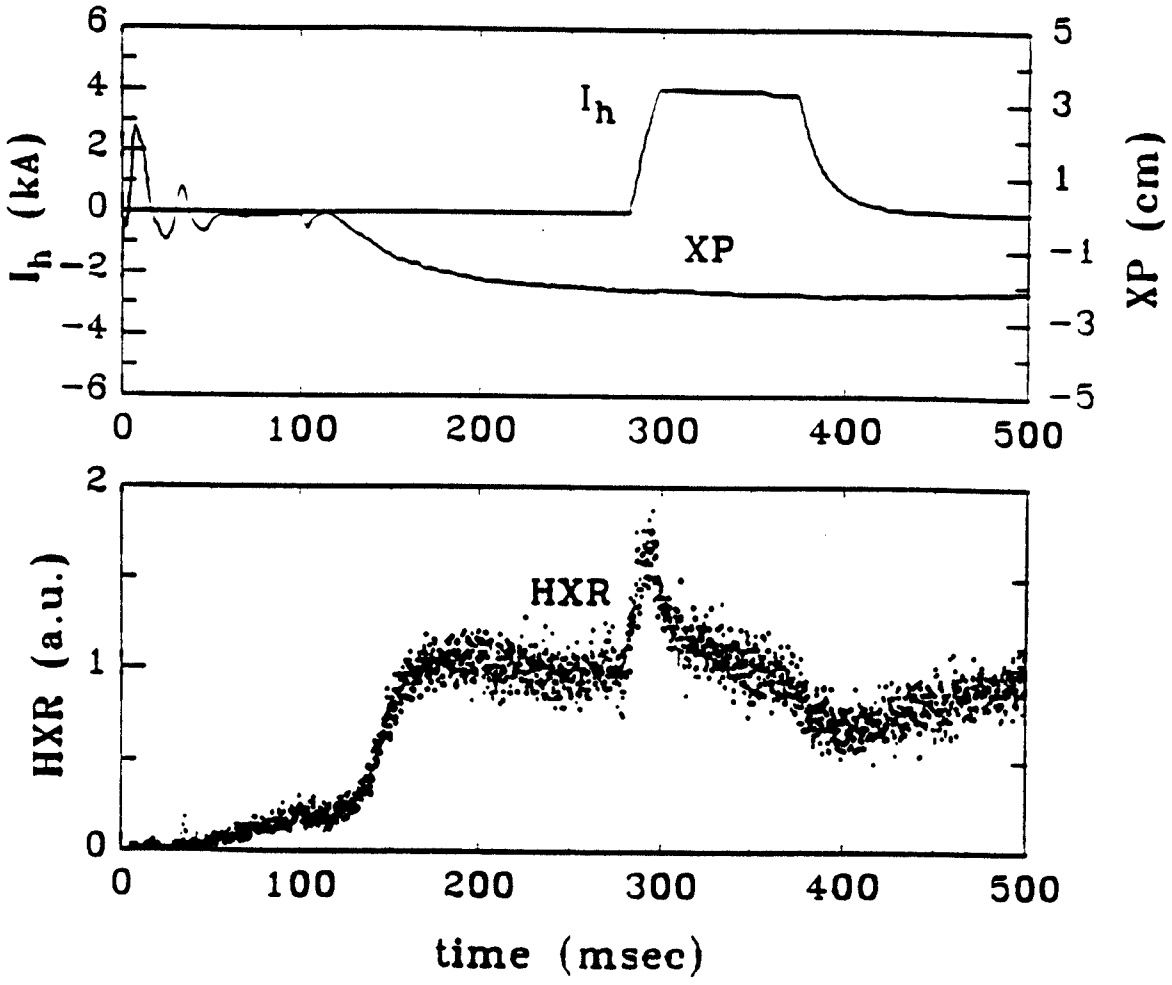

Figure 4-20: The plasma position (XP), I_h, and the hard X-ray signal (HXR) averaged over 10 shots starting from shot 162146.

Chapter 5

Analytical and numerical models

The models to interpret the experimental results are discussed in this chapter. Some approximations are made to get the analytical solutions which can be found in Ref. [92] and will be followed directly. More exact numerical solutions are also obtained and both solutions show good agreement. The runaway electron diffusion coefficient is then estimated by comparing to the experimental results from Chapter 4.

5.1 Diffusion model

A one-dimensional diffusion equation with an anomalous diffusion coefficient D_0 is used. D_0 is assumed to be a constant in time and space. The diffusion model is based on the observations described in Chapter 4. Most of the runaway electrons are created in the early time of the discharge. The production of the runaway electrons during the discharge or caused by the perturbations is small and can be neglected. The source term in the diffusion equation is then neglected. The perturbations are turned on after the hard X-ray signal has reached the state of nearly a plateau. So, by the time the perturbation is turned on, the runaway density is assumed to have relaxed to its lowest eigenmode. The advantage is that the initial density profile in the early discharge need not be known. The

boundary conditions are that the density is flat at the center and disappears at the limiter. The following sections discuss how to model different conditions for different experiments.

5.2 Position shift experiment

5.2.1 Analytical model

The diffusion equation in a slab geometry is written for the runaway electron density N as

$$\frac{\partial N}{\partial t} = \frac{\partial}{\partial x}(D_0 \frac{\partial N}{\partial x}) \tag{5.1}$$

This slab model with x playing the role of the radial variable is adequate because the changes in minor radius with time are small compared to the initial radius a_0. The boundary conditions are

$$N(x = a(t), t) = 0 \tag{5.2}$$

$$\frac{\partial N(x = 0, t)}{\partial x} = 0 \tag{5.3}$$

where $x = 0$ corresponds to $r = 0$ and $x = a(t)$ corresponds to the minor radius of the drift surface of the moving boundary, with $t = 0$ the time at which the plasma begins to move, and a is increasing in size according to

$$a = a(t) = a_0 + \int_0^t dt' V(t') \tag{5.4}$$

The initial condition

$$N(x, t = 0) = \bar{N} \cos(\pi x / 2a_0) \tag{5.5}$$

is employed, the lowest eigenmode, with $\bar{N}$ = constant.

Two cases V = constant with Va_0/D_0 arbitrary and $V = V(t)$ with Va_0/D_0 small are considered and the associated flux $\partial N(x,t)/\partial x|_{x=a}$ is evaluated. In both cases the short time behavior of the flux is dominated by a sum over the rapid exponential decay of the higher eigenmodes as the moving plasma attempts to relax to the lowest moving eigenmode proportional to $\cos[\pi x/2a(t)]$.

V = constant

For the special case of V = constant the flux can be evaluated for arbitrary values of Va_0/D_0. N is written as

$$N = \bar{N} \sum_{n=1}^{\infty} C_n F_n(x,t) \tag{5.6}$$

where $F_n(x,t)$ is the moving boundary eigenfunctions and the coefficients C_n depend only on n.

To find F_n the ansatz

$$F(x,t) = \exp[-\int_0^t d\tau f(x,\tau)] \cos[xk(t)] \tag{5.7}$$

is employed, where the subscript n is dropped temporarily for notational convenience. Taking $\partial F/\partial t$ and $\partial^2 F/\partial x^2$ and plugging into $\partial F/\partial t = D_0 \partial^2 F/\partial x^2$, gives

$$\begin{aligned} & [f - D_0 k^2 - D_0 \textstyle\int_0^t d\tau \frac{\partial^2 f}{\partial x^2} + D_0 (\int_0^t d\tau \frac{\partial f}{\partial x})^2] \cos(xk) \\ = \quad & [-x\tfrac{dk}{dt} - 2D_0 k \textstyle\int_0^t d\tau \frac{\partial f}{\partial x}] \sin(xk) \end{aligned}$$

which must be satisfied for all x and $t > 0$. The functions $f(x,t)$ and $k(t)$ can be chosen to make the coefficients of the $\sin(kx)$ and $\cos(kx)$ terms vanish separately,

$$x\frac{dk}{dt} = -2D_0 k \int_0^t d\tau \frac{\partial f}{\partial x} \tag{5.8}$$

and

$$f = D_0 k^2 + D_0 \int_0^t d\tau \frac{\partial^2 f}{\partial x^2} - D_0 \left(\int_0^t d\tau \frac{\partial f}{\partial x} \right)^2 \tag{5.9}$$

To satisfy Eq. 5.8 requires

$$f(x,t) = h(t) - \frac{x^2}{4D_0} g(t) \tag{5.10}$$

and Eq. 5.8,5.9 become

$$\frac{d}{dt} \ln[k(t)] = \int_0^t d\tau g(\tau) \tag{5.11}$$

$$h(t) - \frac{x^2}{4D_0} g(t) = D_0 k^2(t) - \frac{1}{2} \int_0^t d\tau g(\tau) - \frac{x^2}{4} \left(\int_0^t d\tau g(\tau) \right)^2 \tag{5.12}$$

which must be satisfied for all x. Making the x^0 and x^2 terms balance separately gives

$$h(t) = D_0 k^2(t) - \frac{1}{2}\int_0^t d\tau g(\tau) \tag{5.13}$$

and

$$g(t) = [\int_0^t d\tau g(\tau)]^2 \tag{5.14}$$

Eq. 5.14 is solved by first rewritting it as

$$\frac{d}{dt}[\int_0^t d\tau g(\tau)]^{-1} = -1 \tag{5.15}$$

and then integrating to find

$$\int_0^t d\tau g(\tau) = \frac{-1}{t+\kappa} \tag{5.16}$$

and

$$g(t) = \frac{1}{(t+\kappa)^2} \tag{5.17}$$

with κ a constant. Next, solving Eq. 5.11 for $k(t)$ using

$$\frac{d}{dt}\ln[k(t)] = \int_0^t d\tau g(\tau) = \frac{-1}{t+\kappa} = -\frac{d}{dt}\ln(t+\kappa) \tag{5.18}$$

gives

$$k(t) = \frac{p}{t+\kappa} \tag{5.19}$$

with p another constant. The final free function $h(t)$ is then found from Eq. 5.13 to be

$$h(t) = \frac{D_0 p}{(t+\kappa)^2} + \frac{1}{2(t+\kappa)} \tag{5.20}$$

Using Eq. 5.10, $\int_0^t d\tau f(x,\tau)$ gives

$$\begin{aligned}\int_0^t d\tau f(x,\tau) &= \int_0^t d\tau h(\tau) - \frac{4x^2}{D_0}\int_0^t d\tau g(\tau) \\ &\quad \frac{-D_0 p^2 t}{\kappa(t+\kappa)} - \frac{1}{2}\ln(\frac{t+\kappa}{\kappa}) + \frac{x^2}{4D_0(t+\kappa)}\end{aligned}$$

so that the form of $F(x,t)$ can be found as

$$F(x,t) = (\frac{\kappa}{\kappa+t})^{1/2}\exp[-\frac{D_0 p^2 t}{\kappa(\kappa+t)} - \frac{x^2}{4D_0(\kappa+t)}]\cos(\frac{px}{\kappa+t}) \tag{5.21}$$

To satisfy $F(x=a,t)=0$ with

$$a = a_0 + Vt \tag{5.22}$$

requires

$$\frac{p(a_0+Vt)}{\kappa+t} = \pi(n-\frac{1}{2}),\ n=1,2,\cdots$$

or

$$p = \pi(n-\frac{1}{2})/V \text{ and } \kappa = a_0/V$$

Plugging p and κ into Eq. 5.21, the moving V boundary eigenfunctions become

$$F_n(x,t) = (\frac{a_0}{a})^{1/2}\exp[-\frac{\pi^2(n-\frac{1}{2})^2 D_0 t}{a_0 a} - \frac{Vx^2}{4D_0 a}]\cos[\frac{\pi(n-\frac{1}{2})x}{a_0}] \tag{5.23}$$

The initial condition Eq. 5.5 is used to find

$$\exp(\frac{Vx^2}{4D_0 a_0})\cos(\frac{\pi x}{2a_0}) = \sum_{n=1}^{\infty} C_n \cos[\frac{\pi(n-\frac{1}{2})x}{a_0}] \tag{5.24}$$

Since the $\cos[\pi(n-\frac{1}{2})x/a_0]$ form a complete, orthogonal set, the C_n are found to be

$$C_n = \frac{1}{\pi}\int_0^{\pi} dy \exp(\frac{1}{2}\alpha y^2)\{\cos(ny) + \cos[(n-1)y]\} \tag{5.25}$$

where $y = \pi x/a_0$ and

$$\alpha \equiv \frac{Va_0}{2\pi^2 D_0} \tag{5.26}$$

The flux at $x = a = a_0 + Vt$ from Eqs. 5.6 and 5.23 can be written as

$$\frac{\partial N(x,t)}{\partial x}|_{x=a} = -\frac{\pi a_0^{1/2}\bar{N}}{a^{3/2}}\exp(-\frac{Va}{4D_0})\sum_{n=1}^{\infty}(-1)^{n+1}(n-\frac{1}{2})C_n \exp[-\frac{\pi^2(n-\frac{1}{2})^2 D_0 t}{a_0 a}] \tag{5.27}$$

Using the x derivative of Eq. 5.24 evaluated at a_0

$$\sum_{n=1}^{\infty}(-1)^{n+1}(n-\frac{1}{2})C_n = \frac{1}{2}\exp(\frac{Va_0}{4D_0})$$

and subtracting and adding unity to the exponential under the sum for evaluating the short time behavior of the flux, Eq. 5.27 becomes

$$\frac{\partial N(x,t)}{\partial x}|_{x=a} = -\frac{\pi a_0^{1/2}\bar{N}}{2a^{3/2}}[\exp(-\frac{V^2 t}{4D_0}) - 2\exp(-\frac{Va}{4D_0})\sum(t)] \tag{5.28}$$

where

$$\sum(t) = \sum_{n=1}^{\infty}(-1)^{n+1}(n-\frac{1}{2})C_n\{1-\exp[-\frac{\pi^2(n-\frac{1}{2})^2 D_0 t}{a_0 a}]\} \tag{5.29}$$

Two limits of C_n are of particular interest and can be obtained by integrating by parts. The first and more interesting case is for $n \neq 1$, $n^2 \gg \alpha$, and $n^2 \gg \alpha^2$, and yields

$$C_n = \frac{(-1)^{n+1} V a_0 (n-\frac{1}{2}) \exp(\frac{V a_0}{4D_0})}{\pi^2 D_0 n^2 (n-1)^2}[1 - \frac{2\pi^2\alpha^2 + 6\alpha}{n^2} + \cdots] \tag{5.30}$$

The second is for $\pi\alpha \gg n$ and to leading order is found to give

$$C_n = \frac{(-1)^{n+1} 16\pi^2 D_0^3 (n-\frac{1}{2})}{V^3 a_0^3} \exp(\frac{V a_0}{4D_0}) + \cdots$$

which is valid even for $n = 1$.

For $n^2 \gg \alpha^2$, α expansion may be employed to perform the sum of Eq. 5.29 to a good approximation as long as the result is insensitive to the n for which Eq. 5.30 fails, namely $n = 1$ and $n \sim \pi\alpha$. For this to be the case, the exponential in Eq. 5.29 must be less than unity for these n giving

$$\frac{\pi^2 D_0 t}{4 a_0 a} \ll 1 \quad \text{and} \quad \frac{a_0 V^2 t}{4 a D_0} \ll 1 \tag{5.31}$$

The product of these inequalities gives $(Vt/a)^2 \ll 1$, thereby justifying the slab model. With these restrictions, the sum can be replaced by an integral which is insensitive to the lower limit so that Eq. 5.29 may be approximated by[93]

$$\begin{aligned} \sum(t) &\approx [\frac{V a_0 \exp(\frac{V a_0}{4D_0})}{\pi^2 D_0}][\frac{\pi (D_0 t)^{1/2}}{(a_0 a)^{1/2}}] \int_0^{\infty} \frac{d\xi}{\xi^2}[1 - \exp(-\xi^2)] \\ &\approx \frac{V t^{1/2} \exp(\frac{V a_0}{4D_0})}{(\pi D_0)^{1/2}} \end{aligned} \tag{5.32}$$

where $\sum_n = \int dn$ is employed and $\xi = \pi(D_0 t)^{1/2}(n - \frac{1}{2})/a_0 a$.

Using the short time approximation of Eq. 5.32 in Eq. 5.28 yields the short time behavior of the runaway electron flux,namely,

$$\frac{\partial N(x,t)}{\partial x}|_{x=a} \approx -(\frac{\pi \bar{N}}{2a_0})[1 - 2V(\frac{t}{\pi D_0})^{1/2} + \cdots] \tag{5.33}$$

provided the conditions of Eqs. 5.31 are satisfied (which ensure that the response to the shift is small compared to unity).

To compare with the experimental results it is convenient to normalize $\partial N/\partial x|_{x=a}$ to the flux at $t = 0$, $-\pi\bar{N}/2a_0$, to obtain the normalized flux I_s, which to lowest significant order is

$$I_s \approx 1 - 2V(\frac{t}{\pi D_0})^{1/2} \tag{5.34}$$

The decrease in I_s, $2V(t/\pi D_0)^{1/2}$, can then be compared to the decrease in the normalized hard X-ray signal at its recovery time for a known shift speed. From Fig. 4-7 the decrease in the normalized signal is ≈ 0.3 and the time it takes for the signal to begin to recover is ≈ 7 msec. Using an average speed over the 7 msec of ≈ 450 cm/sec from Fig. 4-7 then gives

$$D_0 \approx 2 \times 10^4 \quad \text{cm}^2/\text{sec} \tag{5.35}$$

Using the preceding numbers and $a_0 = 26$ cm, $\pi\alpha = Va_0/2\pi D_0$ is found to be small and the second inequality of Eq. 5.31 well satisfied, but the first is only marginally satisfied since $\pi^2 D_0 t/4a_0^2 \approx 1/2$ at $t = 7$ msec. Consequently, the preceding value of D_0 should be viewed as being valid to within factors of two or so.

Small Va_0/D_0 for general V(t)

The hard X-ray signal begins to recover slightly before the plasma has stopped increasing in size. To understand this behavior a more general $V = V(t)$ must be considered. By exploiting the smallness of Va_0/D_0 noted earlier, Eq. 5.1 will next be solved for a general time dependent increase in minor radius.

To obtain the small Va_0/D_0 solution to Eq. 5.1 for $V = V(t)$ it is convenient to change variables from (x,t) to (z,τ) where z and τ are defined by

$$\begin{aligned} z &= \frac{\pi x}{2a} \\ \tau &= \frac{\pi^2}{4}\int_0^t \frac{dt' D_0(t')}{[a(t')]^2} \end{aligned}$$

with $a = a(t)$. Notice that $D_0 = D_0(t)$ is allowed by the procedure being employed. In the new variables Eq. 5.1 becomes

$$\frac{\partial N}{\partial \tau} - \frac{\partial^2 N}{\partial z^2} = h(\tau) z \frac{\partial N}{\partial z} \tag{5.36}$$

with

$$h(\tau) = \frac{4aV}{\pi^2 D_0} = \frac{2}{\pi^2 D_0}\frac{da^2}{dt} = \frac{d}{d\tau}\ln a \tag{5.37}$$

Expanding N in powers of h as $N = N_0 + N_1 + \cdots$, Eq. 5.36 gives to lowest order

$$\frac{\partial N_0}{\partial \tau} - \frac{\partial^2 N_0}{\partial z^2} = 0 \tag{5.38}$$

and to next order

$$\frac{\partial N_1}{\partial \tau} - \frac{\partial^2 N_1}{\partial z^2} = h(\tau) z \frac{\partial N_0}{\partial z} \tag{5.39}$$

The solution to Eq. 5.38 must be independent of V and satisfy the initial condition of Eq. 5.5. Therefore N_0 must be taken to be

$$N_0 = \bar{N} \exp(-\tau)\cos(z) \tag{5.40}$$

To next order the equation

$$\frac{\partial N_1}{\partial \tau} - \frac{\partial^2 N_1}{\partial z^2} = -\bar{N} h(\tau) \exp(-\tau) z \sin(z) \tag{5.41}$$

must be solved subject to the initial and boundary conditions

$$N_1(z, \tau = 0) = 0 \tag{5.42}$$

$$\frac{\partial N_1(z,\tau)}{\partial z}|_{z=0} = 0 \tag{5.43}$$

$$\text{and } N_1(z = \frac{\pi}{2}, \tau) = 0 \tag{5.44}$$

Substituting

$$N_1 = \bar{N} \sum_{n=0}^{\infty} A_n(\tau) \cos[(2n+1)z] \tag{5.45}$$

into Eq. 5.41 and using the completeness and orthogonality of the eigenfunctions gives

$$\frac{dA_n}{d\tau} + (2n+1)^2 A_n = -\frac{4}{\pi} h(\tau) \exp(-\tau) \int_0^{\frac{\pi}{2}} dz z \sin(z) \cos[(2n+1)z] \tag{5.46}$$

Carrying out the z integrations and solving for A_n yields

$$A_n(\tau) = -\frac{1}{2}B_n \exp[-(2n+1)^2\tau] \int_0^\tau d\tau' h(\tau') \exp[(2n+1)^2\tau' - \tau'] \qquad (5.47)$$

where $B_0 = 1$ and for $n \geq 1$

$$B_n = \frac{(-1)^n(2n+1)}{n(n+1)} \qquad (5.48)$$

Using the preceding to form the flux and extracting the $n = 0$ term results in the expression

$$\begin{aligned} \frac{\partial N}{\partial z}|_{z=\pi/2} \approx \frac{\partial(N_0+N_1)}{\partial z}|_{z=\pi/2} &= -\exp(-\tau)[1 - \frac{1}{2}\int_0^\tau d\tau' h(\tau')] \\ &+2\sum_{n=1}^{\infty} \frac{(n+\frac{1}{2})^2}{n(n+1)} \int_0^\tau d\tau' h(\tau') \exp[-(2n+1)^2(\tau-\tau') - \tau'] \end{aligned} \qquad (5.49)$$

The $\tau \ll 1$ behavior is then found by replacing the sum by an integral to find

$$\frac{\partial N}{\partial z}|_{z=\pi/2} \approx -[1 - \frac{1}{2}\int_0^\tau d\tau' h(\tau')] + \frac{1}{2}\pi^{1/2} \int_0^\tau \frac{d\tau' h(\tau')}{(\tau-\tau')^{1/2}} \qquad (5.50)$$

where

$$\int_0^\tau d\tau' h(\tau') = \ln(a/a_0) \approx \frac{1}{a_0}\int_0^\tau d\tau' V(\tau')$$

is negligible compared to the last term for $\tau \ll 1$. For V a constant the last term in Eq. 5.50 can be integrated by parts using $(d/d\tau')(\tau-\tau')^{1/2} = -\frac{1}{2}(\tau-\tau')^{-1/2}$ to recover the result of the preceding subsection.

Normalizing Eq. 5.50 to the flux at $t = 0$ to obtain the normalized flux I_s and keeping only the lowest significant order terms gives

$$I_s \approx 1 - \frac{1}{2}\pi^{1/2} \int_0^\tau \frac{d\tau' V(\tau')}{(\tau-\tau')^{1/2}} \approx 1 - \frac{1}{(\pi D_0)^{1/2}} \int_0^t \frac{dt' V(t')}{(t-t')^{1/2}} \qquad (5.51)$$

where in the last form $D_0 =$ constant is employed as well as $a \approx a_0$.

Eq. 5.51 can be used to see that the minimum in the flux I_s will typically occur midway between the first maximum and the first zero of $V(t)$; in agreement with the experimental observation that the hard X-ray signal normally begins to recover prior to the plasma reaching the maximum minor radius. Taking $V(t)$ to be of the form

$$V(t) = V_0[1 - (t-t_0)^2/t_0^2] \qquad (5.52)$$

where $2t_0$ is the time of the first zero of $V(t)$ and t_0 the time of the maximum V_0, then Eq. 5.51 gives

$$I_s = 1 - \frac{8V_0 t^{3/2}(5t_0 - 2t)}{15(\pi D_0)^{1/2} t_0^2} \tag{5.53}$$

The preceding model makes physical sense only as long as I_s remains reasonably close to unity so that the perturbation expansion technique is valid.

The flux begins to recover when $\partial I_s/\partial t = 0$ at $t = 3t_0/2$, mid-way between the maximum in $V(t)$ and $a(t)$, and returns to unity at $t = 5t_0/2$. At the recovery time $\tau_r \equiv 3t_0/2$, Eq. 5.53 becomes

$$I_s(t = \tau_r) = 1 - \frac{8V_0}{5}(\frac{\tau_r}{\pi D_0})^{1/2} = 1 - \frac{32\bar{V}}{15}(\frac{\tau_r}{\pi D_0})^{1/2} \tag{5.54}$$

where $\bar{V} = 3V_0/4$ is the average value of $V(t)$ over the interval from $t = 0$ to $t = \tau_r$. Therefore, Eq. 5.54 is in good agreement with the constant V estimate of Eq. 5.34 at $t = \tau_r$ for $V \approx \bar{V}$ and in Eq. 5.53 is in excellent agreement with the early time behavior of hard X-ray in Fig. 4-7.

5.2.2 Numerical model

A one-dimensional diffusion equation in cylindrical coordinates is written for the local density $N(r,t)$ of runaway electrons,

$$\frac{\partial N}{\partial t} = -\frac{\partial}{r\partial r}(r\Gamma) \tag{5.55}$$

where

$$\Gamma = -D_0 \frac{\partial N}{\partial r} \tag{5.56}$$

is the runaway electron particle flux and D_0 is the diffusion coefficient.

The initial condition in the cylindrical coordinates is written as

$$N(r, t = 0) = \bar{N} J_0(\gamma_1 r/a_0) \tag{5.57}$$

where J_0 is the Bessel function, γ_1 is the first zero of J_0, and $\bar{N}$ is a constant. The same boundary conditions are used as discussed in preceding subsection. The

density is flat at the center

$$\frac{\partial N(r=0,t)}{\partial r} = 0 \tag{5.58}$$

and vanishes at the limiter

$$N(r=a(t),t) = 0 \tag{5.59}$$

The moving boundary position $a(t)$ is found from experimentally measured plasma position $\triangle X(t)$

$$a(t) = a_0 - \triangle X(t) \tag{5.60}$$

where $\triangle X(t)$ is negative as shown in Fig. 4-7.

A change of variable is performed using $s \equiv r/a(t)$ and Eq. 5.55 becomes

$$\frac{\partial N}{\partial t} = \frac{1}{a^2(t)s}\frac{\partial}{\partial s}(sD_0\frac{\partial N}{\partial s}) - \frac{s}{a(t)}\frac{da(t)}{dt}\frac{\partial N}{\partial s} \tag{5.61}$$

subject to the boundary conditions

$$\frac{\partial N(s=0,t)}{\partial s} = 0 \tag{5.62}$$

$$N(s=1,t) = 0 \tag{5.63}$$

and the initial condition

$$N(s,t=0) = \bar{N}J_0(\gamma s) \tag{5.64}$$

Eq. 5.61 is solved numerically by using a standard PDE solver[94]. The routine approximates the partial differential equation by a system of ordinary differential equations, obtained by replacing the space derivatives by finite differences. This system is then integrated forward in time using Gear's method. The approximation uses a uniform mesh in the space direction; in the time direction the interval is chosen by the routine to maintain the local accuracy specified. The initial values and two boundary conditions must be given. The accuracy for controlling the local error estimate in the time integration is given and controlled by the routine, but not the accuracy of the approximation in space. The accuracy is tested by using two different mesh sizes to check that numerical error is not influencing the results. The code was run on a Cray computer. The flux at the edge $\Gamma = -D_0\partial N/\partial r|_{r=a}$

is calculated and normalized to the axisymmetric case. Results show that the best fit to the experimental result, the solid curve in Fig. 5-1, is with the diffusion coefficient

$$D_0 = 1.5 \times 10^4 \quad \mathrm{cm}^2/\mathrm{sec}. \tag{5.65}$$

and is accurate to within 20%.

5.2.3 Discussion of the results

Zweben, Swain and Fleischmann[40] performed the same experiment on ORMAK. The model diffusion equation solved here is similar except that a moving boundary is used instead of an inward convective velocity added in the diffusion equation by them to simulate the plasma shift motion. Also, the initial condition is different. They assumed a steady state had been reached and we assumed the density profile has relaxed to the lowest eigenmode by the time the shift is turned on. In addition, the equation is solved in the laboratory frame rather than the moving frame because the boundary condition at the magnetic axis is easier to apply.

The numerical result fits the experiment reasonably well considering there is only one free parameter, D_0, to be adjusted. There is an about 1 msec delay after the minimum, Fig. 5-1. The experimental result is averaged over several shots. The position change is not exactly the same for each shot and the average is used in the numerical model. Considering this and other experimental errors, the estimate of D by the numerical model is valid with factors of two or so.

The analytical and numerical models discussed show with good agreement that the diffusion coefficient estimated is $D_0 \sim 1 \times 10^4$ cm^2/sec. However the diffusion coefficient is unlikely to be a constant across the minor radius, as the model assumes. Measurements of the background electron thermal conductivity χ_e in TEXT find it to be much larger at the edge than the center[84]. If the actual runaway diffusion coefficient has a similar radial dependence then the plasma shift experiments provide a measure of D_0 near the edge, $a_0 < r < a(t)$, rather than

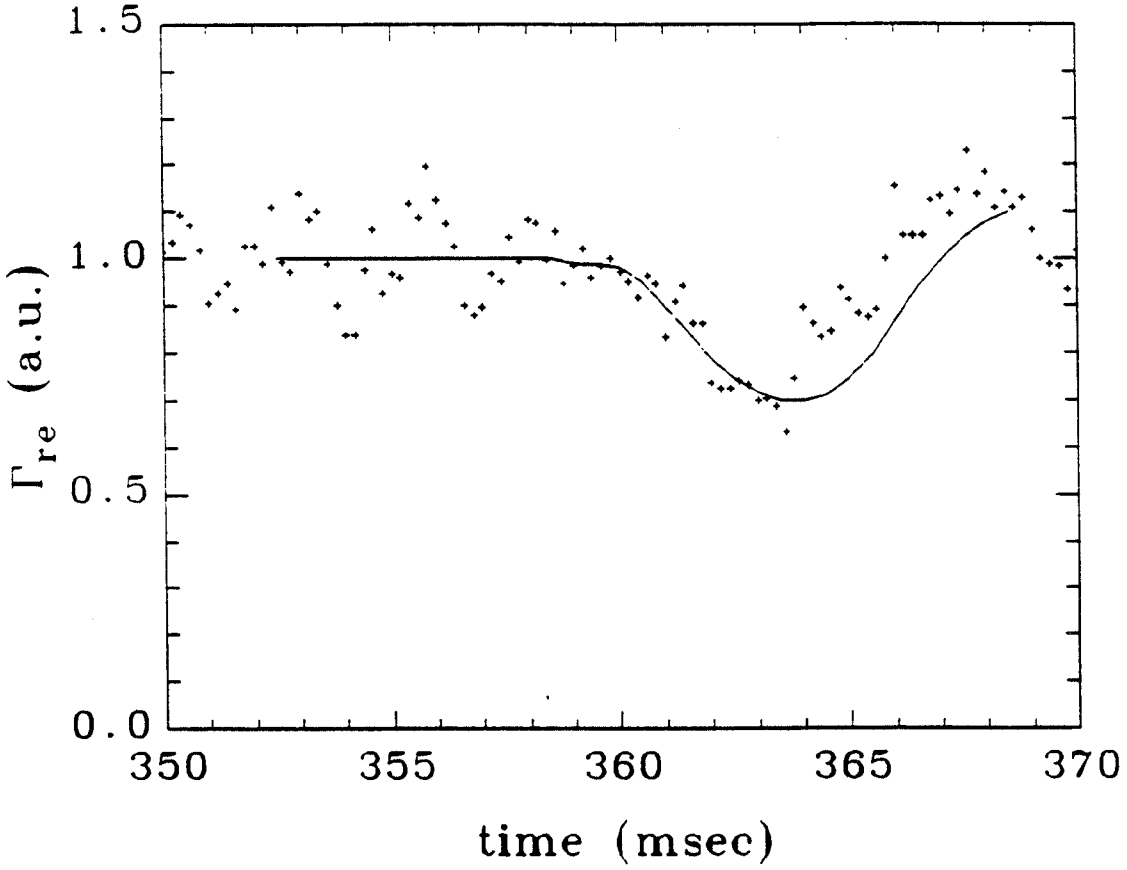

Figure 5-1: Numerical result, the solid curve, for position shift experiment with $D_0 = 1.5 \times 10^4$ cm^2/sec.

in the core, since the short time evolution of a plasma slightly increased in size would be expected to be dominated by the local value of D_0. Also as discussed in Sec. 5.2, the D_0 deduced from the position shift experiment is the edge value. The next section will discuss an independent measure of D_0 which provides the information of D_0 further in the plasma.

5.3 Magnetic perturbation experiment

5.3.1 Analytic model

A layer of stochastic magnetic field in the edge region is generated by the externally applied perturbation field. The diffusion coefficient in the layer, D_s, is assumed to be very large based on the concept that the parallel transport along the magnetic field lines is responsible for the runaway electron loss in the layer[55]. The diffusion equation, Eq. 5.55, is used with the boundary condition on axis, Eq. 5.58, and the initial condition, Eq. 5.57. The remaining boundary condition for $t \geq 0$ now is

$$N(r = b, t \geq 0) = 0 \tag{5.66}$$

where $b = a_0 - d_s$, and d_s is the width of the stochastic layer in the edge region.

At turn on, neglecting the finite ramp up time of the EML current, the layer d_s is assumed to become fully stochastic with $D_s \rightarrow \infty$. Runaway electrons are instantaneously depleted, thereby giving a $\delta(t)$ function in the flux. Moreover, at turn on, the lowest eigenfunction of the larger system, $J_0(\gamma_1 r/a_0)$, begins to readjust and relax toward the lowest eigenfunction of the smaller system, $J_0(\gamma_1 r/b)$. The step in the density profile at $r = b$ is removed diffusively at $t = 0$, giving an additional infinite, but integrable, flux which decays away.

The number of runaway electrons per unit length lost instantaneously from the layer at $t = 0$, N_{d_s}, is found by integrating Eq. 5.57 to be

$$N_{d_s} = 2\pi\bar{N}\int_b^{a_0} dr r J_0(\gamma_1 r/a_0) = 2\pi\bar{N}(a_0^2/\gamma_1^2)[\gamma_1 J_1(\gamma_1) - (\gamma_1 b/a_0)J_1(\gamma_1 b/a_0)] \tag{5.67}$$

and the corresponding loss rate is

$$\dot{N}_{d_s} = 2\pi\bar{N}(a_0^2/\gamma_1^2)[\gamma_1 J_1(\gamma_1) - (\gamma_1 b/a_0)J_1(\gamma_1 b/a_0)]\delta(t) \approx \pi\bar{N}\gamma_1 J_1(\gamma_1)d_s^2\delta(t) \quad (5.68)$$

The $\delta(t)$ behavior occurs because of the $D_s \to \infty$ at $t = 0$ assumption. The last form is valid for $d_s \ll b$.

Expanding $N(r,t)$ in the eigenfunctions spanning $b \geq r \geq 0$ gives

$$N(r, t \geq 0) = \bar{N}\sum_{n=1}^{\infty} B_n J_0(\gamma_n r/b)\exp(-\gamma_n^2 D_0 t/b^2) \quad (5.69)$$

with the γ_n the ordered zeroes of J_0 such that $J_0(\gamma_n) = 0$. The coefficients B_n must satisfy the initial condition of Eq. 5.57 which gives

$$J_0(\gamma_1 r/a_0) = \sum_{n=1}^{\infty} B_n J_0(\gamma_n r/b) \quad (5.70)$$

The evaluation of the B_n from Eq. 5.70 is greatly simplified by employing the Bessel identity[95]

$$J_0(sz) = 2J_0(z)\sum_{n=1}^{\infty}\frac{\gamma_n J_0(\gamma_n s)}{(\gamma_n^2 - z^2)J_1(\gamma_n)} \quad (5.71)$$

where $1 \geq s \geq 0$, to find for $s = r/b$ and $z = \gamma_1 b/a_0$

$$B_n = \frac{2\gamma_n J_0(\gamma_1 b/a_0)}{[\gamma_n^2 - (\gamma_1 b/a_0)^2]J_1(\gamma_n)} \quad (5.72)$$

Inserting B_n in Eq. 5.69 and forming the flux at $r = b$ gives

$$-2\pi b D_0 \frac{\partial N}{\partial r}|_{r=b} = 4\pi\bar{N}D_0 J_0(\gamma_1 b/a_0)S \quad (5.73)$$

with the sum S defined as

$$S = \sum_{n=1}^{\infty}\frac{\gamma_n^2\exp(-\gamma_n^2 D_0 t/b^2)}{[\gamma_n^2 - (\gamma_1 b/a_0)^2]} \quad (5.74)$$

The sum S may be evaluated to the requisite order for $d_s \ll b$ by extracting the $n = 1$ term and approximating the remaining sum by an integral. Carrying out these steps gives

$$S \approx \frac{b}{2(\pi D_0 t)^{1/2}} + \frac{b}{2d_s}\exp(-\frac{\gamma_1^2 D_0 t}{b^2}) \quad (5.75)$$

for $\gamma_1^2 D_0 t/b^2 \ll \ln(b/d_s)$.

The total loss at turn on is the sum of Eq. 5.68 and 5.73

$$\begin{aligned}\dot{N} &= \dot{N}_{d_s} - 2\pi b D_0 \frac{\partial N}{\partial r}|_{r=b} \\ &= 2\pi\bar{N}\{\frac{a_0^2}{\gamma_1^2}[\gamma_1 J_1(\gamma_1) - (\gamma_1 b/a_0)J_1(\gamma_1 b/a_0)]\delta(t) + 2D_0 J_0(\gamma_1 b/a_0)S\} \quad (5.76)\end{aligned}$$

Normalizing $\dot{N}$ to the initial loss rate $-2\pi D_0 a_0 \partial N/\partial r|_{r=a_0} = -2\pi\bar{N}D_0\gamma_1 J_1(\gamma_1)$, the normalized flux I_n for $d_s \ll b$ and $\gamma_1^2 D_0 t/b^2 \ll \ln(b/d_s)$ is

$$I_n \approx \frac{d_s^2\delta(t)}{2D_0} + \frac{d_s}{(\pi D_0 t)^{1/2}} + \exp(-\frac{\gamma_1^2 D_0 t}{b^2}) \quad (5.77)$$

Eq. 5.77 is the result of the idealized calculation. The change in the normalized flux is found by subtracting one from Eq. 5.77 and is then averaged over the time, t_h, it takes for the coil current I_h to reach flat-top to obtain

$$< \Delta I_n > \approx \frac{d_s^2}{2D_0 t_h} + \frac{2d_s}{(\pi D_0 t_h)^{1/2}} - \frac{\gamma_1^2 D_0 t_h}{2b^2} + \cdots \approx \frac{2d_s}{(\pi D_0 t_h)^{1/2}} \quad (5.78)$$

for $\gamma_1^2 D_0 t_h/b^2 \ll 1$ and $d_s/D_0 t_h \ll 1$. Eq. 5.78 is nothing but the result of substituting $t = t_h$ and $V = d_s/t_s$ in Eq. 5.34. This is not surprising because the stochastic layer generated in the edge region is like moving the plasma boundary into the plasma at speed $V = d_s/t_s$. So Eq. 5.34 can be written as

$$I_n \approx 1 + 2V(\frac{t}{\pi D_0})^{1/2} \quad (5.79)$$

where $V = d_s/t_s$. The "plus" sign is used because the boundary is moving into the plasma now.

Eq. 5.79 is valid only for the short time behavior and is compared to the runaway electron flux change at $t = t_h$ in Fig. 4-16. With $d_s = 2.6$ cm, $t_h = 16.6$ msec and $< \Delta I_n > \approx 1$, The diffusion coefficient is estimated to be

$$D_0 \sim 5 \times 10^2 \text{ cm}^2/\text{sec} \quad (5.80)$$

5.3.2 Numerical model

The numerical model solves for the time period from the turn on to the end of the flat top of I_h. The turn off time period of I_h is not included because it has the long trailing time and is less important in the analysis.

To simulate the transport process with the magnetic perturbation, two ways of modeling the diffusion coefficient are examined and the solution is fitted to the flux from experiment to give an estimate of D_0.

$\mathbf{D_s \propto (b_r/B_0)^2}$

Electron thermal transport with stochastic magnetic fields in a collisionless region can be estimated by the theory[10, 84] to be given by

$$\chi_e \cong D_m v_{the} \tag{5.81}$$

where

$$D_m = \pi q R_0 < (b_r/B_0)^2 > \tag{5.82}$$

is the magnetic diffusion coefficient. b_r is the radial magnetic field and $< \ldots >$ denotes a flux surface average. Kwon, etc.[86] also found that the runaway electron diffusion coefficient has the same dependence on the radial magnetic field. Assuming this also applies to the externally generated magnetic field, then $D_s \propto (b_r/B_0)^2$ is the first model.

With the externally applied magnetic field perturbation, the magnitude of the radial magnetic field is a function of radius and can be written as $(b_r/B_0) \propto r^{m-1}$[84] for the cylindrical coordinates, where $m = 7$ is the poloidal mode number. $D(r,t)$ can then be written as

$$D(r,t) = D_0 + D_s \tag{5.83}$$

with

$$D_s(r,t) = (D_s^a - D_0)R(r)T(t) \tag{5.84}$$

where D_0 and D_s^a, the background and edge diffusion coefficients, are constants and

$$R(r) = (r/a_0)^{12} \tag{5.85}$$

$$T(t) = \begin{cases} (t/t_h)^2 & \text{if } t < t_h \\ 1 & \text{if } t \geq t_h \end{cases} \tag{5.86}$$

Fig. 5-2 plots the diffusion coefficient as a function of radius for $t \geq t_h$. It shows that only the edge ($r/a_0 > 0.8$) is affected. The time dependence is determined by assuming that the magnitude of the perturbing magnetic field is proportional to $I_h(t)$ and the diffusion coefficient $D_s \propto (b_r/B_0)^2 \propto I_h^2 \propto t^2$ during the ramping-up of I_h. The diffusion equation Eq. 5.55 with the initial condition Eq. 5.57, boundary condition at the center Eq. 5.58, and a fixed boundary at the edge

$$N(r = a_0, t) = 0 \tag{5.87}$$

are solved with the diffusion coefficient $D = D(r,t)$ as described above. D_0 and D_s^a are the two parameters to be adjusted to obtain the best fit.

The solid curve in Fig. 5-3 shows the best fit for $I_h = 5$ kA with

$$D_0 = 5 \times 10^2 \text{cm}^2/\text{sec} \tag{5.88}$$

$$D_s^a = 2.3 \times 10^3 \text{cm}^2/\text{sec} \tag{5.89}$$

$D_s \to \infty$

We make the same assumption, $D_s \to \infty$, as assumed in the analytical model. The diffusion equation, Eq. 5.61, is solved with the boundary condition, Eq. 5.63, and the initial condition, Eq. 5.64. Now the edge boundary position $a(t)$ is written as

$$a(t) = \begin{cases} a_0 - d_s t/t_h & \text{if } t < t_h \\ a_0 - d_s & \text{if } t \geq t_h \end{cases} \tag{5.90}$$

The boundary is assumed to be moving into the plasma as the EML is turned on. The stochastic layer generated is assumed to be linear with time during the

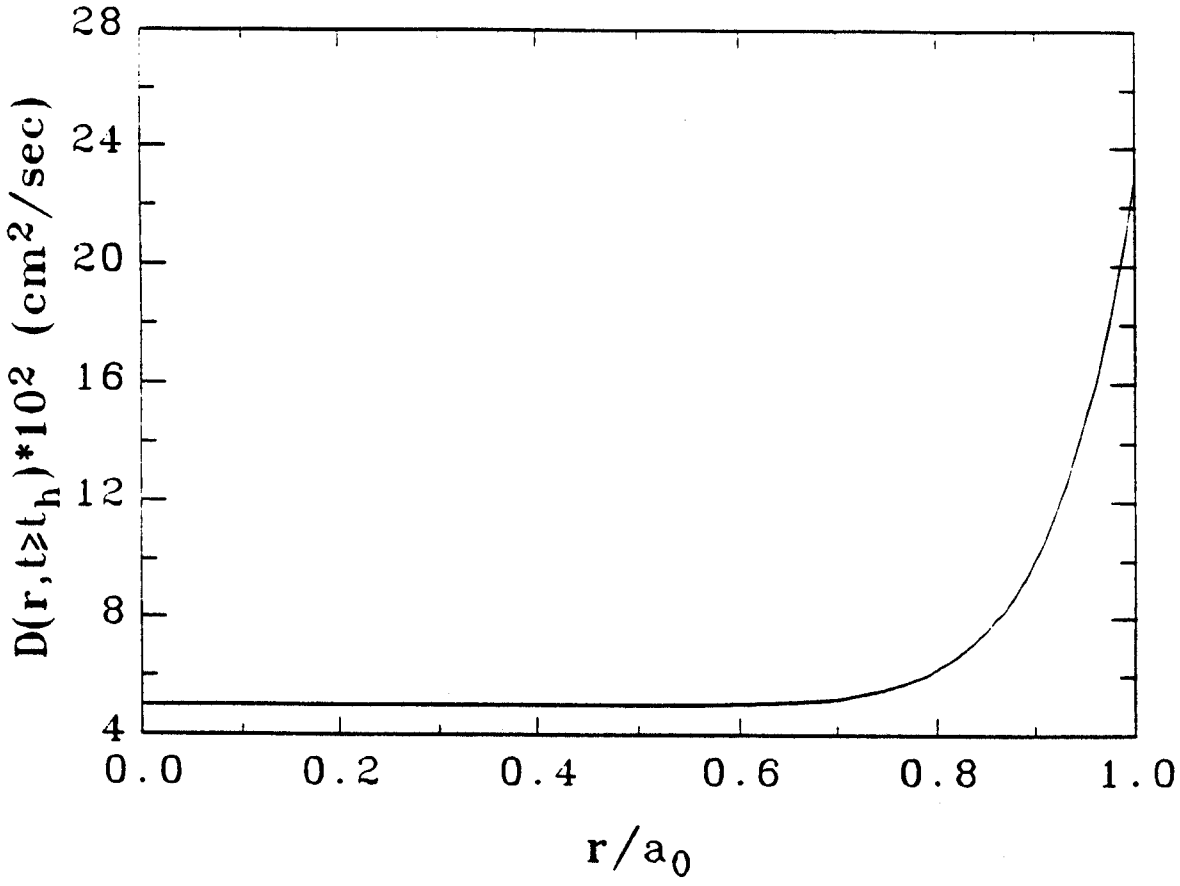

Figure 5-2: The runaway electron diffusion coefficient $D = D(r, t \geq t_h) = D_0 + (D_s^a - D_0)(r/a_0)^{12}$ as a function of radius. It shows that only the edge ($r/a_0 > 0.8$) is affected with $D_0 = 5 \times 10^2$ cm^2/sec and $D_s^a = 2.3 \times 10^3$ cm^2/sec.

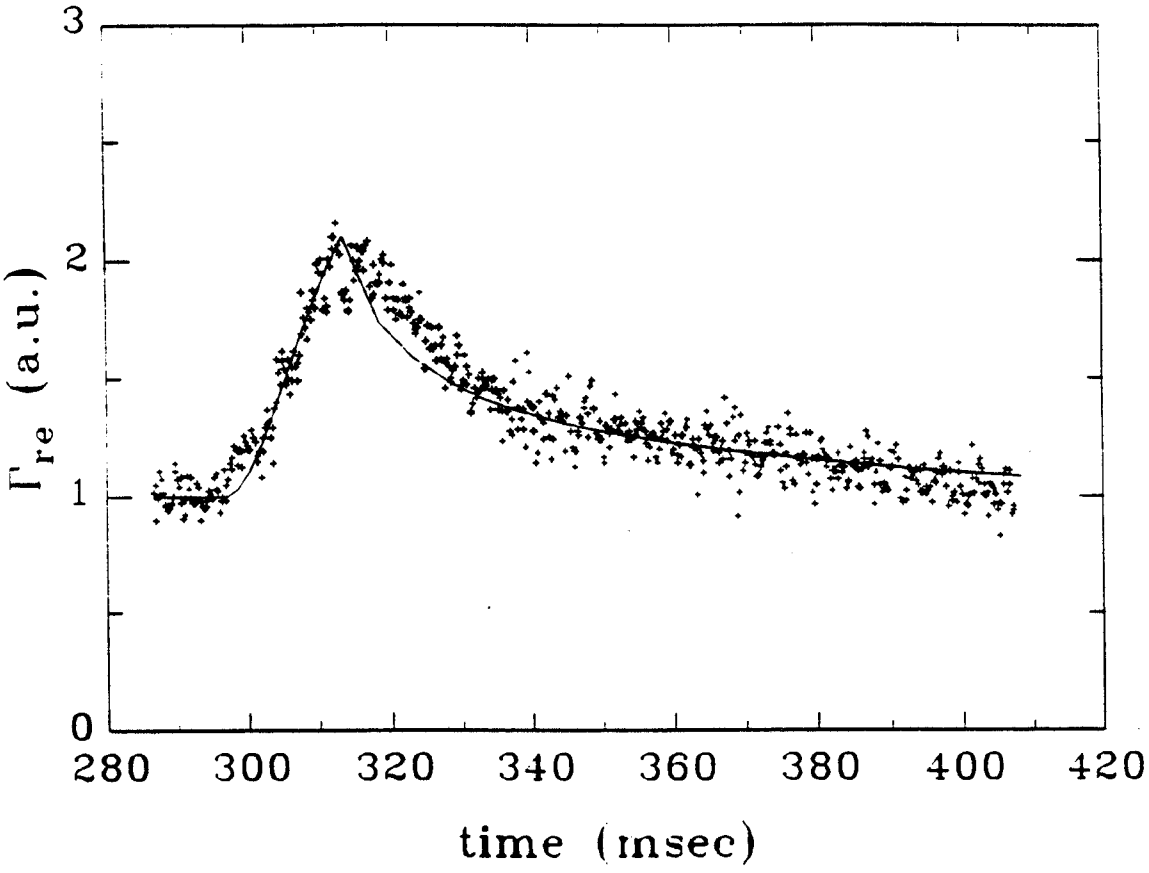

Figure 5-3: Numerical result, the solid curve, for magnetic perturbation experiment with $D_s = D_0 + (D_s^a - D_0)R(r)T(t)$ where $D_0 = 5 \times 10^2$ cm^2/sec and $D_s^a = 2.3 \times 10^3$ cm^2/sec for $I_h = 5$ kA.

ramping-up of I_h. With $D_s \to \infty$, the boundary is moving into the plasma at the speed d_s/t_h. Once I_h reaches the plateau, the edge boundary is kept at smaller radius, $a(t) = b = a_0 - d_s$.

The solution is found with $d_s = 2.6$ cm and $t_h = 16.6$ msec for $I_h = 5$ kA to have the best fit when the runaway electron diffusion coefficient is

$$D_0 \sim 9 \times 10^2 \mathrm{cm}^2/\mathrm{sec} \tag{5.91}$$

as shown by the solid curve in Fig. 5-4.

5.3.3 Discussion of the results

The numerical fit requires only one free parameter, D_0, to be adjusted in Fig 5-4 and two, D_0 and D_s^a, in Fig 5-3. The first model, $D_s = D_s(r,t)$, shows good agreement. Fig. 5-3. The adjustment of the ratio D_0/D_s^a determines the peak magnitude and the value D_0 is to fit the slower decay of the signal. Nevertheless, the diffusion coefficient in the stochastic magnetic fields, D_s^a, deduced from this model is too small compared with the parallel transport along the field lines, $v_{\|}D_m$. This is because the stochastic magnetic field penetrates much deeper into the plasma in the model, $(r/a)^{12}$ as in Eq.5.85, than the actual case. Since the slow decay time is determined by D_0, only D_0 is a useful number from this fitting.

The second model shows the same characteristics of the result. The signal first goes up and reaches the peak, and then shows a fast decay rate preceding a slower one of the signal. The assumption, $D_s \to \infty$, probably is the reason why it overestimates the rising part of the signal, because it kicks out more runaway electrons in the stochastic layer d_s as the boundary is moving in. The faster decay after the peak does not fit well, see Fig. 5-4. This fast decay part shows up when the system is relaxing to the new condition with the perturbed edge stochastic fields. The experimental data that are compared to are energy corrected as explained in the preceding chapters. During the plateau of I_h, the energy is taken to be constant. A small increase in energy after I_h reaches a plateau, Fig. 4-

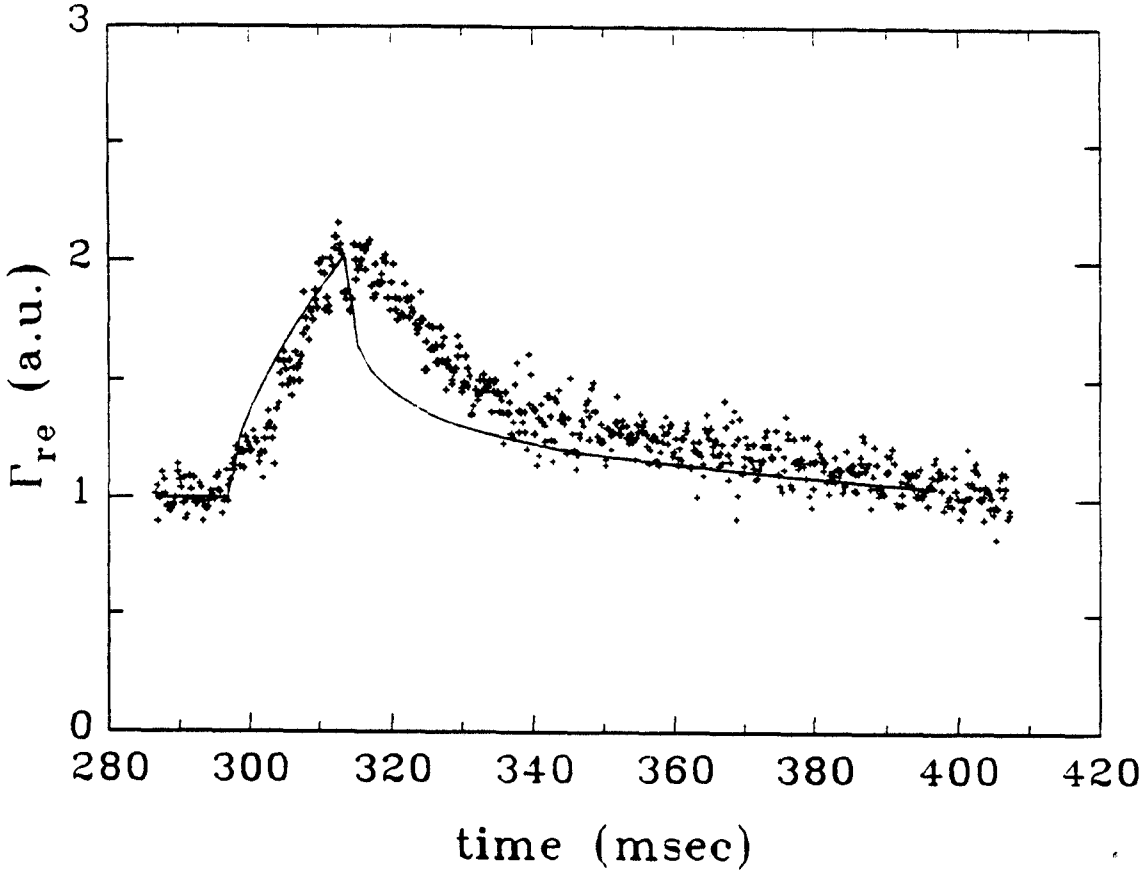

Figure 5-4: Numerical result, the solid curve, for magnetic perturbation experiment with $D_s \rightarrow \infty$ and $D_0 = 9 \times 10^2$ cm^2/sec for $I_h = 5$ kA.

15, could cause the discrepancy of the slower fast decay rate than in the model. Also, magnetic islands are generated much further into the plsma and their effects on runaway electron transport are not considered in the model.

The values of D_0 estimated are accurate within factors of two and show good agreement with the analytical estimate. The speed of the motion, assuming $D_s \rightarrow \infty$, is about 3 times slower than that in the position shift experiment and the boundary is moving in radially making the measurement of D_0 at a position further in than in the shift experiment. The lower values of D_0 estimated indicate that D_0 is decreasing inward from the edge. As in the numerical models, the relaxation to the new condition, after I_h reaches the flat top and the initial faster eigenmodes decay out, is determined mainly by the slower eigenmodes because of the longer time scale. If D_0 is decreasing inward from the edge, this magnetic perturbation experiment measures the smaller D_0 further in and its value is

$$D_0 \sim 10^2 - 10^3 \mathrm{cm}^2/\mathrm{sec} \tag{5.92}$$

5.4 $D_0 = D_0(r)$

By assuming a spatially uniform D_0 in the preceding sections, D_0 was found to be large at the edge from the position shift experiment and small in the interior from the magnetic perturbation experiment. In this section we take the background diffusion coefficient to be a function of radius, $D_0 = D_0(r)$, and it is written as

$$D_0 = D_0(r) = D_0^i + (D_0^a - D_0^i)(\frac{r}{a_0})^{n0} \tag{5.93}$$

where $D_0^i = 5.0 \times 10^2$ cm^2/sec is the interior value and $D_0^a = 1.5 \times 10^4$ cm^2/sec is the edge value. The values of D_0^i and D_0^a were found from the preceding sections. The form of the radial dependence of $D_0(r)$ is chosen such that the constant, $n0$, can be varied to test the different radial profiles. Fig. 5-5 plots the radial profile of D_0 for different $n0$s.

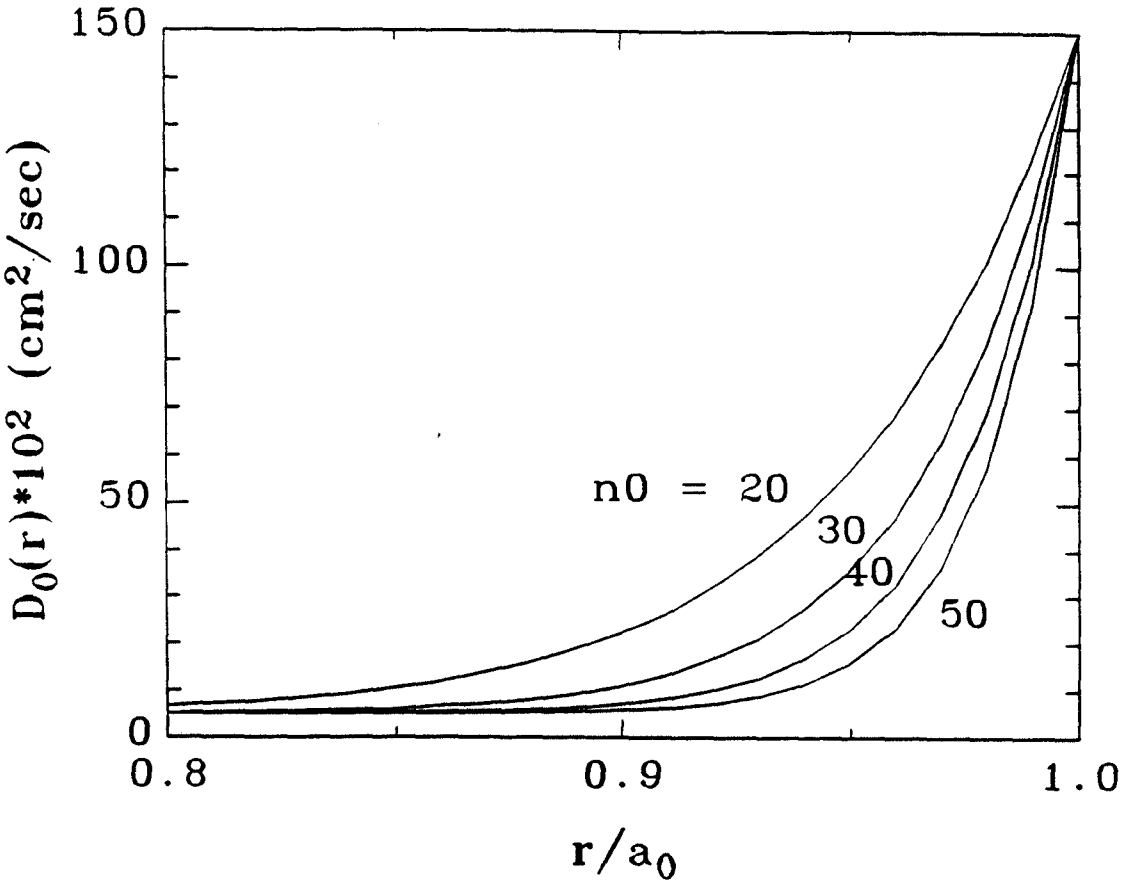

Figure 5-5: The radial profiles of the background runaway diffusion coefficient, $D_0(r) = 500.0 + (15000.0 - 500.0)(\frac{r}{a_0})^{n0}$ cm^2/sec, for $n0$ = 20,30,40, and 50.

The diffusion equation in cylindrical coordinates is solved with two boundary conditions

$$\frac{\partial N(r=0,t)}{\partial r} = 0 \tag{5.94}$$

$$N(r=a_0,t) = 0 \tag{5.95}$$

The initial condition, t=0 being the time at the beginning of the discharge, has a delta-function density profile. The perturbations are turned on after about 300 msec, the time at which the density profile has relaxed to the lowest eigenmode and the exact form of the initial density profile used is not important.

The flux at the limiter is

$$\Gamma(r=a_0) = -D\frac{\partial N}{\partial r}\,|_{r=a_0} \tag{5.96}$$

$$= -\frac{\partial}{\partial t}[\frac{1}{a}\int_0^a Nr\,dr] \tag{5.97}$$

The flux with perturbation is normalized to the unperturbed one and the result is compared with the experimental result.

5.4.1 Position Shift Experiment

As in Sec. 5.2, a change of variable using $s = r/a(t)$ is performed and D_0 in Eq. 5.61 becomes

$$D_0(s) = \begin{cases} D_0^i + (D_0^a - D_0^i)(\frac{sa(t)}{a_0})^{n0} & \text{if } sa(t) < a_0 \\ D_0^a & \text{if } sa(t) \geq a_0 \end{cases} \tag{5.98}$$

The diffusion coefficient in the extra distance from the shifting of the plasma column is taken to be the edge value. The result is shown in Fig. 5-6. It is found that the result is dependent on D_0^a and the value of $n0$ and D_0^i has only minimal effect. It verifies that the diffusion coefficient deduced from the short time recovery of the hard X-ray signal after the shift is the edge value as was concluded in Sec. 5.2.

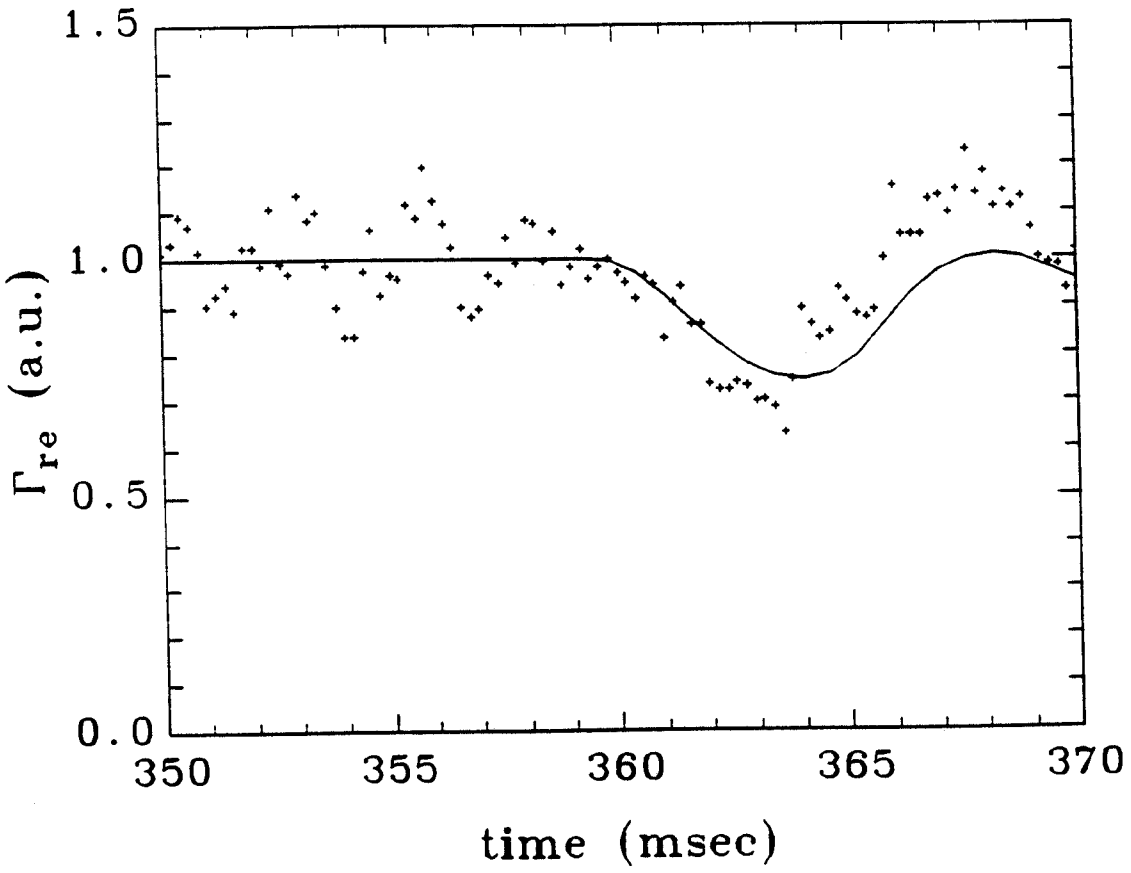

Figure 5-6: Numerical result, the solid curve, for position shift experiment with $D_0(r) = 500.0 + 14500.0(\frac{r}{a_0})^{20}$

5.4.2 Magnetic perturbation experiment

With the assumed constant D_0 across the plasma radius, the runaway diffusion coefficient in the stochastic field, D_s, was found to be much smaller than that of the parallel transport along the magnetic fields, $cD_m \sim 10^{6-7}$ cm^2/sec. Because the process of finding D_s is dependent on D_0, we use a more exact D_0, $D_0 = D_0(r)$ here.

The total diffusion coefficient can be written as

$$D(r,t) = D_0(r) + D_s(r,t) \tag{5.99}$$

The runaway electron diffusion coefficient in the stochastic layer is written as

$$D_s = \alpha v_{\|} D_m \approx \alpha c D_m \tag{5.100}$$

where the parallel velocity is approximately to be the speed of light c and D_m is the magnetic diffusion coefficient. The loss of the runaway electrons in the stochastic layer near the edge is through the parallel motion along the field lines. The drift modification factor α is employed to account for the drift-orbit effects on the runaway electron diffusion[96].

The magnetic diffusion coefficient describes the diffusion of the field lines and is calculated numerically as $D_m = \Delta r^2/(2L)$[97]. Here L is the field line length and Δr is the radial displacement from the initial starting position. Many($\approx 10^4$) different initial θ and ϕ are averaged over for a specified $\Delta r = 2$ cm. Δr is chosen such that D_m is independent of L. Fig. 5-7 shows D_m as a function of radius for different helical current I_h. An analytical form is used to fit D_m

$$D_m = D_m^a \exp[-(\frac{1-\frac{r}{a_0}}{ns})^2] \tag{5.101}$$

and is also shown in Fig. 5-7. Here D_m^a is the edge value and ns is adjusted to fit D_m. For $I_h = 5$ kA, ns is 0.065. During the ramping up of I_h, both ns and D_m^a would increase with time and are written as

$$ns = 0.05(\frac{t-t0}{t1-t0}) + 0.015$$

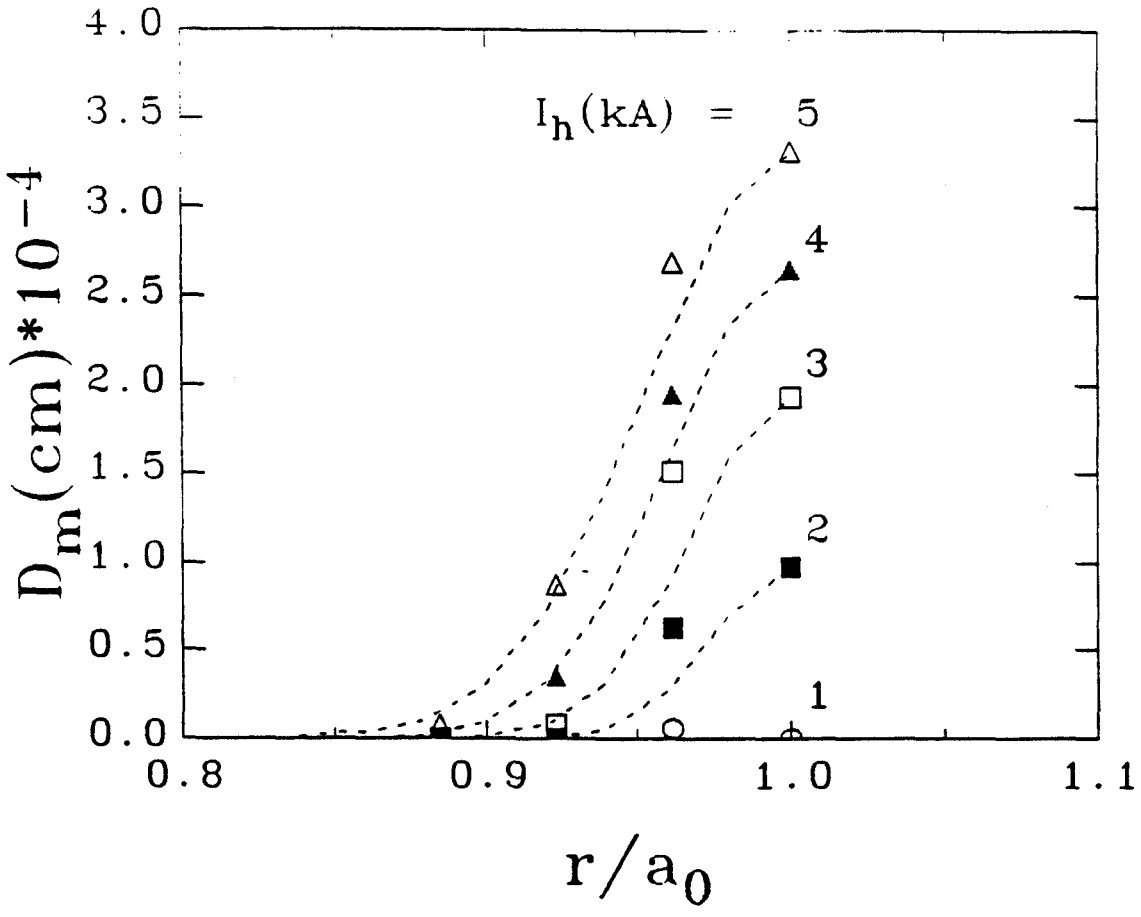

Figure 5-7: The magnetic diffusion coefficient D_m as a function of radius for different helical currents, I_h = 2,3,4, and 5 kA. The solid curves are from the analytical form, $D_m = D_m^a \exp[-(\frac{1-\frac{r}{a_0}}{ns})^2]$ where D_m^a the edge value, for different ns.

$$D_m^a = D_{ms}^a\left(\frac{t-t0}{t1-t0}\right) \quad \text{if } t0 \le t \le t1 \tag{5.102}$$

$$ns = 0.065$$
$$D_m^a = D_{ms}^a \quad \text{if } t1 \le t \le t2 \tag{5.103}$$

to simulate that the stochastic layer penetrates deeper into the plasma and becomes more stochastic as I_h is ramping up. The times $t0$, $t1$, and $t2$ are the time at turn-on, the beginning, and the end of the plateau of I_h, respectively. D_{ms}^a is the edge value for $I_h = 5$ kA.

With all the numbers for D_0 and D_s determined, there are two free parameters, the drift modification factor, α, and the runaway electron radial density profile exponent, $n0$. In Ref. [96] α is found to be dependent on the drift parameter which measures the electron drift-orbit excursion relative to the mode width of the magnetic turbulence. With the runaway electron energy estimated to be in the range 1-2 MeV in TEXT and the edge layer being highly stochastic, the drift parameter is found to be less than 1. This forces α to be of the order of 1. So, $n0$ is the only parameter left to be adjusted to fit the flux at the limiter, Γ_{re}. The result is shown in Fig. 5-8 for $\alpha = 1$. From the best fit, it is estimated $n0 = 19 \sim 21$.

The result fits the rise of the signal well, but the fast decay rate after the peak of the signal is faster. The slow decay rate afterwards is about the same but a little low in magnitude. The peak magnitude of the signal depends on the number of runaway electrons in the edge layer before the turn on of the EML, which is determined by the radial profile of $D_0(r)$. The faster decay rate after the peak of the numerical result has been seen and explained in Sec. 5.3.

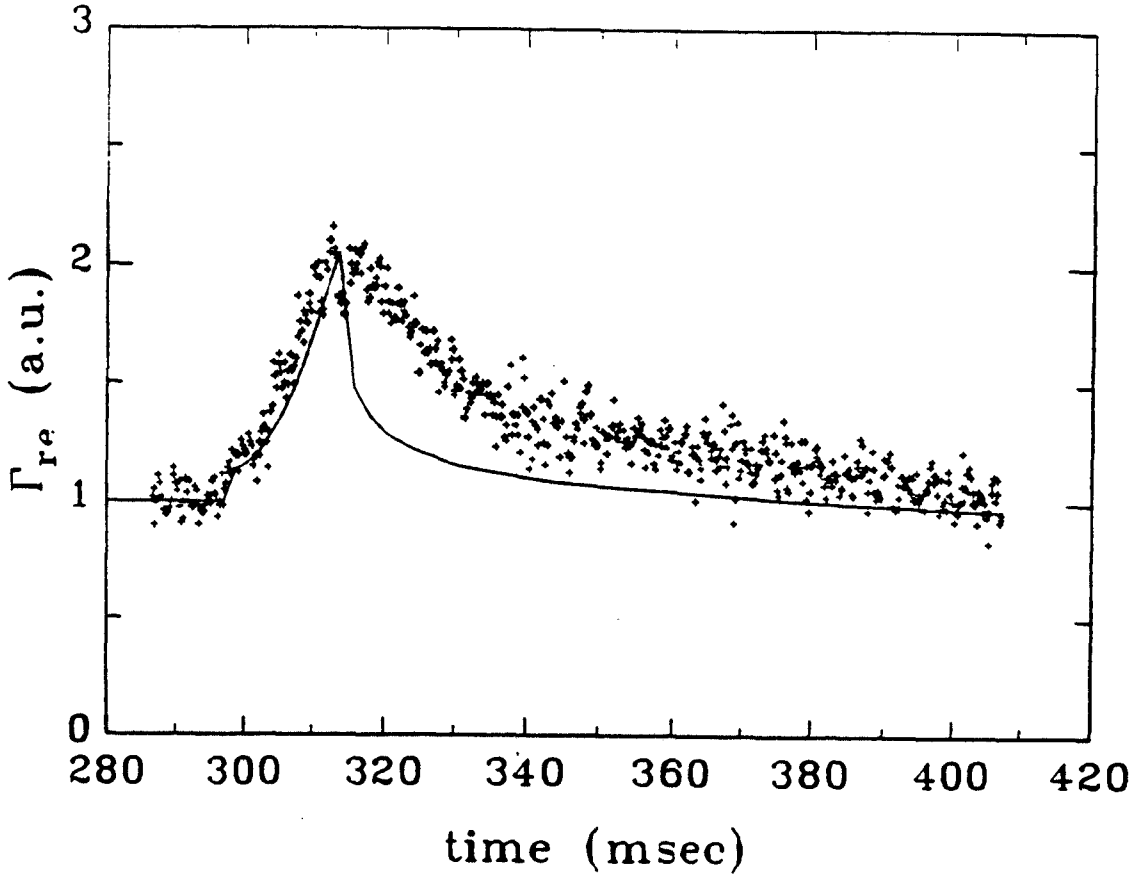

Figure 5-8: Numerical result , the solid curve, for magnetic perturbation experiment with $D_0(r) = 500.0 + 14500.0(\frac{r}{a})^{20}$ and $D_s(r,t) = \alpha c D_m(r,t)$ where $\alpha = 1$.

5.4.3 Magnetic perturbation and position shift experiment

The drift modification factor α is taken to be 1 in the stochastic fields generated by EML. In this subsection we estimate the value of α directly from experimental data. The experiment uses both perturbations, EML and position shift. EML is turned on first and then the plasma column is shifted inward in the middle of the plateau of I_h. Fig. 4-17 shows the signals of I_h and the plasma position as a function of time. The hard X-ray signal change caused by the position shift is very small and is shown in Fig. 4-18. This lack of effect is used to determine α.

The analyses in the preceding subsections also apply here. The exponent $n0$ for the background diffusion coefficient profile is not important because the stochastic diffusion coefficient would dominate the background one as EML is turned on. So, when the plasma column is shifted inward, the edge diffusion which determines the hard X-ray signal change is the stochastic diffusion in the EML fields. By varying α, the results are shown in Fig. 5-9 for $\alpha = 0.001$, 0.01, 0.1, and 1.0. By comparing with experimental data, α is $1.0 \geq \alpha > 0.01$.

5.5 Discussion of the early creation theory

The runaway electron diffusion coefficient is found to be peaked at the edge, $\sim 10^4$ cm^2/sec, and decreasing inward, $\sim 10^2 - 10^3$ cm^2/sec in the core. The numbers found have to be consistent with the early creation theory on which the calculations are based. Since the production of the runaway electrons during the discharge is neglected, the global confinement time has to be long. Runaway electrons created in the center at the early stage of the discharge start to diffuse to the boundary, an absorbing limiter. After some time, the higher eigenmodes decay out and the lowest eigenmode dominates. The observed plateau like state in the hard X- ray signal represents the degree to which the lowest eigenmode

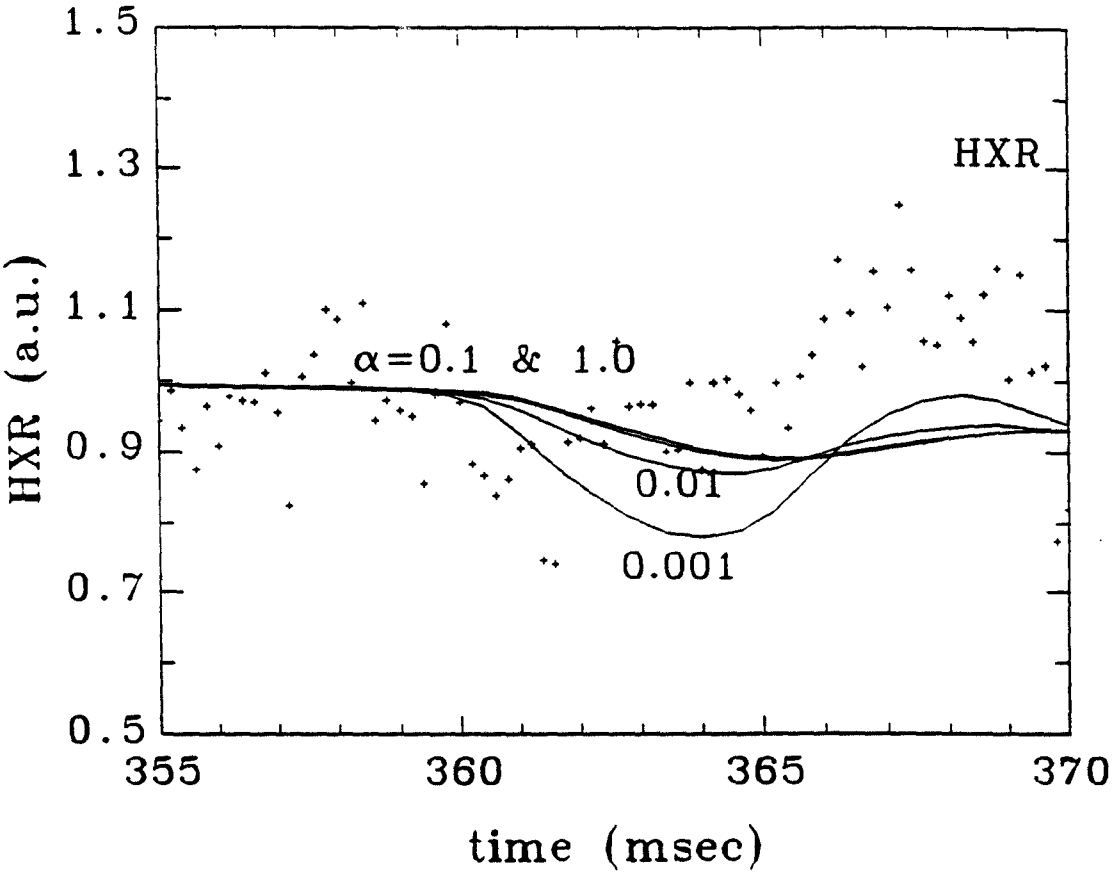

Figure 5-9: Numerical results, the solid curves, for the magnetic perturbation and position shift experiment with α = 0.001, 0.01, 0.1, and 1.0.

mode of the density profile dominates. Then the density can be written as

$$N(r,t) = \bar{N} J_0(\gamma_1 r/a_0) \exp(-\frac{\gamma_1^2 D_0 t}{a_0^2}), \tag{5.104}$$

This radial profile is used as the initial condition for our calculations. The runaway electron flux to the limiter is changing in time as $\Gamma(r = a_0, t) \propto \exp(-\gamma_1^2 D_0 t/a_0^2)$ during this state. But, because the average energy of the the runaway electrons is increasing, though at a slower rate than the free fall, the combination of the two effects gives the nearly a plateau state in the hard X-ray signal. The global confinement time $\tau_{re} = a_0^2/\gamma_1^2 D_0$ has to be $> 200 - 300$ msec, the duration time of the near plateau state. So the diffusion coefficient D_0 can be estimated to be $\sim 10^2 - 10^3$ cm^2/sec. This scenario is consistent with the result that D_0 is small in the core and rises sharply near the edge.

5.6 Possible mechanisms for runaway diffusion

The possible mechanisms responsible for these high energy, collisionless runaway electrons are either the electrostatic or electromagnetic fluctuations inside the plasma. Kwon et al.[86] showed that the electrostatic turbulence cannot govern both the runaway electron confinement and the thermal electron energy confinement. The magnetic turbulence is often suggested as the cause of the anomalous transport of the runaway electrons. The EML experiment has certainly shown that the runaway electrons are sensitive to the magnetic fluctuations. Here, we try to understand the magnetic fluctuations inside the plasma responsible for the diffusion. First, the high energy electron orbits with the perturbed magnetic field, EML, are studied.

5.6.1 Runaway electron drift orbits with EML

A Monte Carlo guiding center code is used to calculate the drift orbits of the high energy runaway electrons. EML fields are calculated from the real geometry of one

coil for the region under the coil by neglecting the finite width of the coil bars, since their effect is not important inside the plasma. The resulting magnetic fields are fitted using the B-spline technique. The region is divided into many sub-regions, and the spline coefficients are stored in a separate file. To calculate the fields at certain location, Eqs. 4.9 and 4.10 are used to determine the corresponding location in the B-spline data file and 4.11 is to determine the sign of the fields. The equilibrium fields are calculated using an equilibrium code PEST. Fig. 5-10(a) shows the equilibrium flux surfaces for $B_t = 2$ T and $I_p = 200$ kA. Fig. 5-10(b) shows the magnetic Poincaré plot with $I_h = 5$ kA at $\phi = 180^o$. The radius is calculated respect to the geometric center, $R_0 = 100$ cm. Also shown are the drift surfaces of the runaway electrons energies of 1 MeV and 5 MeV electrons in the magnetic fields in Fig. 5-10.

With 1 MeV energy, the drift surfaces are not much different from the flux surfaces. With 5 MeV, the drift moves the drift surfaces at $\theta = 0^o$ toward outside and $\theta = 180^o$ inside. However, the magnetic island structure is preserved on the drift surfaces, though the surfaces are shifted toward outside and the edge ergodic surfaces are pushed beyond the boundary and disappeared.

Mynick et al.[57] and Kwon et al.[86] predicted that the improved confinement time for the runaway electrons over the thermal electron energy confinement is due to the drift effects if the magnetic turbulence is assumed to be responsible for both kinds of diffusion. However, the drift has only little effect on 1 MeV or 5 MeV electron with the EML in terms of the island structure.

5.6.2 Estimate of the intrinsic magnetic fluctuations

If the drift effect is small on the runaway electrons whose energies are about 1-2 MeV in TEXT, the diffusion coefficient can be written as

$$D_0 \leq cD_m = \pi cqR_0 < (b_r/B_0)^2 > \qquad (5.105)$$

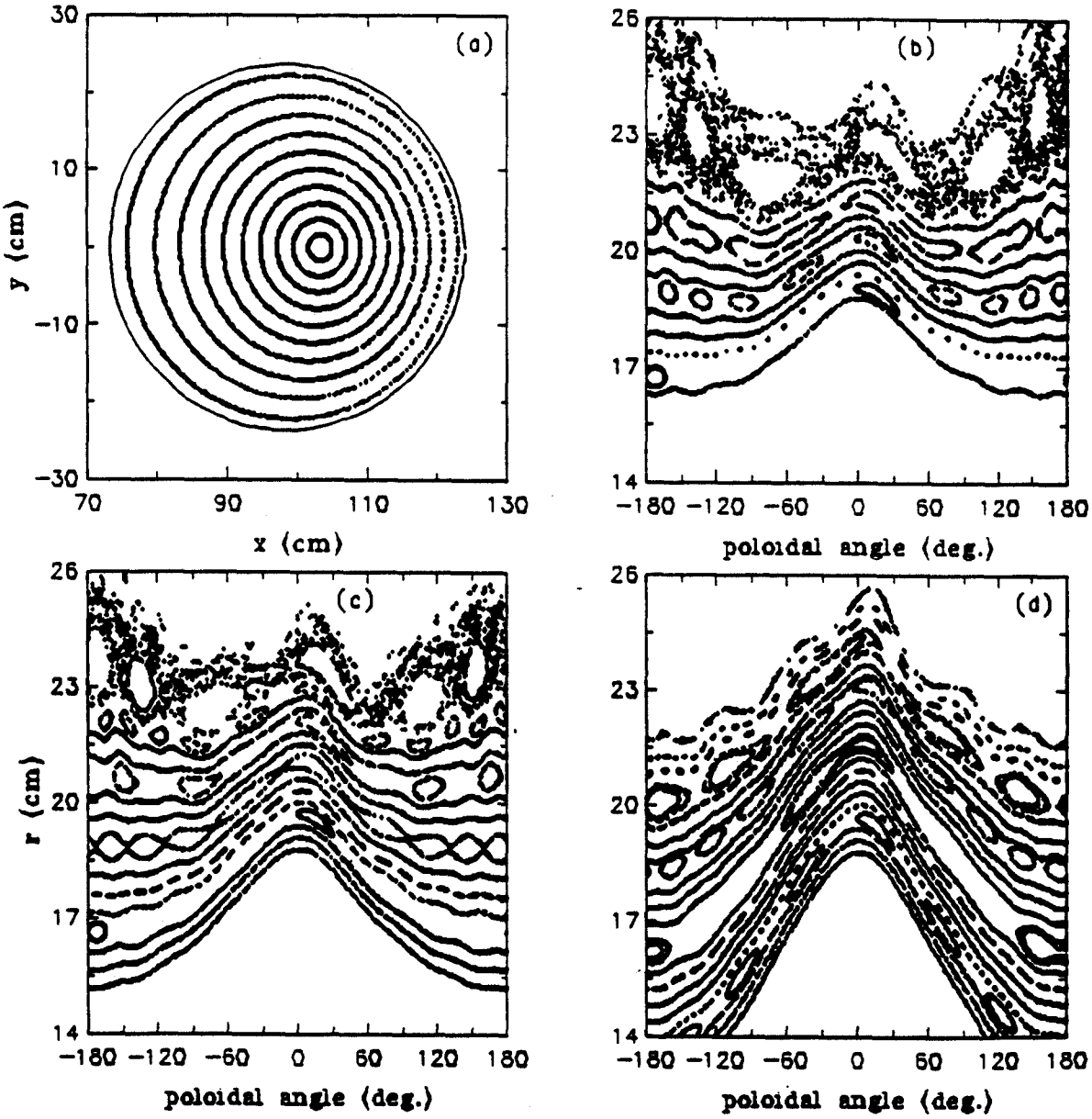

Figure 5-10: (a) The equilibrium flux surfaces from the PEST code for $B_t = 2$ T and $I_p = 200$ kA. (b) The Poincaré plot showing magnetic surfaces with $I_h = 5$ kA at $\phi = 180°$. (c) The drift surfaces of electron with energy 1 MeV. (d) The same as (c) with energy 5 MeV.

Taking $q = 3.5, R_0 = 100$ cm, and $D_0 = 10^4$ cm^2/sec at the edge gives

$$< (b_r/B_0)^2 > \geq 3 \times 10^{-10} \tag{5.106}$$

as a measure of the intrinsic field. The estimate is to be compared with $< (b_r/B_0)^2 > \sim 10^{-10}$ using the extrapolation of the probe measurement into the edge plasma[98]. So, if D_0 is due to the intrinsic magnetic fields then the consistency of the two measurements indicates that the averaging drift effects are small and $< (b_r/B_0)^2 >$ is decreasing inward. For the thermal electrons, the diffusion caused by the magnetic fluctuation, $u_t D_m$, is negligible compared with $\chi_e \sim 10^5$ cm^2/sec[84].

Chapter 6

Summary and conclusions

The generation of the hard X-ray signal at the limiter when high energy runaway electrons leave the plasma and hit the outside of the limiter is observed. Both the time integrated signal and energy spectra are recorded. Because of their high energy, runaway electrons are considered to be collisionless particles. The energy increase rate is found to be less than the "free-fall acceleration rate" due to the electric field. The radial increase of the drift orbit due to the energy increase is too small to be responsible for the runaway electron transport. An anomalous transport has to exist.

To relate the observed hard X-ray signal to the runaway electron particle flux to the limiter, a numerical code DOG[14] is used. This code simulates the processes of the thick-target bremsstrahlung radiation at the limiter, the transmission of the resulting photons through different materials, and their detection. The runaway electron particle flux to the limiter is then deduced and used to be compared to in the analytical and numerical models.

Two experiments have been performed to study the runaway electron transport in TEXT. The first experiment moves the plasma column inward. The observation of the dip in the hard X-ray signal is used to be compared with the analytical and numerical solutions to deduce the diffusion coefficient. The diffusion equation is used based on the assumption that most of the runaway electrons are created

in the center of the plasma at the early stage of the discharge. The production of the runaway electrons during the discharge is negligible. A moving boundary condition is used and the analytical and numerical solutions show good agreement. The diffusion coefficient D_0, estimated to be $\sim 10^4$ cm^2/sec, is interpreted as the edge value because it dominates the short time response to the shift.

The other experiment uses an externally generated helical magnetic field(Ergodic Magnetic Limiter or EML) to perturb the edge of the plasma. The field is in resonance with the edge layer so that magnetic islands, or with overlapped islands, stochastic regions, can be produced. The analytical solution is based on the assumption that the parallel transport along the field lines is responsible for the runaway electron loss. The diffusion coefficient in the stochastic layer is then taken to be infinity, $D_s \rightarrow \infty$. Two models with : (i) $D_s \propto (b_r/B_0)^2$, (ii) $D_s \rightarrow \infty$ are solved numerically. The diffusion coefficient D_0 deduced from both models show good agreement. The characteristics of the longer time scale evolution allows the diffusion coefficient to be interpreted as the core value, which is found to be $\sim 10^2 - 10^3$ cm^2/sec. The runaway diffusion coefficient is then found to be large at the edge and decreasing toward the center. This is consistent with the early creation model which requires a long global confinement time for the runaway electrons.

The diffusion coefficient is then assumed to be a function of radius. It confirms that the diffusion coefficient deduced from the short time recovery of the hard X-ray signal in the position shift experiment is indeed the edge value. In the magnetic perturbation experiment, the radial profile of the diffusion coefficient is determined. The drift modification factor α in the stochastic fields of EML is also determined to be $1.0 \geq \alpha > 0.01$ from the experiment using both magnetic perturbation and the shifting of the plasma column.

The drift surfaces are plotted with EML fields for 1 MeV and 5 MeV electrons. It is found that the drift is small and the drift surfaces are very similar to the flux surfaces for 1 MeV electrons. For 5 MeV electrons, the drift distance is not small

and the drift surfaces are shifted toward the outside, but still preserve the island structure. The typical runaway electron energy is 1 MeV in TEXT. If the averaged drift effects are not important for the runaway electron diffusion in TEXT, the diffusion coefficient can be written as $D_0 \sim cD_m = \pi cqR_0 < (b_r/B_0)^2 >$ and the intrinsic magnetic fluctuation level can then be estimated to be $< (b_r/B_0)^2 > \sim 10^{-10}$. This result is order of magnitude consistent with the probe measurements extrapolated into the edge plasma, which is $< (b_r/B_0)^2 > \sim 4 \times 10^{-10}$. The radial profile of $D_0(r)$ has been analyzed experimentally and theoretically and found to be of the form of Eq. 5.93 with $n0 = 19 \sim 21$. The runaway transport theory of Myra and Catto[96] has been compared to the TEXT experimental data and good agreement is found if the drift modification factor α (γ in Ref. [96]) is taken to be $\alpha = 0.1$ to 1.0. For the externally generated stochasticity (EML), the theoretical result is $\alpha = 1.0$. This at best qualitative agreement may be the first experimental verification of the Rechester-Rosenbluth(improved by Myra-Catto) theory of runaway diffusion. Runaway electrons are a good diagnostic of the magnetic fluctuations because they can offer information further into the interior than the B-dot probes. The magnitude of the edge magnetic fluctuations appears to be too small to induce significant thermal transport, $\chi_e = u_t D_m$. Other mechanisms like electrostatic fluctuations have to play a role in the edge plasma. While if $\alpha = 0.01$ as determined to be the lower bound with EML, the intrinsic magnetic fluctuations $< (b_r/B_0)^2 > \sim 10^{-8}$ could be responsible for the thermal transport at the edge. In the core plasma, recent developments[99] indicate that drift wave turbulence may not be the dominant transport mechanism. Because the driving mechanism may be different for the runaway and thermal electron transport, the good runaway electron confinement and the bad thermal confinement are two separate issues.

Bibliography

[1] H. P. Furth. Review paper : Tokamak research. *Nucl. Fusion*, 15:487, 1975.

[2] F. L. Hinton and R. D. Hazeltine. Theory of plasma transport in toroidal confinement systems. *Rev. Mod. Phys.*, 48:239, 1976.

[3] S. P. Hirshman and D. J. Sigmar. Review paper : Neoclassical transport of impurities in tokamak plasmas. *Nucl. Fusion*, 21:1079, 1981.

[4] S. J. Levinson, J. M. Beall, E. J. Powers, and R. D. Bengtson. Space/time statistics of the turbulence in a tokamak edge plasma. *Nucl. Fusion*, 24:527, 1984.

[5] Ch. P. Ritz, R. D. Bengtson, S. J. Levinson, and E. J. Powers. Turbulent structure in the edge plasma of the TEXT tokamak. *Phys. Fluids*, 27:2956, 1984.

[6] E. J. Powers. Spectral techniques for experimental investigation of plasma diffusion due to polychromatic fluctuations. *Nucl. Fusion*, 14:749, 1974.

[7] P. C. Liewer. Review paper : Measurements of microturbulence in tokamaks and comparisons with theories of turbulence and anomalous transport. *Nucl. Fusion*, 25:543, 1985.

[8] N. T. Gladd, J. F. Drake, C. L. Chang, and C. S. Liu. Electron temperature gradient driven microtearing mode. *Phys. Fluids*, 23:1182, 1980.

[9] W. M. Tang. Review paper : Microinstability theory in tokamaks. *Nucl. Fusion*, 18:1089, 1978.

[10] A. B. Rechester and M. N. Rosenbluth. Magnetic braiding due to weak asymmetry. *Phys. Rev. Lett.*, 40:38, 1978.

[11] T. H. Stix. Plasma transport across a braided magnetic field. *Nucl. Fusion*, 18:353, 1978.

[12] J. A. Krommes, C. Oberman, and R. G. Kleva. Plasma transport in stochastic magnetic fields : part 3. kinetics of test particle diffusion. *J. Plasma Phys.*, 30:11, 1983.

[13] J. D. Callen. Drift-wave turbulence effects on magnetic structure and plasma transport in tokamak. *Phys. Rev. Lett.*, 39:1540, 1977.

[14] C. W. Barnes. *Studies of Runaway Electron Transport in Princeton Large Torus and Poloidal Divertor Experiment.* PhD thesis, Princeton University, 1981. University Microfilms, Ann Arbor.

[15] H. Dreicer. Electron and ion run-away in fully ionized gas. *Phys. Rev.*, 115:238, 1959.

[16] H. Knoepfel and D. A. Spong. Runaway electrons in toroidal discharges. *Nucl. Fusion*, 19:785, 1979.

[17] S. Sesnic. Electron runaway in tokamak devices. In *Course on Plasma Diagnostics and Data Acquisition Systems, Varenna*, page 357, 1975.

[18] A. V. Gurevich. On the theory of runaway electrons. *Sov. Phys.-JETP*, 12:904, 1961.

[19] A. N. Lebedev. Contribution to the theory of runaway electrons. *Sov. Phys.–JETP*, 21:931, 1965.

[20] M. Kruskal and I. B. Bernstein. Runaway electrons in an ideal Lorentz plasma. *Phys. Fluids*, 7:407, 1964.

[21] A. V. Gurevich and Yu. N. Zhivlyuk. Runaway electrons in a nonequilibrium plasma. *Sov. Phys.-JETP*, 22:153, 1966.

[22] R. M. Kulsrud, Y. C. Sun, N. K. Winsor, and H. A. Fallon. Runaway electrons in a plasma. *Phys. Rev. Lett.*, 31:690, 1973.

[23] J. W. Connor and R. J. Hastie. Relativistic limitations on runaway electrons. *Nucl. Fusion*, 15:415, 1975.

[24] R. H. Cohen. Runaway electrons in an impure plasma. *Phys. Fluids*, 19:239, 1976.

[25] A. V. Gurevich and Y. S. Dimant. Kinetic theory of runaway production in toroidal magnetic devices. *Nucl. Fusion*, 18:629, 1978.

[26] Routine D02BBF in NAG library.

[27] G. Fussman. On the motion of runaway electrons in momentum space. *Nucl. Fusion*, 19:327, 1979.

[28] P. Gratreau. Single particle trajectories in axisymmetrical electromagnetic fields : application to tokamaks under runaway regime. *Phys. Fluids*, 19:695, 1977.

[29] A. H. Morton and K. G. Srinivasacharya. Investigations of the electron runaway in slow toroidal Θ-Z pinch, LT-1. *Plasma Phys.*, 14:687, 1972.

[30] J. D. Strachan and R. L. Dewar. Electron runaway in LT-3. In *Plasma Physics and Controlled Nuclear Fusion Research (Proc. 5th Int. Conf. Tokyo, 1974)*, volume 1, page 171, 1974.

[31] I. H. Hutchinson and A. H. Morton. The skin effect and its relaxation in tokamak LT-3. *Nucl. Fusion*, 16:447, 1976.

[32] J. D. Strachan. Runaway electron transport in the LT-3 tokamak. *Nucl. Fusion*, 16:743, 1976.

[33] V. S. Vlasenkov, V. M. Leonov, V. G. Merezhkin, and V. S. Mukhovatov. The runaway electron discharge regime in the Tokamak-6 device. *Nucl. Fusion*, 13:509, 1973.

[34] V. S. Alikaev, G. A. Bobrovskii, and K. A. Razumova. Superthermal X radiation in the TM-3. *Sov. J. Plasma Phys.*, 1:303, 1975.

[35] V. V. Sannikov and Yu. A. Sokolov. Runaway electrons in the TM-3 tokamak. *Sov. J. Plasma Phys.*, 2:112, 1976.

[36] G. J. Boxman, B. Coppi, L.C.J.M. de Kock, B.J.H. Meddens, A.A.M. Oomens, L.Th.M. Ornstein, D. S. Pappas, R. R. Parker, L. Pieroni, S. E. Segre, F. C. Schuller, and R. J. Taylor. Low and high density operation of Alcator. In *Controlled Fusion and Plasma Physics (Proc. of the 7th European Conf., Lausanne)*, volume 2, page 14, 1975.

[37] S. Von Goeler and W. Stodiek. High energy electrons in the ST tokamak discharges. In *Controlled Fusion and Plasma Physics (Proc. of the 5th European Conf., Grenoble)*, volume 1, page 2, 1972.

[38] S. Von Goeler, W. Stodiek, N. Sauthoff, and H. Selberg. X-ray spectra in the ST tokamak. In *Proc. 3rd Int. Symp. on Toroidal Confinement, Garching*, page B25, 1973.

[39] H. Knoepfel and S. J. Zweben. High-energy runaway electrons in the Oak Ridge tokamak. *Phys. Rev. Lett.*, 35:1340, 1975.

[40] S. J. Zweben, D. W. Swain, and H. H. Fleischmann. Radial transport of high-energy runaway electrons in ORMAK. *Nucl. Fusion*, 18:1679, 1978.

[41] M. G. Kaganskii and S. G. Kalmykov. Behavior of runaway electrons in the Tuman-2 device. *Sov. J. Plasma Phys.*, 4:18, 1978.

[42] G. Fussmann and S. Sesnic. Investigations of runaways in the Pulsator tokamak. *IPP*, 3:37, 1977.

[43] G. Fussmann, W. Engelhardt, W. Feneberg, J. Gernhardt, E. Glock, F. Karger, S. Sesnic, and H. P. Zehrfeld. Investigation of modulated runaway losses and effects of a helical dipole field in Pulsator. In *Plasma Physics and Control Nuclear Fusion Research (Proc. 7th Int. Conf. Innsbruck, 1978)*, volume 1, page 401, 1979.

[44] S. A. Eckstrand. *An Investigation of Runaway Electrons in the Pretext tokamak.* PhD thesis, University of Texas, 1981. FRC#219.

[45] P. Brossier. Runaway-driven kinetic instabilities in tokamaks. *Nucl. Fusion*, 18:1069, 1978.

[46] V. V. Parail and O. P. Pogutse. The kinetic theory of runaway electron beam instability in a tokamak. *Nucl. Fusion*, 18:303, 1978.

[47] K. Papadopoulos, B. Hui, and N. Winsor. Formation of positive slope on electron runaway distribution in tokamaks. *Nucl. Fusion*, 17:1087, 1977.

[48] E. Moghaddam-Taaheri, L. Vlahos, H. L. Rowland, and K. Papadopoulos. Runaway tails in magnetized plasmas. *Phys. Fluids*, 28:3356, 1985.

[49] E. Moghaddam-Taaheri and L. Vlahos. Dynamics of runaway tails with time-dependent sub-Dreicer dc fields in magnetized plasmas. *Phys. Fluids*, 30:3155, 1987.

[50] L. Muschietti, K. Appert, and J. Vaclavik. Quasisteady turbulence driven by runaway electrons. *Phys. Fluids*, 25:1187, 1982.

[51] J. C. Wiley, D. I. Choi, and W. Horton. Simulations of the runaway electron distributions. *Phys. Fluids*, 23:2193, 1980.

[52] D. S. Liu, Y. C. Mok, K. Papadopoulos, F. Engelmann, and M. Bornatici. Nonlinear dynamics of runaway electrons and their interaction with tokamak liners. *Phys. Rev. Lett.*, 39:701, 1977.

[53] K. Molvig, M. S. Tekula, and A. Bers. Theory of runaway electron tail. *Phys. Rev. Lett.*, 38:1404, 1977.

[54] C. W. Barnes, J. M. Stavely Jr., and J. D. Strachan. High-energy runaway electron transport deduced from photonuclear activation of the PLT limiter. *Nucl. Fusion*, 21:1469, 1981.

[55] C. W. Barnes and J. D. Strachan. Measurements of the fluctuations in the flux of runaway electrons to the PLT tokamak limiter. *Phys. Fluids*, 26:2668, 1983.

[56] C. W. Barnes and J. D. Strachan. Sawtooth oscillations in the flux of runaway electrons to the PLT limiter. *Nucl. Fusion*, 22:1090, 1982.

[57] H. E. Mynick and J. D. Strachan. Transport of runaway and thermal electrons due to magnetic turbulence. *Phys. Fluids*, 24:695, 1981.

[58] H. E. Mynick and J. A. Krommes. Particle stochasticity due to magnetic perturbations of axisymmetric geometries. *Phys. Fluids*, 23:1229, 1980.

[59] H. E. Mynick and J. A. Krommes. Particle diffusion by magnetic perturbations of axisymmetric geometries. *Phys. Rev. Lett.*, 43:1506, 1979.

[60] TEXT user handbook. Technical report, Fusion Research Center, Univ. of Texas, 1988.

[61] S. Von Goeler, J. Stevens, S. Bernabei, M. Bitter, T. K. Chu, P. Efthimion, N. Fisch, W. Hooke, K. Hill, J. Hosea, F. Jobes, C. Karney, J. Mervine, E. Meservey, R. Motley, P. Roney, S. Sesnic, K. Silber, and G. Taylor. Angular distribution of the bremsstrahlung emission during lower hybrid current drive on PLT. *Nucl. Fusion*, 25, 1985.

[62] S. Texter. *Plasma X-ray spectroscopy during lower hybrid current drive on Alcator.* PhD thesis, Massachusetts Institute of Technology, 1986. PFC/RR-85-24.

[63] B. Bulow and B. Forkman. Photonuclear cross-sections in handbook on nuclear activation cross-section. Technical report, IAEA, 1974.

[64] Canberra Industries Inc. *Series-35 multichannel analyzer operator's mannual.*

[65] S. Koicki, A. Koicki, and V. Ajdacic. The investigation of the 0.15 s phosphorescent component of NaI(Tl) and its application in scintillation counting. *Nucl. Inst. Meth.*, 108:297, 1973.

[66] R. D. Evans. *The atomic nucleus.* McGraw-Hill, New York, 1952.

[67] G. R. White. Technical report, Natl. Bur. Standards (U.S.), 1952. Rept. 1003.

[68] TFR Group. Observation of photonuclear processes in the TFR tokamak. *Phys. Letters*, 60A:219, 1977.

[69] TFR Group. Activation effects due to runaway beams on TFR. *J. Nucl. Mater.*, 93&94:203, 1980.

[70] W.K.H. Panofsky and M. Phillips. *Classical Electricity and Magnetism.* Addison-Wesley, Reading, MA, 1955.

[71] A. J. Russo. Effect of ripple on runaway electrons in tokamaks. *Nucl. Fusion*, 31:117, 1991.

[72] W. Feneberg. In *Controlled Fusion and Plasma Physics (Proc. 8th Europ. Conf. Prague, 1977)*, volume 1, page 3, 1977.

[73] F. Karger and K. Lackner. Resonant helical divertor. *Phys. Lett.*, 61A:385, 1977.

[74] W. Engelhardt and W. Feneberg. Influence of an ergodic magnetic limiter on the impurity content in a tokamak. *J. Nucl. Mater.*, 76&77:518, 1978.

[75] N. Ohyabu. Expanded-boundary approach to impurity control in tokamaks. *Nucl. Fusion*, 21:519, 1981.

[76] W. Feneberg and G. H. Wolf. A helical magnetic limiter for boundary layer control in large tokamaks. *Nucl. Fusion*, 21:669, 1981.

[77] P. Deschamps, A. Grosman, M. Lipa, and A. Samain. Power exhaust and plasma-surface interaction control in TORE SUPRE. *J. Nucl. Mater.*, 128&129:38, 1984.

[78] A. Samain, A. Grosman, T. Blenski, G. Fuchs, and B. Steffen. An ergodic divertor for TORE SUPRA. *J. Nucl. Mater.*, 128&129:395, 1984.

[79] A. J. Wootton, R. D. Bengtson, and et al. In *Plasma Physics and Controlled Nuclear Fusion Research 1986 (Proc. 11th Int. Conf. Kyoto, 1986)*, volume 1, page 187, Vienna, 1987. IAEA.

[80] N. Ohyabu, J. S. DeGrassie, N. Brooks, T. Taylor, H. Ikezi, K. W. Gentle, R. Bengtson, R. Bravenec, W. Hodge, K. Nelin, P. Phillips, B. Richards, C. Ritz, W. Rowan, Y. X. Wan, C. Klepper, J. Porter, and J. Snipes. Ergodic magnetic layer experiment. *Nucl. Fusion*, 25:1684, 1985.

[81] T. E. Evans, J. S. DeGrassie, H. R. Garner, A. W. Leonard, N. Ohyabu, L. S. Peranich, and et al. Experiments to test an intra-island scoop limiter on TEXT. *J. Nucl. Mater.*, 145:812, 1987.

[82] J. S. DeGrassie, N. Ohyabu, N. H. Brooks, and et al. Ergodic magnetic limiter experiments on TEXT with a 7/3 resonance. *J. Nucl. Mater.*, 128&129:266, 1984.

[83] N. Ohyabu, J. S. DeGrassie, N. H. Brooks, T. S. Taylor, H. Ikezi, and TEXT group. Preliminary results from the ergodic magnetic limiter experiment on the TEXT experimental tokamak. *J. Nucl. Mater.*, 121:363, 1984.

[84] S. C. McCool, A. J. Wootton, A. Y. Aydemir, R. D. Bengtson, J. A. Boedo, R. V. Bravenec, D. L. Brower, J. S. DeGrassie, T. E. Evans, S. P. Fan, J. C. Forster, M. S. Foster, K. W. Gentle, Y. X. He, R. L. Hickock, G. L. Jackson, S. K. Kim, M. Kotschenreuther, N. C. Luhmann Jr., W. H. Miner Jr., N. Ohyabu, D. M. Patterson, W. A. Peebles, P. E. Philips, T. L. Rhodes, B. Richards, Ch. P. Ritz, D. W. Ross, W. L. Rowan, P. M. Schoch, B. A. Smith, J. C. Wiley, X. H. Ye, and S. B. Zheng. Electron thermal confinement studies with applied resonant fields on TEXT. *Nucl. Fusion*, 29:547, 1989.

[85] S. C. McCool, A. J. Wootton, M. Kotschenreuther, A. Y. Aydemir, R. V. Bravenec, J. S. DeGrassie, T. E. Evans, R. L. Hickok, B. Richards, W. L. Rowan, and P. M. Schoch. Particle transport studies with applied resonant fields on TEXT. *Nucl. Fusion*, 30:167, 1990.

[86] O. J. Kwon, P. H. Diamond, F. Wagner, G. Fussmann, ASDEX, and NI TEAMS. A study of runaway electron confinement in the ASDEX tokamak. *Nucl. Fusion*, 28:1931, 1988.

[87] T. J. Martin and J. B. Taylor. Ergodic behaviour in a magnetic limiter. *Plasma Phys.*, 26:321, 1984.

[88] X. H. Yu and J. S. DeGrassie. Mapping techniques for the GA Ergodic Magnetic Limiter experiment on TEXT. Technical report, Fusion Research Center, Univ. of Texas, 1986. FRC#292.

[89] S. B. Zheng and A. J. Wootton. Magnetic island widths in tokamaks. Technical report, Fusion Research Center, Univ. of Texas, 1987. FRC#294.

[90] S. Takamura, H. Yamada, S. C. McCool, and A. J. Wootton. Computer code for field line tracing. Technical report, Fusion Research Center, Univ. of Texas, 1987. FRC#298.

[91] A. B. Rechester and T. H. Stix. Electron heat transport in a tokamak with destroyed magnetic surfaces. *Phys. Rev. Lett.*, 36:587, 1976.

[92] P. J. Catto, J. R. Myra, P. W. Wang, A. J. Wootton, and R. D. Bengtson. Estimating the runaway diffusion coefficient in TEXT from shift and externally applied resonant magnetic field experiments. To be published in Phys. Fluids, 1991.

[93] I. S. Gradshteyn and I. M. Ryzhik. *Table of integrals, series, and products*, pages 338, 480 and 495. Academic, New York, 1965.

[94] Routine D03PAF in NAG library.

[95] W. Magnus, F. Oberhettinger, and R. P. Soni. *Formulas and theorems for the special functions of mathematical physics*, page 134. Springer-Verlag, New York, 3 edition, 1966.

[96] J. R. Myra and P. J. Catto. Effect of drifts on the diffusion of runaway electrons in tokamak stochastic magnetic fields. Technical report, Lodestar Research Corporation, 1991. LRC-91-25.

[97] A. J. Wootton and S. B. Zheng. Test particle calculations for TEXT with resonant magnetic fields. Technical report, Fusion Research Center, Univ. of Texas, 1988. FRC#325.

[98] Y. J. Kim. General description of magnetic fluctuations in text. Technical report, Fusion Research Center, Univ. of Texas, 1989. FRC#344.

[99] D. W. Ross, P. M. Schoch, J. W. Heard, T. P. Crowley, and R. L. Hickok. Dispersion relations of density fluctuations observed by the heavy ion beam probe in TEXT. *Nucl. Fusion*, 31:1355, 1991.